National and Kapodistrian Univesity of Athens
Department of Physics

Study of Atmospheric Boundary Layer dynamics in coastal areas, using active remote sensing methods

Ioanna Tsikoudi

A Doctoral Dissertation submitted to the
Environmental Physics - Meteorology Sector of the Physics Department,
National and Kapodistrian University of Athens

May 2025

Advisory Committee

Eleni Giannakaki, Section of Environmental Physics and Meteorology, Department of Physics, University of Athens, Greece, Assistant Professor (Supervisor).

Maria Tombrou, Section of Environmental Physics and Meteorology, Department of Physics, University of Athens, Greece, Professor.

Vassilis Amiridis, Research Director, National Observatory of Athens.

Examining Committee

Eleni Giannakaki, Section of Environmental Physics and Meteorology, Department of Physics, University of Athens, Greece, Assistant Professor (Supervisor).

Maria Tombrou, Section of Environmental Physics and Meteorology, Department of Physics, University of Athens, Greece, Professor.

Vassilis Amiridis, Research Director, National Observatory of Athens.

Elena Floca, Section of Environmental Physics and Meteorology, Department of Physics, University of Athens, Greece, Professor.

Georgia Sotiropoulou, Section of Environmental Physics and Meteorology, Department of Physics, University of Athens, Greece, Associate Professor.

Dimitrios Balis, Department of Applied and Environmental Physics, Faculty of Sciences, Aristotle University of Thessaloniki, Professor.

Stelios Kazadzis, Physicalisch Meteorologisches Observatorium Davos, World Radiation Center, Switzerland, Senior Researcher.

Στους γονείς μου,
την αδερφή μου,
και το Νικηφόρο.

Abstract

This study investigates the characteristics of the Atmospheric Boundary Layer (ABL) in marine environments using active remote sensing measurements and radiosondes. PollyXT Raman Lidar and Halo Wind Doppler Lidar observations were utilized to retrieve the ABL height and its diurnal evolution, while radiosonde profiles of temperature, humidity, and wind provided information about the vertical structure of the lower troposphere and atmospheric dynamics. Various methods, namely the Wavelet Covariance Transform, gradient, parcel, Richardson, and threshold methods, were applied and assessed across different atmospheric variables. Among these, WCT proved the most effective and optimal for detecting the complexities of profiles with multiple aerosol layers. The study focuses on two locations: Finokalia on the island of Crete, Greece, where the PreTECT Campaign was conducted in April 2017, and Mindelo on São Vicente island, Cabo Verde, during the ASKOS Campaign in 2021-2022. In both regions, the ABL displayed Marine Atmospheric Boundary Layer (MABL) characteristics with minimal sharp daytime evolution. In Finokalia, a coastal site with complex terrain, the dynamics presented significant variability under different meteorological conditions. A comparison of measured ABL heights with ECMWF model outputs for two neighboring land and sea model bins revealed systematic discrepancies. These were attributed to the coarse resolution of the model, surface roughness transitions, and horizontal advection effects. In Cabo Verde, ground-based observations capture an ABL height of approximately 600 m, which is in good agreement with the results from statistical analysis of ECMWF data for September 2022. CALIPSO satellite observations from CALIOP, a space-borne lidar, provided additional information for the ABL in a broader domain over the Atlantic. A 10-year dataset of CALIPSO and ECMWF data for cloud-free conditions in the open ocean yielded a consistent ABL top height of approximately 700 m. However, over the transition zone between the eastern Atlantic and the western African continent, significant discrepancies were observed between the model and the satellite measurements. These differences likely arise from the reduced reliability of ECMWF's Richardson-based method under weak stratification or coarse vertical resolution, the CALIPSO's limited sensitivity near the desert surface, and the model uncertainties related to the lack of surface observations and aerosol–radiation interactions. Finally, detailed analysis of selected cases in Mindelo, Cabo Verde, explored the interaction between thermodynamic stability and boundary layer characteristics. Impact of marine and desert dust aerosols on the dynamics and structure of the MABL is investigated in this region.

Extended Abstract in Greek
ΕΚΤΕΤΑΜΕΝΗ ΠΕΡΙΛΗΨΗ

Η παρούσα διδακτορική διατριβή πραγματεύεται τα χαρακτηριστικά του Ατμοσφαιρικού Οριακού Στρώματος (ΑΟΣ) σε θαλάσσια περιβάλλοντα με τη χρήση μεθόδων ενεργητικής τηλεπισκόπησης. Διερευνώνται τα εξής θέματα: (α) ποια είναι η πιο αξιόπιστη και βέλτιστη χρήση μεθόδων τηλεπισκόπησης για την εύρεση του ύψους του ΑΟΣ, (β) ποια είναι τα χαρακτηριστικά του ΑΟΣ στις περιοχές μελέτης και (γ) ποια είναι η επίδραση των αιωρούμενων σωματιδίων (σκόνη και θαλάσσια σωματίδια) στην ανάπτυξη του ΑΟΣ. Για το σκοπό αυτό χρησιμοποιήθηκαν μετρήσεις επίγειου και δορυφορικού συστήματος lidar, καθώς και δεδομένα ραδιοβολίσεων για την αξιολόγηση των νέων μεθόδων.

Τα θαλάσσια περιβάλλοντα παρουσιάζουν ιδιαίτερα χαρακτηριστικά ως προς τον άνεμο, την ύπαρξη αιωρούμενων σωματιδίων, τη δημιουργία νεφών και κατ'επέκταση το σχηματισμό του ατμοσφαιρικού οριακού στρώματος. Όταν επιπρόσθετα υπάρχουν υψηλές συγκεντρώσεις αιωρούμενων σωματιδίων διαφορετικού τύπου, όπως ερημική σκόνη, τα χαρακτηριστικά του οριακού στρώματος είναι ιδιαίτερα και ο εντοπισμός του ύψους της κορυφής του πιο δύσκολος. Για τους σκοπούς της διατριβής, συλλέχθηκαν και αναλύθηκαν δεδομένα από δύο περιοχές: Τη Φινοκαλιά Κρήτης στη Μεσόγειο, και το νησί Sao Vincente, στον Ατλαντικό Ωκεανό. Η Φινοκαλιά, βρίσκεται στα βόρεια παράλια της ανατολικής Κρήτης κι επηρεάζεται από τις Ετησίες, τους έντονους βόρειους ανέμους που οφείλονται στην αλληλεπίδραση ενός χαμηλού και ενός υψηλού βαρομετρικού συστήματος στην ανατολική Μεσόγειο που αλληλοεπιδρούν. Εκεί πραγματοποιήθηκε η πειραματική εκστρατεία «PreTECT» τον Απρίλιο του 2017. Η ιδιαίτερη τοπογραφία της Φινοκαλιάς σε συνδυασμό με το πολύπλοκο πεδίο ανέμων, σχηματίζουν ένα ενδιαφέρον πεδίο μελέτης για τη δομή του οριακού στρώματος. Το Sao Vincente στο Πράσινο Ακρωτήρι, είναι ένα μικρό νησί 227 km^2, που βρίσκεται στον Ατλαντικό και απέχει 920 km από την ακτή της δυτικής Αφρικής. Στην περιοχή αυτή, πραγματοποιήθηκε η πειραματική εκστρατεία «ASKOS» κατά τη διάρκεια των ετών 2021-2022, με εντατικές μετρήσεις τους μήνες Ιούνιο και Σεπτέμβριο. Το νησί επηρεάζεται από έντονη μεταφορά αφρικανικής σκόνης από την έρημο Σαχάρα, ενώ ταυτόχρονα χαρακτηρίζεται από το θαλάσσιο περιβάλλον με υψηλή υγρασία και ύπαρξη θαλάσσιων σωματιδίων στα χαμηλότερα στρώματα.

Η εύρεση του ύψους του ΑΟΣ πραγματοποιήθηκε με διάφορες μεθόδους που εφαρμόστηκαν στις κατακόρυφες κατανομές του συντελεστή οπισθοσκέδασης στα 532nm και 1064nm και στο προϊόν αναλογίας μίγματος υδρατμών (water vapor mixing ratio) του συστήματος PollyXT Raman Lidar, καθώς και στις κατακόρυφες κατανομές του συντελεστή οπισθοσκέδασης στα 1500nm και στο προϊόν του ρυθμού διακύμανσης τυρβώδους κινητικής ενέργειας (Turbulence Kinetic Energy dissipation rate) του συστήματος Halo Wind Doppler Lidar, στην κατακόρυφη κατανομή του συντελεστή οπισθοσκέδασης στα 532nm του δορυφορικού συστήματος Lidar CALIOP του δορυφόρου CALIPSO και τέλος στις κατακόρυφες κατανομές της υγρασίας και θερμοκρασίας των ραδιοβολίσεων. Πιο συγκεκριμένα εξετάστηκαν: η μέθοδος μετασχηματισμού κυματιδιακής συνδιακύμανσης (wavelet covariance transform), η μέθοδος βαθμίδας (gradient method), η μέθοδος κατωφλίου (threshold method), η μέθοδος πακέτου αέρα (parcel method), και τέλος η μέθοδος Richardson.

Η παραπάνω μελέτη του ΑΟΣ ανέδειξε πως και στις δύο περιοχές, τα ύψη του οριακού στρώματος ήταν χαμηλά με μικρή ημερήσια διακύμανση. Στη Φινοκαλιά Κρήτης, η διεύθυνση του ανέμου διαδραματίζει κρίσιμο ρόλο για το ύψος του οριακού στρώματος: ο δυτικός άνεμος, προερχόμενος από την ξηρά, συνεισφέρει στη δημιουργία ενός χαμηλού οριακού στρώματος που φτάνει τα 600 m, ενώ ο βόρειος άνεμος, προερχόμενος από τη θάλασσα και προσήνεμος στην ψηλή και βραχώδη πλευρά του νησιού, ευνοεί τη δημιουργία ενός ψηλού οριακού στρώματος που φτάνει το 1 km. Επιπλέον πραγματοποιήθηκε στατιστική ανάλυση των αποτελεσμάτων και τα ευρήματα από τις μετρήσεις διασταυρώθηκαν με τα αποτελέσματα του μοντέλου IFS/ECMWF. Στο Πράσινο Ακρωτήρι, η στατιστική ανάλυση των αποτελεσμάτων για το Σεπτέμβριο του 2022, ανέδειξε το ΑΟΣ της περιοχής στο ύψος των 600 m περίπου, παρουσιάζοντας καλή συμφωνία μεταξύ των αποτελεσμάτων του μοντέλου και των επίγειων μετρήσεων. Από την ερμηνεία των δεδομένων του δορυφορικού lidar πάνω από το νησί Sao Vincente αλλά και στην ευρύτερη περιοχή του Ατλαντικού, το μέσο ύψος του οριακού στρώματος προέκυψε επίσης γύρω στα 700 m, όντας σε καλή συμφωνία με το μοντέλο. Για τη μελέτη του ΑΟΣ στην ευρύτερη περιοχή, αναλύθηκαν 10 έτη δεδομένων lidar CALIPSO και μοντέλου ECMWF (2012-2022), αξιοποιώντας μόνο το μήνα Σεπτέμβριο από κάθε έτος. Αξίζει να σημειωθεί πως για το ύψος του οριακού στρώματος, παρατηρήθηκαν μεγαλύτερες διαφορές μεταξύ δορυφορικού Lidar και ECMWF στη δυτική Αφρική σε σχέση με εντός του Ατλαντικού Ωκεανού. Τέλος, στη διατριβή αναλύονται λεπτομερώς περιπτώσεις μελέτης στο Πράσινο Ακρωτήρι, διερευνώντας τις διαφορετικές περιπτώσεις θερμοδυναμικής ευστάθειας, αλλά και την ύπαρξη αιωρούμενων σωματιδίων θάλασσας και σκόνης, αξιοποιώντας όλες τις διαθέσιμες μετρήσεις επίγειου και δορυφορικού lidar, ραδιοβολίσεων καθώς και αποτελεσμάτων του μοντέλου.

Acknowledgments
ΕΥΧΑΡΙΣΤΙΕΣ

Η παρούσα διδακτορική διατριβή αποτελεί καρπό μίας συλλογικής προσπάθειας και θα ήθελα να εκφράσω την ειλικρινή μου ευγνωμοσύνη σε όλους όσοι συνέβαλαν στην ολοκλήρωσή της. Θα ήθελα πρωτίστως να ευχαριστήσω την επιβλέπουσα Καθηγήτρια Ελίνα Γιαννακάκη, για την καθοδήγηση και υποστήριξη καθ' όλη τη διάρκεια της ερευνητικής πορείας. Θερμές ευχαριστίες επίσης στην Καθηγήτρια Μαρία Τόμπρου, για την συνεχή βοήθεια που μου προσέφερε στην ανάλυση και ερμηνεία των αποτελεσμάτων, καθώς και για τις ουσιαστικές παρατηρήσεις που συνέβαλαν στη βελτίωση της παρούσας διατριβής. Στη συνέχεια, θα ήθελα να ευχαριστήσω θερμά την Καθηγήτρια Έλενα Φλόκα, την οποία γνωρίζω και εκτιμώ βαθύτατα από τα πρώτα μου βήματα στο Τμήμα Φυσικής, καθώς και την Επ. Καθηγήτρια Γεωργία Σωτηροπούλου, τον Καθηγητή Δημήτριο Μπαλή και τον Ερευνητή Δρ. Στέλιο Καζαντζή για τη συμβολή τους με τις γνώσεις και τις χρήσιμες παρατηρήσεις.

Ευχαριστώ από καρδιάς τον επιβλέποντα Δρ. Βασίλη Αμοιρίδη, Διευθυντή ερευνών του Εθνικού Αστεροσκοπείου Αθηνών, καθώς και τη Δρ. Ελένη Μαρίνου, Ερευνήτρια του Εθνικού Αστεροσκοπείου Αθηνών. Κατά τη διάρκεια της εκπόνησης της παρούσας διατριβής, μου έδωσαν επιστημονική και ηθική υποστήριξη, πρωτοπόρες ιδέες, και δε σταμάτησαν στιγμή να με παροτρύνουν προς το καλύτερο, διαμορφώνοντας το ακαδημαϊκό μου ήθος. Η εμπειρία τους και η συμβολή τους ήταν καθοριστική για την πορεία και την ολοκλήρωση της διατριβής.

Επιπλέον ευχαριστώ την ομάδα ReACT, για τη συνεργασία με υπέροχους και άξιους ανθρώπους. Ειδικές ευχαριστίες στο Μαράκι, την Περιστέρα, την Άννα Γ. (που μου έμαθε τόσα πολλά), την Σταυρούλα, την Άννα Κ., το Γιώργο, το Θανάση, την Ελένη Δ. και τη Δήμητρα, που έκαναν τη δουλειά να κυλάει με χαμόγελο κα ευχαρίστηση.

Ολόψυχα ευχαριστώ τις φίλες και συμπαίχτριές μου, που με βοηθούσαν να διαχειριστώ την ένταση και τη ψυχολογική πίεση που συνοδεύει κάθε διδακτορική διατριβή, με στήριξαν με στιγμές χαράς και βοήθησαν να ξεπεράσω τα αδιέξοδα.

Θα ήθελα να ευχαριστήσω τον άνθρωπό μου, τον αγαπημένο μου Νικηφόρο Μανδηλαρά, που έδειξε κατανόηση, συνέβαλε καταλυτικά σε αυτό τον προσωπικό αγώνα και με βοήθησε να δω τα πράγματα καθαρά.

Το μεγαλύτερο ευχαριστώ ανήκει στην οικογένειά μου, τον πατέρα μου Δημήτρη, τη μητέρα μου Μαίρη και την αδερφή μου Όλγα, που έδωσαν απλόχερα την έμπρακτη στήριξή τους, όπως έκαναν πάντα σε κάθε βήμα της ζωής μου.

Ιωάννα Τσικουδή
Αθήνα, 6 Μαΐου 2025.

Contents

List of Figures

List of Tables

List of Abbreviations

ABL	Atmospheric Boundary Layer
AMMA	African Monsoon Multidisciplinary Analyses
a.m.s.l.	above mean sea level
AOD	Aerosol Optical Depth
ASKOS	Campaign link
BSC	Backscatter Coefficient
BL	Boundary Layer
C3S	Copernicus Climate Change Service
CALIOP	Cloud-Aerosol Lidar with Orthogonal Polarization
CALIPSO	Cloud-Aerosol Lidar and Infrared Pathfinder Satellite Observations
CI	Capping Inversion
CNES	Centre National D'Études Spatiales
CPV	Cape Verde
CV	Cabo Verde
CWT	Continuous Wavelet Transform
DOD	Dust Optical Depth
EarthCARE	Earth Cloud Aerosol and Radiation Explorer
ECMWF	European Centre for Medium-Range Weather Forecasts
EO	Earth Observations
ESA	European Space Agency
EZ	Entrainment Zone
FF	Far Field
GFS	Global Forecast System
HYSPLIT	Hybrid Single-Particle Lagrangian Integrated Trajectory
IBL	Internal Boundary Layer
ITCZ	Intertropical Convergence Zone

JATAC	Joint Aeolus Tropical Atlantic Campaign
L2	Level 2
L3	Level 3
LIDAR	LIght Detection And Ranging
LIVAS	LIdar climatology of Vertical Aerosol Structure for space-based lidar simulation studies
MABL	Marine Atmospheric Boundary Layer
MBE	Mean Bias Error
MBL	Marine Boundary Layer
MLH	Mixing Layer Height
MLH_{TKE}	Mixing Layer Height retrieved from TM on TKE_{dr} of Halo Wind Lidar
MODIS	Multi-angle Imaging Spectro-Radiometer and Polarization and Directionality of the Earth's Reflectance
MWR	Microwave Radiometer
NASA	National Aeronautics and Space Administration
NCEP	National Centers for Environmental Prediction
N, E, S, W	North (0°/360°), East (90°), South (180°), West (270°)
NF	Near Field
NOA	National Observatory of Athens
NWP	Numerical Weather Prediction
OSCM	Ocean Science Centre Mindelo
PANGEA	PANhellenic GEophysical observatory of Antikythera
PBL	Planetary Boundary Layer
PBL_{BSC}	Planetary Boundary Layer height retrieved from WCT on BSC of Halo Wind Lidar
$PBL_{ECMWF_{LAND}}$	PBL height from ECMWF bin above land
$PBL_{ECMWF_{SEA}}$	PBL height from ECMWF bin above sea
PBL_{RCS}	Planetary Boundary Layer height retrieved from WCT on RCS from 532nm NF channel of PollyXT Lidar
PBL_{WVMR}	Planetary Boundary Layer height retrieved from WCT on WVMR of PollyXT Lidar
PM	Parcel Method
PollyXT	Portable Lidar System: the neXT generation
PreTECT	Campaign link

RCS	Range Corrected Signal
RL	Residual Layer
RS	Radiosonde
RM	Richardson Method
SBL	Stable Boundary Layer
SNR	Signal-to-Noise-Ratio
SST	Sea Surface Temperature
TKE_{dr}	Turbulent Kinetic Energy dissipation rate
TM	Threshold Method
UTC	Coordinated Universal Time
V4	Version 4
VLDR	Volume Linear Depolarization Ratio
WCT	Wavelet Covariance Transform
WRF	Weather Research and Forecasting
WVMR	Water Vapor Mixing Ratio

Chapter 1

Introduction

Research Outline

The Atmospheric Boundary Layer (ABL) is a critical component of the atmosphere, as it represents the interface where the Earth's surface interacts with the air above, and shapes directly the environmental conditions humans live in (e.g. Seibert et al. 1998). The atmospheric dynamics of the lower troposphere that directly influence ABL characteristics, are shaped by the surface exchange of momentum, heat and moisture (e.g. Pastor et al. 2001; Belamari and Céron 2005), as well as the topography (e.g. Benjamin and Carlson 1986; Benjamin 1986). Understanding and quantitative knowledge of ABL dynamics are crucial for a wide range of applications, including air quality (e.g. Han et al. 2009; Stirnberg et al. 2021; Sujatha et al. 2016) or greenhouse gases (e.g. Lauvaux et al. 2016), the generation of renewable energy (e.g. Peña et al. 2016), numerical weather prediction (NWP; e.g. Illingworth et al. 2019), sustainable urban planning (e.g. Barlow et al. 2017), and all aspects of transportation such as aviation, shipping, or road safety (e.g. Vajda et al. 2011). The dissertation focuses on the boundary layer characteristics shaped in marine environments (Marine Atmospheric Boundary Layer - MABL). MABL is influenced by physical processes across multiple scales, including large-scale phenomena such as synoptic weather systems, mesoscale phenomena like sea breezes, and small-scale processes such as turbulence, convection, and wave-induced mixing (Edson et al., 1999, 2007). A better understanding of how different air-sea processes can act by themselves or interact with each other to enhance or reduce surface exchange of energy and momentum is of interest from a global climatological point of view, as 70% of Earth's surface is covered by ocean (Yu, 2019). The interaction and the energy exchange of atmosphere-ocean system, are the predominant physical mechanism characterizing the development of the MABL as well as the weather patterns and oceanic heat transport, that shape the climate (Bjerknes, 1964).

The parameters that define the MABL dynamics, are studied by the scientific community with modelling (e.g. Faloona 2009), air-borne or ground-based in-situ (e.g. Zemba and Friehe 1987; Pezzi et al. 2005), satellite remote sensing (e.g. Luo et al. 2016; Young et al. 2000) and surface-based remote sensing (Peña et al., 2008; Luo et al., 2014). Over the ocean, the surface layer of the MABL is often described using the Monin–Obukhov Similarity Theory Monin and Obukhov (1954), where turbulent fluxes of momentum heat and moisture, are parametrized based on the Monin–Obukhov length. However, under specific meteorological conditions or topography, MABL can have complex behavior and present distinct characteristics, for instance in close basins such as the Aegean Sea, where the Etesian patterns strongly affect the wind fields (Tombrou et al., 2015; Portalakis et al., 2021), or in open ocean (Edson et al., 2007). Over the open Atlantic, the MABL is typically shallow and influenced by the relatively constant sea surface temperature, while coastal BLs are affected by terrestrial-marine interactions that increase their variability (Fairall et al., 2006).

In this dissertation, we focus on regions such as the Aegean Sea and the northern tropical Atlantic. Both areas are affected by high concentrations of transported aerosols from nearby natural sources (e.g. Amiridis et al. 2024; Carlson 2016). Aerosols also play a critical role in shaping the dynamics of the MABL since they influence radiative transfer, cloud formation, and precipitation processes, all of which are integral to the energy balance and thermodynamic structure of the MABL (e.g. Bates et al. 2001; Fairall and Davidson 1986; Katoshevski et al. 1999; Russell et al. 1994). Furthermore, marine aerosols emitted at the ocean surface, primarily sea salt and secondary organic particles, modulate the microphysical properties of clouds by acting as cloud condensation nuclei (CCN) (Kristensen et al., 2016). This, in turn, affects cloud albedo, lifetime, and coverage, leading to feedback on atmospheric stability and turbulence (Hudson, 1993; Farmer et al., 2015). Finally, aerosols influence the exchange of heat and moisture at the ocean-atmosphere interface, which directly impacts the stratification and vertical mixing within the boundary layer (Vignati et al., 2001; Kudryavtsev and Makin, 2011). These processes are further complicated in regions with mixed aerosols, such as those influenced by long-range transported desert dust or anthropogenic pollutants, which can alter the optical and hygroscopic properties of the aerosol population. Therefore, in this thesis to better understand local atmospheric dynamics, we investigate the impact of land and sea surface heterogeneity as well as the impact of aerosols on the evolution of the MABL.

Historically, our fundamental understanding of the boundary layer comes from measurements (see for example Stull 2012). For instance, Baars et al. (2008) describe the continuous monitoring of the boundary layer top with lidars, while several studies have measured the ABL evolution in urban sites over Greece (Amiridis et al., 2007, Kokkalis et al., 2020, Tsaknakis et al., 2011). Although field measurements represent the reality by definition, this reality is composed of the superposition of many simultaneous local effects and processes. Boundary layer vertical profiles have historically been obtained primarily through radiosonde measurements, which provide information about atmospheric thermodynamics and winds (e.g. Dourado and Oliveira 2001). However, radiosondes have limitations, including low temporal resolution due to typically sparse launch intervals and spatial inaccuracies caused by the horizontal drift of the balloons as they ascend (Seidel et al., 2011). These constraints introduce challenges in capturing the continuous and localized evolution of the ABL. To address these gaps, remote sensing techniques such as lidar, offer an alternative by providing high-resolution, and continuous observations. It is consequently suitable to use measurements synergistically to describe the observed ABL behavior. Observing the MABL is particularly complex due to limited ground-based observation sites over ocean. Given this constraint, satellite observations, such as those provided by space profilers (e.g. the Cloud-Aerosol Lidar and Infrared Pathfinder Satellite Observations - CALIPSO mission, Winker et al. 2003), have become essential for studying lower troposphere characteristics over remote regions, offering a means to improve understanding of these complex systems. Various methods have been employed to determine the ABL or MABL height, with the Wavelet Covariance Transform (WCT) (Brooks, 2003) and the Gradient Method (Li et al., 2023) being among the most widely used. The WCT method excels in identifying sharp changes in the profile of an atmospheric variable, for instance the backscattering profiles of Lidars (Li et al., 2020). In this dissertation different modifications of the methods are applied, in order to demonstrate a reliable boundary layer height. The Gradient Method leverages gradients such as potential temperature, humidity, or wind speed, providing a robust approach for both radiosonde and remote sensing data (Hennemuth and Lammert, 2006). The strengths and limitations of each method are discussed, along with their applicability that often depends on the data type, resolution, and the specific characteristics of the ABL in the areas of interest.

To investigate the characteristics of the boundary layer in different marine environments, this study targets on two regions in the Eastern Mediterranean and the Atlantic Ocean. Despite the critical importance of these areas for understanding air-sea interactions and their climatological implications, ground-based measurements of the boundary layer remain sparse, limiting our ability to interpret the complex dynamics in these key regions (Kotthaus et al., 2023). We initially focus on the Finokalia station of Crete, as a site of complex topography, affected by different wind fields in the Aegean Sea. Numerous interesting studies have been conducted on this site, focusing inside the boundary layer. For instance, Kalivitis et al. (2012, 2015) and Bougiatioti et al. (2009) investigated CCN mechanisms and atmospheric ion concentrations, while Eleftheriadis et al. (2006) examined the size distribution, composition, and origin of submicron aerosols. Dandou et al. (2017) examined turbulence schemes over the Aegean Sea during Etesian winds and found that while the MABL was generally shallow, its simulated depth varied significantly across schemes depending on atmospheric stability and parameterization. Furthermore, air masses of different origins present significant variations in the height of the boundary layer in this region (Tsikoudi et al., 2022). These variations arise from the distinct thermodynamic properties, aerosol content, and moisture levels associated with each air mass, which influence the stability, turbulence, and energy fluxes within the MABL. Then, we focus on the MABL dynamics of the northern tropical part of the central Atlantic Ocean, with intensive measurements from Cabo Verde Archipelagos. Cabo Verde region encompasses convective conditions and unique MABL vertical structure and extent as it is a site of high mineral dust concentrations (Sun and Zhao, 2020), under the influence of oceanic climate. Carpenter et al. (2010) studied the seasonal characteristics of tropical marine boundary layer structure measured at the Cabo Verde and discussed certain aspects of the MABL dynamics. These dynamics are affected by the general circulation that is dominated by the Inter-Tropical Convergence Zone (ITCZ) characteristics, while the region is rich in aerosols due to the advection of Saharan dust and the formation of the Saharan Air Layer (SAL) in the free troposphere (Dunion and Velden, 2004). The ITCZ migrates seasonally between the northern and southern tropics and this movement influences rainfall and convective activity, creating conditions conducive to both the formation of clouds and the upward transport of aerosols over the Atlantic (Zhou et al., 2020). In tandem, the SAL—comprising hot, dry air laden with desert dust from the Sahara—moves westward across the Atlantic Ocean, especially in summer, driven by the prevailing trade winds (Prospero and Mayol-Bracero, 2013).

The primary objective of this dissertation is to extend the scientific knowledge on

MABL dynamics by utilizing and comparing the unique capabilities of different remote sensing methods and range of instrument profilers. More specifically, the aim of this study is twofold: First, to demonstrate the effectiveness of remote sensing synergies and methods in studying the vertical structure of the lower troposphere. Second, to investigate in detail how the existence of desert dust and marine aerosols impact the formation of boundary layer. The specific research questions driving this thesis are:

- What are the most effective and reliable methods for studying the boundary layer evolution?

- In what ways do aerosols impact the dynamics and structure of the MABL?

- What are the defining characteristics of the MABL in complex coastal sites?

- To what extent do models capture the boundary layer evolution?

To address these objectives, we use data from the PreTECT campaign which took place in April 2017, at Finokalia of Crete (cf. Marinou et al. 2021) and from the ASKOS experimental campaign (2021–2022) in Sao Vicente Island in Cabo Verde (cf. Marinou et al. 2023), situated in the Atlantic Ocean. Satellite lidar observations from CALIPSO were also employed to examine the MABL's behavior over the Atlantic, uncovering patterns and differences associated with dust transport.

Understanding the structure of the MABL and detecting the top reliably, remains an open question in many cases and an active area of research, particularly in heterogeneous environments where traditional observation methods may fall short. This thesis proposes a synergy of instruments and methodologies to address the complexities of the ABL in marine environments and its relationship with aerosol presence. By classifying meteorological and aerosol conditions, this work aims to shed light on MABL processes and contribute to improve forecasts of coastal winds, pollutants dispersion, and precipitation patterns.

Structure

The first part of this thesis addresses the technical aspects of measuring the MABL. Various methods for deriving the MABL top and understanding its dynamics are explored in detail, including the Wavelet Covariance Transform (Brooks, 2003; Nakoudi et al., 2019; Dang et al., 2019; Zhong et al., 2020; Kim et al., 2021; Granados-Muñoz et al., 2012), Gradient (Lammert and Bösenberg, 2006; de Arruda Moreira et al., 2022), Richardson (Hong, 2010; Shin and Hong, 2011), Parcel (Holzworth, 1964), and Threshold methods (Dang et al., 2019; Baars et al., 2008). Each method's advantages, limitations, and applications are discussed, along with the implications of the variables to which these methods are applied. This study demonstrates that the choice of atmospheric variable significantly influences the results. For instance, using backscatter as a tracer for the ABL top may yield different results than applying the same method to water vapor mixing ratio or potential temperature profiles, highlighting the importance of selecting the appropriate parameter for specific applications.

The second part of this thesis is motivated by the above-mentioned complexities of lower troposphere in marine environments influenced also by aerosols. The sharp contrasts in temperature, moisture, and surface roughness between land and sea can lead to unique turbulence and mixing processes. After establishing the most effective methods and emphasizing the importance of a multi-sensor approach, the study focuses on interpreting results in these challenging environments, as coastal areas are inherently more complex than continental regions.

The thesis is organized into six chapters, guiding the reader through the study of the ABL meteorology by using remote sensing measurements, analytical methods, and investigating site-specific dynamics in coastal and marine environments. Chapter 1 introduces the research outline, objectives, and the overall structure of the thesis, setting the initial stage for exploring of MABL dynamics and the influences that shape its behavior. The emphasis is placed on the challenges of varied geographical settings, particularly coastal regions with complex terrain, such as Finokalia, Greece, and marine locations influenced by desert dust like Cabo Verde.

Chapter 2 provides the theoretical background on the ABL, including key definitions and characteristics. The critical role of aerosols in boundary layer dynamics, stability, moisture, and thermal properties is discussed. This chapter also introduces the measurement techniques employed, describing the data sources and instrumentation used in the study. The active remote sensing tools include ground-based lidars, namely the PollyXT Raman Lidar and the Halo Wind Doppler lidar, as well as the CALIPSO satellite-based lidar observations, complemented by radiosonde measurements to capture vertical profiles essential for understanding MABL structure.

The methodological framework is detailed in Chapter 3, which reviews and applies various approaches for determining the boundary layer height, including the Wavelet Covariance Transform, gradient method, threshold method, Richardson method, and parcel method. In chapters 4 and 5, methods are applied in selected case studies: the former focuses on MABL characteristics at Finokalia, analyzing PreTECT campaign data under diverse meteorological conditions, while the latter examines the MABL in the Atlantic region using data from the ASKOS campaign in Cabo Verde, with a focus on the impact of desert dust on ABL structure and evolution. An overview of the experimental campaigns, including their locations, instrumentation, periods of operation, and methods to acquire the ABL height is provided in Table 1.1. Finally, Chapter 6 synthesizes the findings of the study and discusses future research directions, proposing improvements in measurement approaches and modeling for enhanced understanding of ABL dynamics in coastal and marine settings.

Methods of Acquiring the Boundary Layer Height	
	Wavelet Covariance Transform Method Gradient Method Threshold Method Richardson Method Parcel Method
ABL Characteristics at a coastal site	
	Location: Finokalia, Crete, PreTECT Campaign 2017 Instruments: PollyXT Raman & Halo Wind Doppler Lidar ↬Cases analyzed in detail, Statistical Analysis
ABL in the Atlantic: the desert dust impact	
	Location: São Vicente, Cabo Verde ASKOS Campaign 2022 Instruments: PollyXT Raman & Halo Wind Doppler Lidar CALIPSO, radiosondes ↬Area 1: open ocean, ITCZ ↬Area 2: the ocean-desert transition zone ↬ABL in Mindelo of Cabo Verde

Table 1.1: Summary of the methods to acquire the ABL height, locations, field campaigns, and analysis included in this dissertation.

Chapter 2

Theory and Measurement of the ABL

2.1 Historical Overview

The study of the Atmospheric Boundary Layer (ABL) has developed significantly over the past century, propelled by advances in observational technology and theoretical frameworks. The scientific exploration of the atmosphere began in earnest in the mid-18th century (Bjerknes, 1964). The early 20^{th} century, researchers recognized the importance of the atmosphere's lowest layer, the boundary layer, which interacts directly with the Earth's surface.

Lewis Fry Richardson introduced a theory linking atmospheric turbulence to the ratio of buoyant forces and shear (Richardson, 1921) in the 1920s. The Richardson number, a dimensionless quantity, became essential for predicting whether atmospheric layers would be turbulent or laminar. This parameter remains a cornerstone in understanding ABL stability and turbulence generation, allowing to categorize layers as either favorable to turbulence or suppressive of it, depending on the thermal and wind gradients present.

Radiosondes, provided valuable unforeseen vertical profiles of temperature, humidity, and pressure in the 1930s, that greatly enhanced the understanding of ABL's vertical structure. Around the 1940s and 1950s, the Monin-Obukhov Similarity Theory furthered ABL research by modeling turbulence and fluxes near the surface, establishing a theoretical basis still widely used in boundary-layer studies (Khanna and Brasseur, 1997). In the same era, the construction of wind profilers and meteorological towers enabled real-time observations of wind and turbulence profiles, essential for studying ABL dynamics.

The 1960s brought a leap forward with the application of remote sensing technologies, such as radar and lidar, allowing continuous, non-intrusive measurements of the ABL's depth and structure (Schwiesow, 1986). These instruments have become indispensable in observing the ABL's behavior across different environments. Since then, ABL studies have expanded to cover a wide range of topics, including extreme weather impacts, urban boundary-layer effects, air quality, cloud-ABL interactions, and marine boundary-layer dynamics. The growing diversity in ABL research reflects its critical role in numerous fields, from weather forecasting and climate modeling to environmental management and pollution monitoring. McBean (1986), from the early years explored the ABL characteristics over snow, ice and water surfaces while Emeis (2010) describes in detail the Surface-based remote sensing of the atmospheric boundary layer. A recent study presents the review of current challenges and a new generation of machine learning techniques

(Canché-Cab et al., 2024).

2.2 ABL Dynamics and Structure

In boundary layer science, the term 'dynamics of the boundary layer' refers to the processes that govern its movement, evolution, and interactions with the Earth's surface and the free atmosphere above. This includes the complex mechanisms of turbulence, mixing, and energy exchange that shape the BL's behavior. Specifically, it involves how air parcels move within this layer, how momentum, heat, and moisture are transferred between the Earth's surface and the air above, and how larger atmospheric systems interact with these processes. BL dynamics are influenced by factors like wind shear, surface heating and cooling, topography, and the presence of aerosols or other particulate matter, which all contribute to creating an evolving, often turbulent environment (Cebeci, 2012).

2.2.1 Evolution of the ABL

The atmosphere near the Earth's surface responds dynamically to the daily cycle of sunlight and darkness, leading to regular patterns of heating and cooling over a 24-hour period. The diurnal cycle of the ABL refers to the daily evolution of the layer, driven primarily by these changes. This cycle governs how the ABL changes in depth over a 24-hour period, involving the formation and dissipation of several key sub-layers, including the nocturnal layer, convective layer, residual layer, mixing layer, entrainment zone, and surface layer.

During the day, as the sun rises and warms the Earth's surface, the surface layer within the ABL begins to heat up, creating a convective layer dominated by rising warm air parcels. This process enhances turbulence and vertical mixing, creating small eddies that lead to thickening of the boundary layer. This daytime ABL, often referred to as the Mixing Layer (ML), grows steadily as surface heating increases, causing air to rise and creating buoyancy-driven, or convective, turbulence. As it rises, the mixing layer reaches a transition zone known as the Entrainment Zone (EZ), where it interacts with the more stable air of the free atmosphere above. This entrainment process allows air from the free atmosphere to mix down into the boundary layer, adding to its depth. Clauser (1956) present a simple case of the turbulent boundary layer in a constant pressure field and consider the complex problem of the effects of pressure gradients, and variable wall roughness, while discussing the assumption of a constant outer viscosity has been investigated only for the case of equilibrium layers.

By afternoon, the ABL typically reaches its maximum height as a result of sustained heating, at which point it may contain thermals that transport heat and moisture upward, and any aerosols or pollutants near the surface are thoroughly mixed throughout this layer. Observations of the afternoon transition of the Convective Boundary Layer (CBL) are presented in the study of Grimsdell and Angevine (2002), where the behavior of the portion of the CBL remaining in contact with the surface, becomes very similar with the CBL beginning to decay earlier in the day, simply because of the weaker turbulence conditions. The surface layer (extending only a few tenths of meters above the surface) remains closest to the ground and is highly influenced by direct interactions with the Earth's surface, leading to the strongest temperature and humidity gradients in this sub-layer.

As night falls and solar heating ceases, radiative cooling at the surface causes the boundary layer to gradually contract, and the convective turbulence from the day is replaced by more stable conditions. A shallow nocturnal Stable Boundary Layer (SBL) forms near the ground, often only a few hundred meters thick, as cooling suppresses vertical mixing. Nieuwstadt (1984) was one of the first scientists that studied in detail the Turbulent Structure of the stable, nocturnal boundary layer, by using measurements from a meteorological mast, analyzing characteristic profiles of wind speed, direction and potential temperature in the SBL. Above this, the Residual Layer (RL)—a remnant of the previous day's convective mixing layer—persists with weaker turbulence and retains the daytime properties, such as aerosol concentrations and temperature gradients. However, it is decoupled from the surface and gradually becomes more stable as the night progresses. Blay-Carreras et al. (2014) investigated the role of the RL and large-scale subsidence on the development and evolution of the CBL. They used observations from different campaigns and simulated the evolution of the RL and CBL. The Capping Inversion (CI) separates the boundary layer from the free atmosphere above, effectively capping the mixing. Usually the inversions of the atmospheric parameters at the top of the boundary layer take place in the CI. The EZ and the CI could overlap, but the first usually exists when the daytime mixing layer develops, while the latter generally constrains vertical mixing between free troposphere and the air below. Lock (2009) investigated the factors influencing cloud area at the capping inversion for shallow marine cumulus clouds and performed large-eddy simulations. Rampanelli and Zardi (2004) developed a method to determine the Capping Inversion of the Convective Boundary Layer.

The next morning, the cycle begins again. The nocturnal layer dissipates as the sun rises and the surface warms, eventually re-establishing the convective mixing that builds up the ABL once again. Duncan Jr et al. (2022) recently conducted a comprehensive research on evaluating the CBL height estimations resolved by both active and passive remote sensing instruments. This regular diurnal evolution, driven by heating and cooling cycles, results in distinctive ABL profiles that vary widely between day and night.

Each phase of this cycle is crucial for understanding boundary layer processes, as the dynamics of each sub-layer and their transitions impact everything from pollutant dispersion to energy fluxes and cloud formation. The boundary layer's diurnal cycle showcases the continuous and complex interplay of atmospheric processes that define this important region closest to Earth's surface.

McNider and Pielke (1981) studied the Diurnal boundary-layer development over sloping terrain, concluding to the development of a mesoscale thermal wind component to the south during the day throughout the convective boundary layer, by using model results and an analysis of thermal wind relationships in the transformed equations. Whiteman et al. (2000) focused on the Mexican plateau to study the diurnal evolution of ABL, and discovered that the air that converges onto the plateau comes from elevations at and above the plateau, was modified earlier in the day by a cool, moist coastal inflow carried up the plateau slopes by the plain-plateau circulation. This shows how important are the local effects of each area and the meteorological conditions for the diurnal pattern of ABL.

2.2.2 Marine Atmospheric Boundary Layer

The characteristics and dynamics of the ABL are shaped by various factors, such as geography, meteorology, and human activities. One of the most fundamental distinctions in its behavior arises from the contrast between marine (oceanic-coastal) and continental (land-based) environments. The nature of the underlying surface —whether land or sea— determines key physical properties (heat capacity, moisture availability, and surface roughness), influencing the structure, evolution, and processes within the ABL. Understanding these differences is essential for accurately modeling atmospheric processes and interpreting observational data.

This dissertation focuses on marine-influenced environments. Specifically, we investigate the ABL in coastal regions such as Finokalia, located along the Aegean Sea — a partially enclosed basin within the eastern Mediterranean — and Cabo Verde, situated in the open Atlantic Ocean. Despite their geographical differences, both regions are characterized by their proximity to the sea and the associated high humidity conditions.

An important indirect factor influencing the ABL over marine regions is the heat capacity of the underlying surface. Water has a much higher specific heat capacity than land, meaning that it can absorb and retain larger amounts of heat. As a result, ocean surface temperatures change gradually over the course of the day, and the sea surface temperature (SST) remains relatively stable, so the air above it typically maintains a more constant temperature and humidity. During daylight hours, the sea heats up more slowly and releases heat more gradually at night. This leads to a boundary layer less affected by rapid temperature fluctuations. These relatively uniform conditions over the ocean help promote steady turbulent mixing, although sea surface temperature gradients can still drive significant wind patterns, such as the sea breeze (Miller et al., 2003). In contrast, land surfaces would exhibit more rapid temperature fluctuations due to their lower heat capacity. This thermal inertia of the sea leads to more stable boundary layer conditions and dampens the diurnal temperature cycle. As shown by Joshi et al. (2008), the disparity in heat capacity between land and ocean contributes significantly to differences in surface temperature responses under climate change scenarios, which in turn affect the development and structure of the ABL.

It is important to note that coastal and marine are not exactly the same thing, although they are closely related in the context of ABL studies. Marine environment refers specifically to areas dominated by open ocean or large bodies of water, such as the open sea. In the case of ocean, the conditions are influenced primarily by the sea's characteristics, such as SST, salinity, and moisture content in the air (e.g. Zemba and Friehe, 1987). A MABL typically experiences uniform mixing and gradual temperature changes, while the surface latent heat flux over the ocean is strongly correlated with its structure (Palm et al., 1999). Díaz et al. (2019) studied the long-Term Trends in MABL properties over the Atlantic Ocean. In coastal areas, where the sea meets the land, there is often a combination of land and marine ABL characteristics (e.g. Schafer et al., 2001). During the day, the ABL may grow more rapidly over land due to strong convective heating, while MABL typically do not present daytime evolution. This differential behavior can lead to complex interactions between the two layers, and is particularly evident in phenomena such as the Internal Boundary Layer (IBL) (Garratt and Ryan, 1989), which forms at the interface between two contrasting air masses. The IBL is especially pronounced when a colder marine layer moves over a warmer land surface or vice versa. This can result in vertical layering within the ABL, with sharp changes in temperature, moisture, and wind profiles.

A detailed study that examines the distinctions between continental and marine boundary layers is the one by Kante et al. (2012). They analyze and compare relative humidity, dew point temperature, wind speed and direction vertical profiles, and atmospheric boundary layers of continental, coastal, and marine sites located in West Africa. The findings indicate that the maximum thickness of the boundary layer is observed on the continent during the day, while at night, the marine boundary layer is the thickest. Additionally, the diurnal evolution shows that the mixing layer thickness decreases during the night over the continent but increases at the coast and at sea. The study also notes that the continental boundary layer is more unstable during the day, whereas at night, the marine boundary layer exhibits greater instability compared to the coastal and inland ones. Moreover, Luo et al. (2014) briefly described the Lidar-based remote sensing of atmospheric boundary layer height over land and ocean and Aryee et al. (2020) provided a comparative assessment of boundary layer characteristics using the African Monsoon Multidisciplinary Analyses (AMMA) radiosonde network data over West Africa. These studies consistently highlight the dynamic contrast in boundary layer depth, turbulence, and moisture structure between land and ocean sites. Similarly, Choi and Noh (2020) analyzed the differences in turbulent processes between atmospheric and oceanic boundary layers during convection. Jiang and Wang (2021) explored the development of stable internal boundary layers over cooler coastal waters, highlighting the variability in turbulence characteristics, and Chen et al. (2023) investigated the impact of continental and marine sources on boundary layer properties in the Cape Grim coastal region.

The latitude of a region further complicates the ABL dynamics. In tropical or equatorial regions, the marine boundary layer is often deeper, and the trade winds help maintain a continuous mixing process, although the intensity of convection can still vary depending on the region's proximity to land and seasonal factors (Carrillo et al., 2016). In contrast, continental ABLs in temperate or polar regions experience much more variability, with pronounced seasonal changes and greater shifts in atmospheric conditions (Heinemann, 2008).

Overall, on marine environments, island and coastal sites, the ABL tends to be more homogeneous, with smaller temperature gradients and less diurnal variation. The high moisture levels in these regions also play a key role in influencing the ABL, making it more prone to cloud formation and more stable compared to dry continental areas, where lower moisture levels allow greater heating and cooling.

2.2.3 The Role of Aerosols in the ABL

The particles suspended in the atmosphere, so called aerosols, originate from natural sources such as volcanoes, deserts, forest and grassland fires, terrestrial and oceanic vegetation and sea sprays from the oceans, but also arising from anthropogenic sources. The latter include the burning of fossil and bio-fuels through industrial activities, transportation systems, and urban heating, along with land cover/land use changes, e.g. biomass burning, deforestation, and desertification (Diner et al., 2004).

Although aerosol is technically defined as a suspension of fine solid or liquid particles in a gas, common usage refers to the aerosol as the particulate component only. The size of the atmospheric aerosol particles ranges from a few nanometers (nm) to tens of micrometers (μm) in radius. Once airborne, they can change their size and composition by several ways: (i) by condensation of vapor species (Kolb and Worsnop, 2012), (ii) by evaporation (McMurry, 2000), (iii) by coagulating with other particles (Suck and Brock, 1979), (iv) by chemical reaction (Katrib et al., 2005), or (v) by activation in the presence of water supersaturation (Shen et al., 2018) resulting in the formation of fog and cloud droplets. Particles smaller than 1 μm have atmospheric concentrations in the range of around ten to several thousand per cm^3. Particles exceeding 1 μm are usually found at concentrations less than 1 cm^{-3} (Seinfeld and Pandis, 2016). The Particles are removed from the atmosphere by two mechanisms: deposition at the Earth's surface (dry deposition) and incorporation into cloud droplets during the formation of precipitation (wet deposition). Tropospheric aerosols vary widely in concentration and composition, since the geographic distribution of particle sources is highly non-uniform and the wet and dry deposition lead to relatively short residence times in the troposphere. Their residence times in the troposphere vary from a few days to few weeks (Seinfeld and Pandis, 2016).

Aerosols act as important tracers of ABL dynamics in many studies (Groß et al., 2016; Kanitz et al., 2014; Mona et al., 2006) because their distribution and concentration provide valuable information about mixing, transport processes, and the interactions between the ABL and the free atmosphere above. Moreover they interact with the solar radiation and modify the energy budget. The different types of aerosol-radiation interactions constitute the aerosol radiative forcing and are presented in Figure 2.1. The forcing from direct aerosol–radiation interactions encompasses the scattering and absorption of sunlight from the particles and cor-responds to what is usually referred to as the aerosol "direct" effect (Change, 2007). The presence of aerosols influences the thermal and moisture properties of the boundary layer, affecting its stability and depth. They can also serve as markers for turbulence and the vertical structure of the ABL, as their concentration tends to decrease with altitude in a well-mixed layer and may show distinct layering patterns during periods of reduced mixing (Heinold et al., 2008; Cuesta et al., 2009). Technically, the ABL top can be identified as the point where the aerosol concentration profile sharply decreases. In urban areas, this typically corresponds to anthropogenic aerosols such as pollutants and biomass burning emissions. In contrast, marine environments often feature aerosols from natural sources, such as sea spray. Lidar systems provide data for this analysis by measuring the backscatter coefficient, which quantifies aerosol concentration vertically throughout the atmosphere.

Compared to other aerosol types, desert dust contributes substantially to the aerosol load with wind acting on bare land surfaces being the main source for mineral particles in the atmosphere. Gkikas et al. (2022) quantified the dust optical depth (DOD) and its uncertainty across spatiotemporal scales between 2003 and 2017 at global and regional levels. The most active dust sources are predominantly situated in semi-arid and arid regions at sub-tropical latitudes where subsiding air masses stabilize the atmosphere and dry climates prevail (Schepanski, 2018). Figure 2.2 shows the global major dust sources. In terms of dust emission flux and frequency of events, the largest global source is the Sahara Desert located in the Sahara-Sahel region of Northern Africa and the second largest is the central Asia (Prospero et al., 2002; Washington et al., 2003; Seinfeld and Pandis, 2016). As mentioned in 1, this dissertation focuses on two sites: Finokalia in Crete, and São Vincente in Cabo Verde. Both sites are influenced by dust aerosols, as they are located

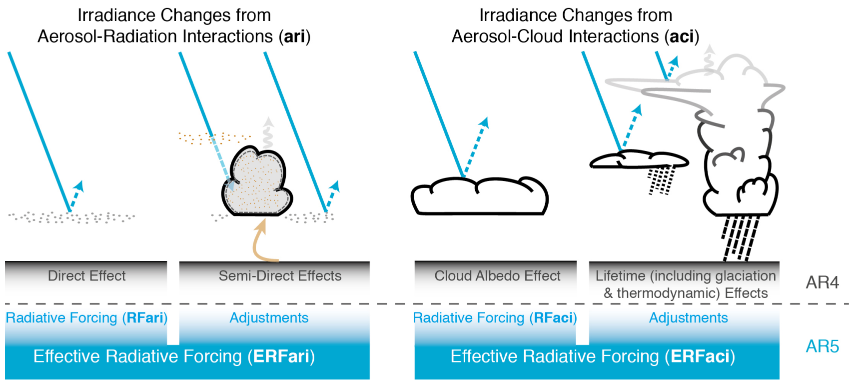

Figure 2.1: Schematic of the aerosol–radiation and aerosol–cloud interactions. The blue arrows depict solar radiation, the grey arrows terrestrial radiation and the brown arrow symbolizes the importance of couplings between the surface and the cloud layer for rapid adjustments (Fig. 7.3 from Change, 2007).

in the southeastern Mediterranean and the northern tropical Atlantic—regions relatively, close to dust emission sources (see Fig. 2.2). Atmospheric circulation strongly governs the amount of dust transported to each site, shaping the aerosol conditions observed.

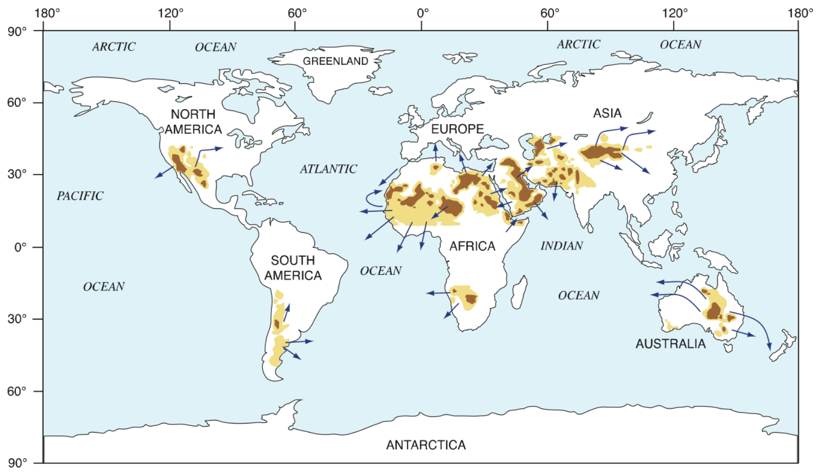

Figure 2.2: Map of global dust sources, based on multiple years of satellite imagery (TOMS). Dark brown is 21–31 days; yellow is 7–21 days (Redrawn from Fig. 4 of Prospero et al., 2002). Blue arrows indicate typical dust transport path-ways, based on interpretation of MODIS observations (Knippertz and Stuut, 2014). Figure from Muhs et al. (2014)

Desert dust aerosols that are transported over the Atlantic and the Mediterranean from Africa, introduce another layer of complexity in troposphere dynamics and clouds activity (Marinou et al., 2021). As mineral dust is advected from the Sahara across the central eastern Atlantic Ocean, it alters radiation budgets, atmospheric stability, and moisture distribution (Ansmann et al., 2017; Marsham et al., 2008). This dual effect of dust—scattering and absorbing solar radiation while in the same time serving as cloud condensation nuclei (CCN)—leads to competing influences on the BL: radiative cooling can suppress turbulent mixing, yet CCN activation can lead to increased cloud cover and associated feedback on surface radiation. These processes have been observed to influence the vertical structure and stability of the ABL, but their overall impact on BL dynamics is still not fully understood.

Accurately representing ABL-aerosol interactions in climate and weather models is crucial because these processes affect surface conditions and large-scale atmospheric circulation and surface conditions (Menut et al., 2009; Pérez et al., 2006; Tombrou et al., 2007, 2015). Gaps in observational data over complex environments, such as the dust-laden, desert-ocean transition zone in the Atlantic, limit the ability of models to accurately capture BL evolution and aerosol influences (Rémy et al., 2019, 2021; Kallos et al., 2007). The need for observational data to validate and refine the atmospheric models is pressing, especially given the impacts on cloud formation, energy distribution, and surface-air interactions. Addressing these gaps through both ground-based experimental campaigns and satellite-based systems can significantly enhance understanding and modeling of BL processes in regions of critical climatic importance.

2.2.4 Meteorological Conditions and their impact on ABL Structure

The origin of the air mass interacting with the surface plays a pivotal role in shaping the ABL structure. The thermodynamic properties of the air mass, including its temperature, humidity, and stability, are largely determined by its source region and trajectory (Fuchs et al., 2017; Emeis, 2010). For instance, air masses originating over the ocean are typically moist and favor the formation of a shallow MABL. Conversely, continental air masses are often drier and more prone to thermal instability, potentially fostering deeper convective layers (Pal and Lee, 2019).

The wind patterns reflect the circulation of air masses in atmosphere and strongly influence ABL dynamics by modulating turbulence and horizontal and vertical mixing (Kang et al., 2007). Coastal regions, for example, frequently experience sea breeze circulation, which introduces cooler, moist air from the ocean. This can alter the temperature and humidity profiles near the surface and lead to the formation of a shallow, well-mixed layer. Strong winds can also enhance mechanical turbulence, which deepens the ABL and redistributes heat, momentum, and aerosols. The wind direction relative to topography can create additional complexities, such as forced uplift and localized variations in ABL height, as observed in regions with rugged terrain.

Humidity gradients within the ABL are closely linked to evaporation, condensation, and entrainment processes at the ABL top. High surface moisture content, such as that found over oceans or moist soil, can lead to a more humid and thermally stable boundary layer (Fan et al., 2008). On the other hand, dry air advection or subsidence from the free troposphere can destabilize the ABL by steepening the moisture gradient, influencing cloud formation, and reducing the clarity of the inversion layer.

Surface heating and cooling drive diurnal variations in ABL structure through convective mixing during the day and stratification at night (Stull, 1988). In convective conditions, strong surface heating destabilizes the atmosphere, leading to the formation of a high well-mixed ABL that can extend to significant heights. In contrast, nighttime cooling promotes the development of a stable boundary layer, where turbulence is suppressed, and temperature inversions become more pronounced. In coastal and marine environments, sea surface temperature variations also play a role, especially in moderating surface fluxes that govern ABL evolution.

Some events of interest are the sea breeze, the convection, and dust events. Sea breezes, driven by temperature contrasts between land and sea, introduce cool marine air inland. This leads to localized shifts in ABL height and structure, often producing a sharp gradient between the marine and terrestrial layers (Huang et al., 2009), or the formation of an Internal Boundary Layer (IBL) (Liu et al., 2001; Reddy et al., 2021). Convective events, driven by intense surface heating, destabilize the ABL and promote vigorous mixing leading to significant vertical development, cloud formation, and precipitation (Rao and Prasad, 2007). Moreover, dust aerosols, such as those transported from deserts, significantly impact ABL dynamics, as described in 2.2.3. One typical example is the area of the central tropical Atlantic ocean, where the general circulation is dominated by the Inter-Tropical Convergence Zone (ITCZ) and the Saharan Air Layer (SAL) (Dunion and Velden, 2004). The ITCZ, a belt of low pressure where the trade winds from the Northern and Southern Hemispheres converge, migrates seasonally between the northern and southern tropics. This movement influences rainfall and convective activity, creating conditions conducive to both the formation of clouds and the upward transport of aerosols over the Atlantic (Zhou et al., 2020). In tandem, the SAL—comprising hot, dry air laden with desert dust from the Sahara—moves westward across the Atlantic Ocean, especially in summer, driven by the prevailing trade winds (Prospero and Mayol-Bracero, 2013). These circulation patterns are key in transporting dust from Africa to the Atlantic, affecting the radiative balance and potentially impacting cloud formation, atmospheric stability, and therefore boundary layer behavior in the region (Sun and Zhao, 2020). Moreover, a typical characteristic of the eastern sides of the Atlantic, is that the air subsiding into the subtropical north-east Atlantic is warmer and drier than the air that has been in contact with the relatively cold ocean surface influenced by upwelling, and a strong inversion forms at the interface of the two air masses (Hanson, 1991).

2.3 Overview of ABL Measurement Techniques

The ABL can be studied using various observational techniques, ranging from in situ measurements to remote sensing methods. One common approach is to use aerosols as tracers of boundary layer processes, as their concentration and vertical distribution often reflect the structure and dynamics of the ABL. However, observing the ABL over marine regions is particularly complex due to limited ground-based observation sites, even though oceanic and coastal boundary layers exhibit unique characteristics. Given this constraint, satellite observations have become essential for studying lower troposphere characteristics over remote regions, offering a means to improve understanding of these complex systems. By analyzing certain key atmospheric variables that will be described in this section, we can infer the ABL height and its evolution under different conditions.

Data supporting aerosol research can be obtained either through episodically acquired data, localized in space and/or time (e.g., from field campaigns), or through routine monitoring efforts. The first available aerosol observations were provided by synoptic meteorological stations which measure either visibility reduction caused by dust or a code denoting dust weather (Klose et al., 2010). Modern sensors measure aerosols based on two broad categories: in situ and remote sensing. Remote sensing includes ground-based and space-based instruments, performing either passive or active measurements. Finally, radiosondes are among the most reliable measurement techniques for atmospheric profiling, though they have relatively low time resolution.

2.3.1 Ground-Based Active Remote Sensing

Lidars (LIght Detection And Ranging) are used to obtain information about distant objects using active optical systems based on the reflection and scattering of the light in the transparent or semi transparent media. The development and advancements in lidar techniques, have provided an unprecedented view of the vertical structure of the troposphere. The earliest investigations on dust vertical repartition were performed in the 1970s through limited aircraft measurements during field campaigns in the North Atlantic region (Prospero and Carlson, 1972). Having high vertical and temporal resolution, lidar can also detect the diurnal evolution of ABL. Detailed altitude knowledge of all the layers is helpful for assessing the radiative impact and for tracing particles back to their origins. Moreover, using sophisticated multi-wavelength systems that have separate channels for elastic backscatter, Raman backscatter, and depolarization, lidars provide a comprehensive optical and microphysical characterization of aerosols. The advanced lidar systems can characterize aerosol optical and microphysical properties, with fewer and less stringent assumptions from other remote sensing methods. This way, the capability of distinguish desert dust from marine aerosol is valuable for the interpretation of ABL findings. Finally, lidar systems can acquire measurements continuously during day and night in a wide range of weather conditions (e.g. Pappalardo et al., 2014).

Lidar systems have proven valuable for continuous profiling of aerosol and atmospheric structures, as their high vertical resolution enables detailed monitoring of ABL height (Wiegner et al., 2006). However, studying the ABL by means of Lidars, can suffer from many restrictions related to weather conditions, temporal and spatial resolution, range and accuracy. The retrieval of the ABL top based on Lidar systems in a region with particular topography, such as Finokalia (chapter 4), can hardly be an automated procedure, because of the variability inserted by aerosols and clouds existence, as well as by strong wind fields.

Aerosol PollyXT Raman Lidar

A lidar system, is an advanced active remote sensing instrument designed to measure atmospheric profiles of aerosols and water vapor. Operating on the principle of elastic and inelastic scattering of light by atmospheric particles, it uses a laser source to emit pulses of light at specific wavelengths. The system detects the returned signal, separating elastic (Rayleigh and Mie) and inelastic (Raman) components to provide detailed vertical profiles. The fundamental equation governing lidar backscatter is the lidar equation:

$$P(r) = \frac{C}{r^2}\,\beta(r)\exp\left(-2\int_0^r \alpha(r')\,dr'\right) \quad (2.1)$$

where:

- P(r) is the received power from a range r

- C is the system constant
- $\beta(r)$ is the backscatter coefficient
- $\alpha(r)$ is the extinction coefficient

These parameters briefly characterize the interaction of light with aerosols and molecules.

A lidar provides key products such as backscatter and extinction coefficients, aerosol optical depth (AOD), water vapor mixing ratio, and depolarization ratios. These products enable the study of aerosol properties, atmospheric stability, and moisture distribution. In this dissertation, the products of backscatter coefficient (1064 nm, 532 nm) and water vapor mixing ratio will be interpreted in order to acquire information for the ABL dynamics. The backscatter coefficient $\beta(r)$ stands for the ability of the atmosphere to scatter light back into the direction from which it comes (Weitkamp et al., 2005). It is the primary atmospheric parameter that determines the strength of the lidar signal, describing how much light is scattered into the backward direction, i.e., towards the lidar receiver (scattering angle θ = 180°). In the atmosphere, the laser light is scattered by air molecules and particulate matter, i.e., $\beta(r, \lambda)$ can be written as

$$\beta(r, \lambda) = \beta_{mol}(r, \lambda) + \beta_{aer}(r, \lambda). \tag{2.2}$$

Molecular scattering (index 'mol'), mainly occurring from nitrogen and oxygen molecules, primarily depends on air density and thus decreases with height, i.e., backscattering decreases with distance if the observation is made from the ground, but increases in the case of downward-looking systems on aircraft or spacecraft. Particulate scattering (index 'aer' for aerosol particles) is highly variable in the atmosphere on all spatial and temporal scales. Particles represent a great variety of scatterers: tiny liquid and solid air-pollution particles consisting of, e.g., sulfates, soot and organic compounds, larger mineral-dust and sea-salt particles, pollen and other biogenic material, as well as comparably large hydrometeors such as cloud and rain droplets, ice crystals, hail, and graupel. The boundary layer contains higher concentrations of molecules and aerosols compared to the free troposphere. This difference makes the lidar backscattering coefficient an important parameter for identifying the boundary layer top. By analyzing the abrupt changes in backscatter profiles, the transition zone between the well-mixed boundary layer and the relatively cleaner, less turbulent free troposphere can be detected.

Another crucial parameter for interpreting the lidar measurements, is the transmittance T(r), that is defined as the fraction of light that gets lost on the way from the lidar to the scattering volume and back. T(r) can take values between 0 and 1 and is given by

$$T(r, \lambda) = \exp\left(-2\int_0^r \alpha(r', \lambda)\, dr'\right) \tag{2.3}$$

This term results from the specific form of the Lambert–Beer–Bouguer law for lidar. The integral considers the path from the lidar to distance r. The factor 2 stands for the two-way transmission path. The sum of all transmission losses is called light extinction, and $\alpha(r, \lambda)$ is the extinction coefficient. It is defined in a similar way as the backscatter coefficient as the product of number concentration and extinction cross section $\sigma_{j,ext}$ for each type of scatterer j,

$$\alpha(r,\lambda) = \sum_j N_j(r)\sigma_{j,ext}(\lambda) \tag{2.4}$$

Extinction can occur because of scattering and absorption of light by molecules and particles. The extinction coefficient therefore can be written as the sum of four components,

$$\alpha(r,\lambda) = \alpha_{mol,sca}(r,\lambda) + \alpha_{mol,abs}(r,\lambda) + \alpha_{aer,sca}(r,\lambda) + \alpha_{aer,abs}(r,\lambda) \tag{2.5}$$

where the indices 'sca' and 'abs' stand for scattering and absorption, respectively. Because scattering into all directions contributes to light extinction, the (integral) scattering cross section σ_{sca}, together with the absorption cross section σ_{abs}, both in m^2, make up the extinction cross section $\sigma_{ext}(\lambda) = \sigma_{sca}(\lambda) + \sigma_{abs}(\lambda)$.

The Volume Linear Depolarization Ratio (VLDR), also known as δ, is a key parameter that provides information about the shape of atmospheric particles. It is defined as the ratio of the cross-polarized to co-polarized backscatter coefficients and is given by the equation:

$$\delta(r,\lambda) = \frac{\beta_{\perp}(r,\lambda)}{\beta_{\parallel}(r,\lambda)} \tag{2.6}$$

where $\beta_{\perp}$ and $\beta_{\parallel}$ are the backscatter coefficients for the perpendicular and parallel polarization channels, respectively. High depolarization values indicate the presence of non-spherical particles such as dust or ice crystals, while low values are associated with spherical targets like marine particles or water droplets.

For this dissertation, PollyXT Raman lidar data are used to investigate the aerosol type and load of the atmosphere and to derive the top of the atmospheric boundary layer. This multi-wavelength depolarization, Raman PollyXT Lidar of the National Observatory of Athens (NOA), was built in 2014 and operated in Athens (2015-2016), Nicosia (for 2 campaigns in March 2015 and April 2016), Finokalia (2017-2018) and Antikythera (2018-today). The system components are briefly depicted in Table 2.1, but a more detailed description can be found at Engelmann et al. (2016). PollyXT Lidar consists of a compact, pulsed Nd:YAG laser, emitting at 355, 532 and 1064nm at 20Hz repetition rate, with the laser beam pointed into the atmosphere at an off-zenith angle of 5°. The backscattered signal is collected by a Newtonian telescope with 0.9m focal length, acquiring profiles with vertical resolution 7.5 m, and the temporal resolution 30s. The system includes five elastic channels for far and near range detection at 355, 532 and 1064 nm; four Raman channels for far and near range detection at 387 and 607 nm; two depolarization channels at 355 nm and 532 nm; and a water vapor channel at 407 nm. The overlap-affected height range of the overall system is 120 m above the lidar for the Near Field channels and between 700 and 800 m height for the Far Field channels. All measurements within the period 2014–2022 are available online at this Link.

In practice, the attenuated backscatter coefficient is what the PollyXT lidar system initially provides, representing the combined effects of scattering and attenuation in the atmosphere. It is more useful to use the attenuated backscatter coefficient for visualizing atmospheric features, as in Fig. 2.3. The yellow to red regions in the plot indicate

Table 2.1: Specifications of PollyXT Raman Lidar

PollyXT Lidar Specifications	
Operating Wavelengths	1064 nm, 532 nm, 355 nm
Number of Channels	12
Height Resolution	7.5 m
Time Resolution	30 sec
Maximum Altitude	40 km
Pre-Trigger	256 bins
Repetition Rate of laser	20 Hz
Photomultiplier voltage	127 Volts
Zenith angle of measurement	5°
Polarization	Cross and Total

an aerosol layer passing above the instrument, with higher concentrations or scattering properties. The black areas above 2500 m represent regions where no meaningful information can be retrieved because the lidar signal has been significantly attenuated, leaving insufficient return signal for analysis. In the context of boundary layer study, the Wavelet Covariance Transform Method is used to detect abrupt changes in the backscatter coefficient, and consequently determine the boundary layer top, as detailed in Chapter 3.

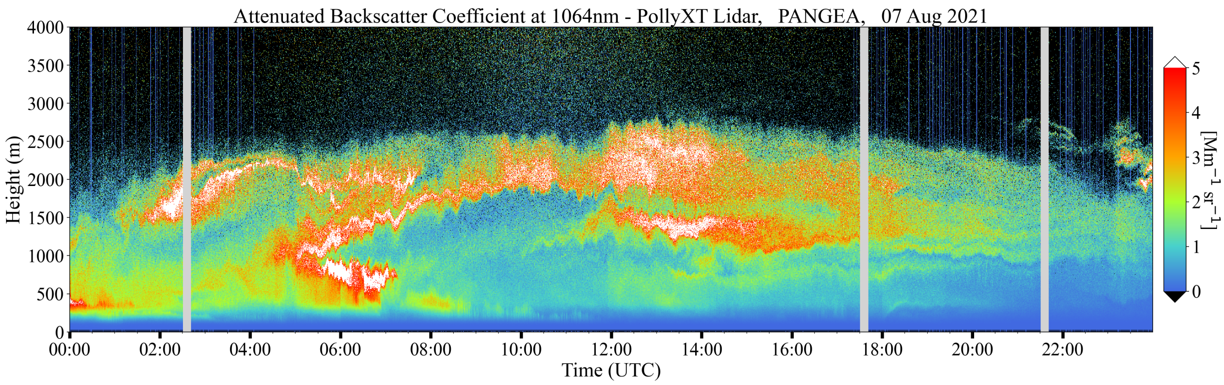

Figure 2.3: 24-hour Attenuated backscatter coefficient (β_{att}) from the 1064nm channel of PollyXT Lidar in PANGEA Observatory, 07 August 2021. Y-axis represents the height above the instrument, X-axis is the time of measurement and the colorbar accounts for β_{att} measured in $M\mu^{-1}sr^{-1}$.

The attenuated backscatter coefficient $\beta_{att}(r,\lambda)$, is essentially the backscatter coefficient $\beta(r,\lambda)$ (eq. 2.2), scaled by the transmission of the atmosphere (eq. 2.3), accounting for the fact that the laser light emitted by the lidar is attenuated as it travels through the atmosphere, and the returning signal is further attenuated on its way back to the detector. The attenuated backscatter coefficient incorporates the two-way transmittance through the exponential term and can be expressed as: $\beta_{att}(z) = \beta(z) \cdot exp(-2\int_0^z \alpha(r')\,dr')$.

When interpreting atmospheric lidar measurements for ABL investigation, it is essential to analyze the attenuated backscatter coefficient (Att BSC) in combination with the volume linear depolarization ratio (VLDR). The Att BSC provides information on the intensity of the lidar signal, which is influenced by the concentration and size of atmospheric particles. The VLDR complements this by providing information on particle shape, as it distinguishes between spherical particles, such as liquid droplets, and non-spherical particles, such as dust or ice crystals.

In the figure 2.4, the Att BSC (left panel) highlights regions of high backscatter intensity, which can indicate aerosol or cloud layers. The corresponding VLDR (right panel) reveals the nature of these layers, helping to identify whether they are composed of spherical or non-spherical particles. The white points in the attenuated backscatter indicate the presence of clouds and are not included in the ABL analysis. Between 1 and 5 km altitude, the VLDR exhibits greenish tones (∼20%), suggesting the presence of non-spherical aerosol particles, likely a mixture of dust. Closer to the surface (below 1 km) the VLDR values remain below 10%, indicating a predominance of more spherical particles, such as marine aerosols or pollution. This combined view of backscatter intensity and depolarization ratio allows for a more detailed characterization of atmospheric aerosol layers.

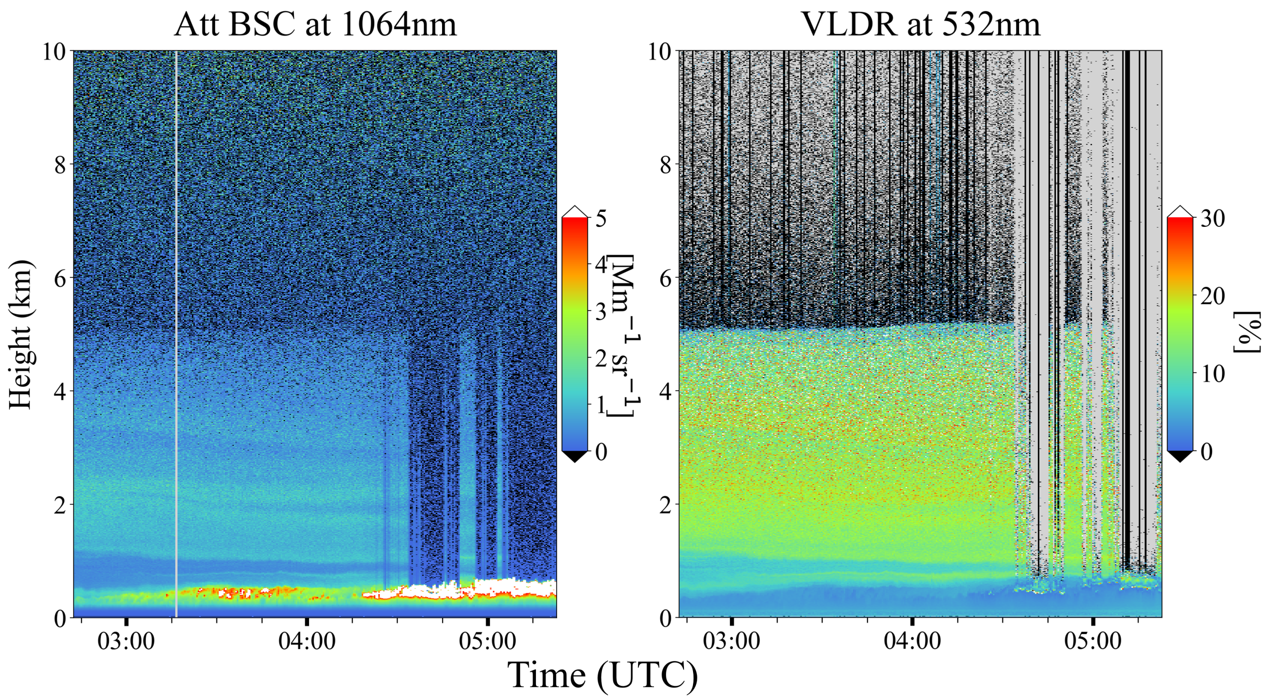

Figure 2.4: Ground-based PollyXT Lidar at Mindelo (16.87°N, 24.99°W), Cabo Verde, on the 10th of September, 2021, depicting the attenuated backscatter coefficient (Att Bsc) at 1064 nm (left), and volume linear depolarization ratio (VLDR) at 532 nm (right).

Halo Wind Doppler Lidar

The Wind Doppler lidar system is an active remote sensing instrument designed to measure wind velocity profiles by utilizing the Doppler shift of backscattered infrared laser light, which relates the change in frequency (Δf of the scattered light to the radial velocity (U_r) of atmospheric scatterers (aerosols or particulates). The relationship is given by:

$$U_r = \frac{\Delta f \cdot c}{2 \cdot f_0} \tag{2.7}$$

where:

- U_r: Radial velocity of the scatterer (m/s)
- Δf: Doppler frequency shift (Hz)
- C: Speed of light ($\approx 3 \cdot 10^8$ m/s)
- f_0: Emitted laser frequency (Hz)

This technology (Newsom and Krishnamurthy, 2022) provides high spatial and temporal resolution, ideal for atmospheric applications such as wind and turbulence characterization. The Wind Doppler lidar typically operates using an infrared laser with a wavelength of 1.5 μm , which is optimal for eye safety and atmospheric aerosol scattering. This wavelength is commonly used in Doppler lidars for measuring wind velocity profiles because it balances atmospheric transmission and backscatter sensitivity (Pearson et al., 2009).

The Wind lidar transmits pulses of infrared light into the atmosphere. The scattered light, returned by aerosols and particles in the air, is collected by the system. The frequency shift between the transmitted and received light provides information about the radial velocity of atmospheric scatterers. The system uses a reference laser (local oscillator) to mix with the received signal, enabling precise Doppler shift measurement. Finally, it provides radial velocity, attenuated backscatter, and SNR, often with full hemispheric scanning for three-dimensional wind mapping.

The Halo Photonics Stream Line Scanning Doppler lidar data are used for this dissertation. It is a 1.5 µm pulsed Doppler lidar with a heterodyne detector that can switch between co- and cross-polar channels (Pearson et al., 2009). The Halo lidar has a range resolution of 30 m and measures the attenuated aerosol backscatter and Doppler velocity along the beam direction. During the PreTECT Campaign (see section 4), two conical scans at 15° and 75° elevation angle and a 3° elevation angle sector scan were scheduled every 15 minutes. This schedule leaves approx. 9 minutes out of every 15 minutes for vertically-pointing measurement. For the vertically-pointing measurements integration time was set to 3.7 seconds. For the 15° conical scan integration time was 4.5 seconds and for the 75° conical scan integration time was 6.5 seconds. More details about Halo Doppler Lidar characteristics and specifications can be found at Pearson et al. (2009) and Manninen et al. (2016). The technical specifications of the instrument as configured for standard operation during the campaign are summarized in Table 2.2.

An example of the Halo Wind Doppler Lidar measurements that were conducted during the PreTECT Campaign in Finokalia, Crete, is shown in Figure 2.5. Halo Lidar provides the backscatter coefficient, as well as other critical atmospheric parameters, including wind speed, wind direction, and the turbulent kinetic energy dissipation rate. The backscatter coefficient is used in detecting the boundary layer top, as explained above (subsection 2.3.1). The measurements of Halo lidar measurements are significant in this study, as wind components and turbulence shape the processes that influence the behavior and dynamics of the boundary layer.

Table 2.2: Specifications of Halo Wind Lidar

Halo Wind Doppler Lidar Specifications	
Wavelength	1.5μm
Detector	heterodyne
Pulse repetition frequency	15 kHz
Nyquist velocity	20 ms^{-1}
Sampling frequency	50 MHz
Velocity resolution	0.038 ms^{-1}
Height resolution	30m
Range	90-9600m
Pulse duration of measurement	0.2 μs

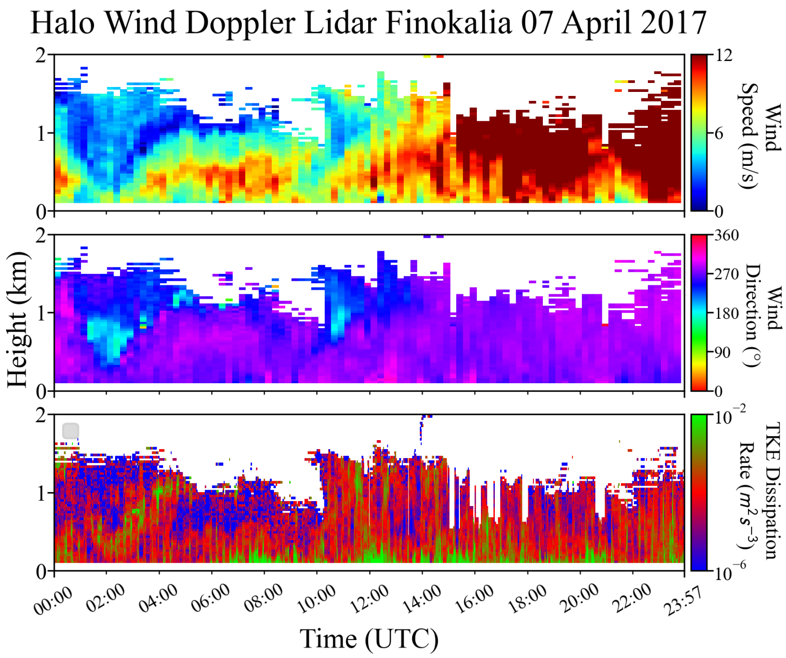

Figure 2.5: 24-hour Measurements of Halo Wind Doppler Lidar in Finokalia, 07 April 2017. Y-axes represent the height above the instrument, X-axis is the time of measurement and the colorbar accounts for wind speed in m/s (top), wind direction in degrees (middle) and turbulent kinetic energy dissipation rate in m^2s^{-3} (bottom).

During the ASKOS Campaign (see section 5) Horizontal wind profiles were retrieved from a velocity azimuth display (VAD) scan with 12 azimuthal angles at 60° elevation angle every 15 minutes. Otherwise, the Doppler lidar operated in vertical stare mode, retrieving vertical wind profile time series. The Doppler lidar data was post-processed according to Vakkari et al. (2019) and a signal-to-noise ratio (SNR) threshold of 0.005 was applied to the vertically-pointing measurements. Turbulent kinetic energy (TKE) dissipation rate profiles were calculated from the vertically-pointing data using the method by O'Connor et al. (2010). Instrumental noise was calculated from signal-to-noise ratio according to Pearson et al. (2009) and subtracted from the vertical wind variance time series before the TKE dissipation rate calculation. To estimate mixed layer height (MLH) from the TKE dissipation rate profiles a threshold of $10^{-4} m^2 s^{-3}$ was applied, similar to previous studies (e.g. Vakkari et al., 2015).

2.3.2 Satellite-Based Remote Sensing

Field campaigns and long-term monitoring stations and networks provide detailed measurements of specific dust events for limited periods or time-series and these measurements are essential for dust research. However, ground-based and airborne observations do not provide enough observational constraints for a comprehensive quantification of dust loads, associated impacts and understanding of atmospheric processes on a global scale (Knippertz and Todd, 2012). One additional tool that has become increasingly important in recent years for identifying, tracking and analyzing large-scale dust events is remote sensing from space. Indeed, the satellite repetitive global coverage is the only way to monitor the complex spatial pattern (horizontally and vertically) and the high temporal variability of mineral dust (Knippertz and Stuut, 2014).

There are currently more than twenty satellite sensors available for aerosol studies (Lenoble et al., 2013) allowing to spatially extend the point observations from the ground sites. These sensors have been widely used for dust research because they allow repetitive large-scale observations and monitoring of dust events. Examples of enhanced passive sensors include among others MODIS, the Multi-angle Imaging Spectro-Radiometer and Polarization and Directionality of the Earth's Reflectance. Satellites equipped with radiometers mainly provide the AOD (i.e. the total amount of aerosol weighted by their extinction coefficient) at one or several wavelengths, including the contribution of all aerosol species. Some algorithms allow the retrieval of the dust contribution to AOD (i.e. dust optical depth, DOD). The UV and IR spectral ranges that have been used besides the Visible allow to extent the monitoring to arid and semi-arid surfaces, which is of primary importance for a better understanding of desert dust emissions (Legrand et al., 2001; Prospero et al., 2002; Knippertz and Stuut, 2014).

Observations from the geostationary sensors Meteosat and MSG have been applied for studies of North African dust emissions and transport over surrounding oceanic regions. Although they are restricted to only one part of the globe the frequency of measurements (15 min with MSG) is of great benefit for dust research (Thieuleux et al., 2005; Schepanski et al., 2007). Most of the sensors on polar-orbiting platforms are limited to one observation over a certain area per day, a frequency which may, at least in certain cases, prevent a representative measurement of daily dust content (Kocha et al., 2013).

Since the launch of the Cloud-Aerosol Lidar with Orthogonal Polarization onboard Cloud-Aerosol Lidar and Infrared Pathfinder Satellite Observations (CALIOP/CALIPSO) mission in 2006 (Winker et al., 2010), the first satellite carrying a lidar specifically designed to study aerosols and clouds (Winker et al., 2009), vertically resolved observations of dust have become available at a glob-al scale, which was a huge progress in dust observations. Thanks to the CALIOP lidar depolarization measurements, CALIPSO enables aerosol classification, including identification of non-spherical particles such as dust (Omar et al., 2009). CALIPSO has acquired the largest amount of global dust vertical profiles so far (Figure 2.6). Based on CALIOP measurements, a number of dust studies have been performed recently mainly focusing on the characterization of North African dust transport over the Atlantic (Liu et al., 2008; Ben-Ami et al., 2009; Generoso et al., 2008) and on the analysis of the 3D structure of Asian dust (Huang et al., 2009; Uno et al., 2008). Moreover, many climatological studies have monitored the dust load and investigated the impact on dynamics (Berhane et al., 2024; Senghor et al., 2017). The CALIPSO mission offers considerable improvement in determining the vertical distribution of dust properties globally, especially in situations where passive sensors cannot, such as over snow and at cloudy skies (Winker et al., 2009). Moreover, the information about the vertical layering of aerosols provided by lidar instruments is crucial for aerosol-cloud interaction studies.

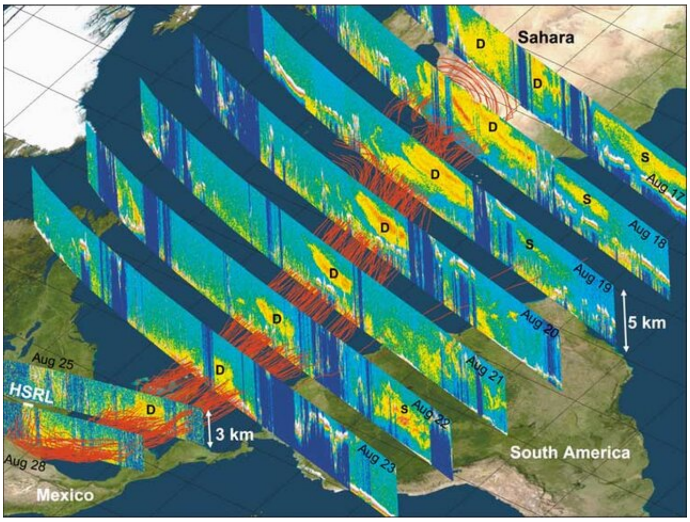

Figure 2.6: An example demonstrating the capability of CALIOP to track dust long-range transport during a dust event that originated in the Sahara Desert on 17 August 2007 and transported to the Gulf of Mexico. Vertical images are 532-nm attenuated backscatter coefficients measured by CALIOP when passing over the dust transport track, source: Liu et al. (2008)

Advanced aerosol characterization knowledge provided by ground-based observational networks (e.g. AERONET and EARLINET) are of primary importance in order to discriminate dust from space and eventually validate and interpret the satellite-derived dust products to-wards quantifying their climatic footprint and contribution on the air quality.

Towards investigating the dynamics of the BL over the Atlantic Ocean region, earth observations (EO) provided by CALIOP (Hunt et al., 2009), the primary instrument on board the joint National Aeronautics and Space Administration (NASA) and Centre National D'Études Spatiales (CNES) CALIPSO mission, are extensively implemented. More specifically, CALIOP provided as integrated component of the Afternoon-Train constellation of polar-orbit sun-synchronous satellites (Stephens et al., 2018), profiles of aerosols and clouds along the CALIPSO orbit-path between June 2006 and August 2023. In the framework of this dissertation, CALIOP Level 2 (L2) Version 4 (V4) aerosol profiles of backscatter coefficient at 532 nm and particulate depolarization ratio at 532 nm are used, provided at uniform 5 km horizontal resolution and 60 m vertical resolution for the altitudinal range between -0.5 and 20.2 km above mean sea level (a.m.s.l.) are used, for the domain encompassing the broader North Atlantic Ocean- Western Saharan Desert and for September 2021. Prior implementation of CALIOP optical products, rigorous quality assurance procedures are applied (Marinou et al., 2017; Proestakis et al., 2024), following also the quality controls adopted towards the generalization of the official CALIPSO Level 3 (L3) products (Winker et al., 2013; Tackett et al., 2018). Towards this objective, the most aggressive quality control procedure applied in the framework of the study is the cloud-free condition, removing the entire L2 profiles when detected atmospheric layers (Vaughan et al., 2009) along the CALIPSO orbit-path are classified as clouds in the feature-type classification algorithm (Liu et al., 2009; Zeng et al., 2019). Figure 2.7 provides an indicative example of the considered CALIOP observations and products, and more specifically the Feature Type (Fig.2.7 top left) product and the profiles of particulate depolarization ratio at 532 nm (Fig.2.7 top right), total backscatter coefficient at 532 nm (Fig.2.7 bottom left), and quality-assured total backscatter coefficient at 532 nm (Fig.2.7 bottom right), along the CALIPSO overpass on the 10^{th} of September 2021.

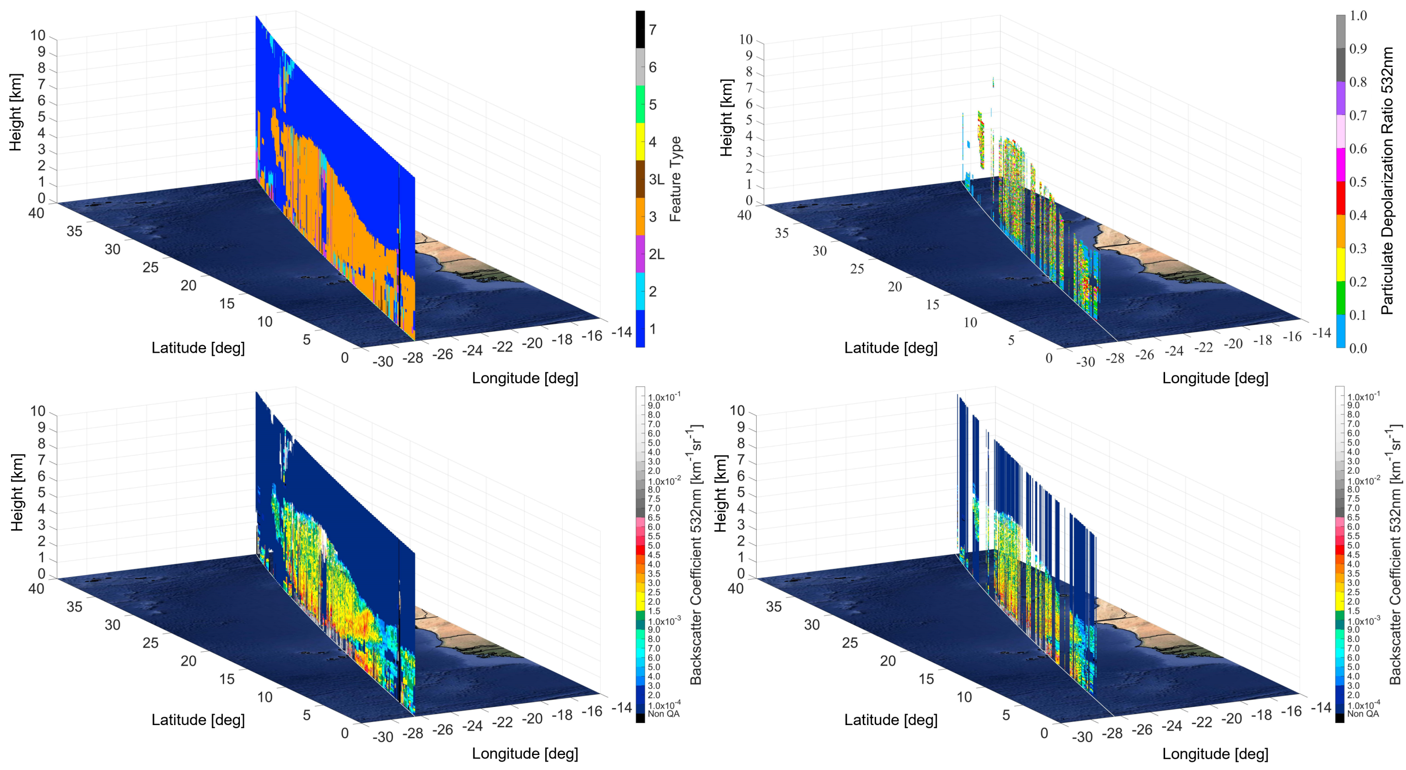

Figure 2.7: CALIPSO nighttime overpass in the ESA-ASKOS campaign region of interest in the proximity of Cabo Verde on the 10^{th} of September, 2021, depicting the Feature Type (top left), particulate depolarization ratio at 532 nm (top right), total backscatter coefficient at 532 nm (bottom left), and the quality-assured total backscatter coefficient at 532 nm (bottom right).

2.3.3 Radiosondes

Radiosondes are a widely used atmospheric in-situ measurement tool consisting of a weather balloon and a sensor package that records temperature, humidity, and wind as it ascends through the atmosphere. As the balloon rises, the sensor transmits data back to the ground station, providing high-resolution vertical profiles of these atmospheric variables(Durre et al., 2006). The main advantage of radiosondes lies in their high vertical resolution, enabling detailed measurements of atmospheric properties at different altitudes, which is essential for understanding atmospheric boundary layer dynamics and upper atmospheric conditions. However, their spatial resolution is limited since they only provide data at specific points along the balloon's trajectory and are typically launched at fixed locations few times per day.

Despite these limitations, radiosondes are considered accurate tools for atmospheric observations, with consistent measurements across a range of altitudes. They are particularly useful in combination with other remote sensing instruments like lidars, as they provide complementary information on the vertical profile of the atmosphere.

Figure 2.8 presents an example of a radiosonde measurement. The left panel shows a radiosonde balloon ascending through the atmosphere. It is carrying sensors to measure meteorological parameters, along with a red parachute that will facilitate the landing of the sensors after the balloon bursts. The right panel shows sample profiles of relative humidity (RH), temperature, and wind speed recorded by the radiosonde as it ascends.

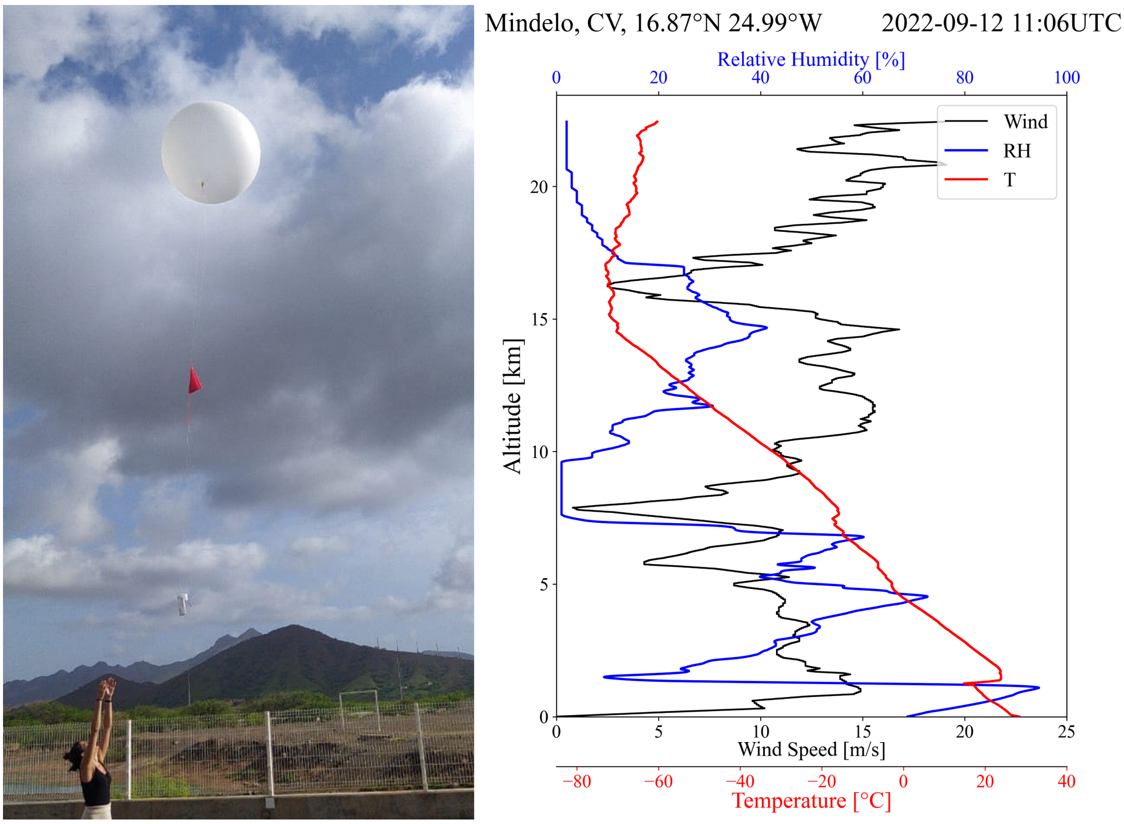

Figure 2.8: Left: Release of a radiosonde during ASKOS Campaign at Mindelo of Cabo Verde on the 12^{th} September 2022, Right: Profiles of temperature (red line), Relative Humidity (RH, blue line) and Wind Speed (black line) as recorded by the radiosonde.

As mentioned before, radiosondes have limitations, including low temporal resolution due to typically sparse launch intervals and spatial inaccuracies caused by the horizontal drift of the balloons as they ascend (Seidel et al., 2011). Such variability in drift paths complicates the accurate localization of ABL features.

Figure 2.9 presents the ascending trajectories of two radiosondes launched from the same point on different days, illustrating the influence of atmospheric circulation on their paths. In the first map (left panel), the radiosonde follows a westward trajectory, while in the second map (right panel), the balloon initially moves west but then twists and reverses course, heading east. These contrasting trajectories highlight the inherent variability of atmospheric circulation and the challenges associated with radiosonde measurements. To address these challenges, remote sensing techniques such as lidar offer a complementary approach, providing high-resolution, continuous observations that are independent of atmospheric circulation variability.

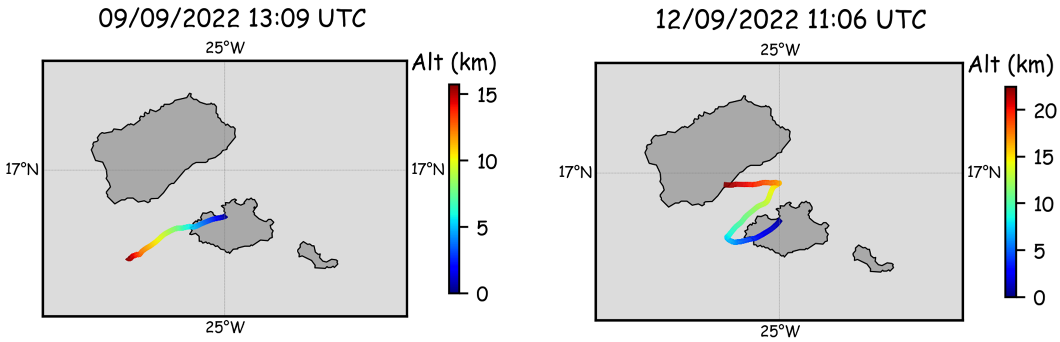

Figure 2.9: Ascending trajectories of two radiosondes as a function of height. The ballons were launched at the Mindelo site in Cabo Verde (16.87°N, 24.99°W) on two different days. Left panel: 9^{th} September 2022 southwestward trajectory, Right panel: 12^{th} September 2022 twisting trajectory.

2.3.4 Models

ERA-5 is a global atmospheric reanalysis that was developed by the Copernicus Climate Change Service (C3S) and produced at the European Centre for Medium-Range Weather Forecasts (ECMWF). It is a comprehensive, high-resolution global climate data set offering hourly atmospheric variables spanning from 1950 to the present, with a horizontal resolution of 31 km, with 137 vertical levels (Vogelezang and Holtslag, 1996) ranging from the surface up to 0.01 hPa. The ABL height in ERA5 is derived from the model's vertical velocity and potential temperature profile, using a combination of turbulence and stability criteria to define the ABL top, according to ECMWF (2017), Chapter 3. This reanalysis product is highly valuable for studies of atmospheric dynamics, including boundary layer processes, providing a consistent and globally available source of data that complements observational measurements. For more details on ERA5's methodology, the reader can refer to the ECMWF's documentation (Rémy et al., 2019; Hersbach et al., 2020) and the official ERA5 user guide. von Engeln and Teixeira (2013) performs a Planetary Boundary Layer Height Climatology by using the ECMWF Reanalysis Data.

The boundary layer height plays a critical role in applications such as air quality modeling and atmospheric dispersion studies. Thus, it is provided as a diagnostic variable in ERA5. The parametrization of the mixed layer uses a boundary layer height from an entraining parcel model. But in order to get a continuous field, also in neutral and stable situations, a bulk Richardson method is used as a diagnostic, independent of the turbulence parametrization. This method follows the conclusions of the recent study by Seidel et al. (2012). They evaluated a large number of methods proposed in the literature for estimating the boundary layer height and found that an algorithm based on the bulk Richardson number, originally proposed by Vogelezang and Holtslag (1996), is the most appropriate for application to radiosondes, reanalysis and climate model data sets. Several approximations are applied to the original algorithm, so that it can be consistently applied for both radiosondes and model output. Thus, since the friction velocity is not known from radiosonde data, the surface frictional effects are ignored in the computation of the bulk shear.

Similarly, because radiosonde observations do not include winds close to the surface (at 2m), winds at 2m are set to zero. With these assumptions, the boundary layer height h_{BL} is defined as the lowest level at which the bulk Ri reaches the critical value of 0.25. Seidel et al. (2012) showed that this algorithm is suitable for both convective and stable boundary layers, identifies a nonnegative height in all cases, and is not strongly dependent on the sounding vertical resolution.

The bulk Richardson number is computed as follows.

$$
\begin{aligned}
|\Delta U|^2 &= u_{\mathrm{hbl}}^2 + v_{\mathrm{hbl}}^2 \\
s_{vn} &= c_p T_n(1+\epsilon q_n) + g z_n \\
s_{\mathrm{vhbl}} &= c_p T_{\mathrm{hbl}}(1+\epsilon q_{\mathrm{hbl}}) + g h_{\mathrm{bl}} \\
Ri_b &= \frac{2g(s_{\mathrm{vhbl}} - s_{vn})h_{\mathrm{bl}}}{(s_{\mathrm{vhbl}} + s_{vn} - g h_{\mathrm{bl}} - g z_n)|\Delta U|^2}
\end{aligned}
\tag{2.8}
$$

where index n indicates the lowest model level and h_{BL} indicates the boundary layer height, i.e the level where Rib = 0.25. The virtual dry static energy from the lowest level s_{vn} is compared to the virtual dry static energy at the boundary layer height h_{bn}. For the buoyancy parameter g/T, T is computed from s and averaged between the lowest model level and the boundary layer height. The boundary layer height is found by a vertical scan from the surface upwards. If the boundary layer height is found to be between two levels a linear interpolation is done to find the exact position.

In this dissertation, the measurements-derived ABL height is compared to values obtained from the ERA5 Reanalysis dataset. The results are presented in Chapters 4 & 5. An example of the data used, is presented in figure 2.10. The depicted domain covers the Atlantic ocean surface that extends from the eastern America to the western Africa around the ITCZ. This is one of the studied areas of Chapter 5. The ABL top can range from 200 m to 1500 m. The higher values are met above the African continent, while the ABL height in the Atlantic ocean strongly depends on the circulation and the cyclonic activity (Ren et al., 2019).

Additionally, Hybrid Single-Particle Lagrangian Integrated Trajectory (HYSPLIT) is employed to analyse the backward trajectories of air masses arriving at the site of the ASKOS Campaign, Mindelo, Cabo Verde. This model estimates the tracking of air parcels over time, providing valuable information about the origins of the air parcels and their potential interactions with dust and other atmospheric constituents (Rolph et al., 2017). By identifying these pathways, a clearer understanding of the sources and transport mechanisms of the the atmospheric conditions at Cabo Verde can be established.

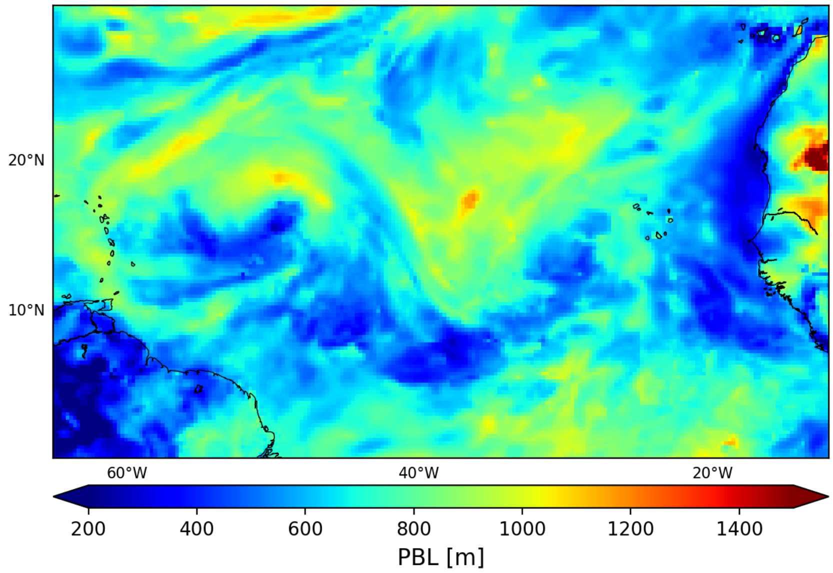

Figure 2.10: Planetary Boundary Layer (PBL) Height from ERA 5 - ECMWF dataset for the 14^{th} of September 2022, over the region of western Africa and eastern Atlantic Ocean.

Chapter 3

Methods for Acquiring the ABL Height

3.1 Introduction to methods

The study of Atmospheric Boundary Layer (ABL) dynamics in coastal areas presents unique challenges due to the complex interactions between land, sea, and atmosphere. A combination of advanced methods is necessary for investigating these dynamics. This chapter outlines the various methodologies employed in this study, each chosen for its ability to capture different aspects of the ABL. More specifically, five key methods are described and applied: (i) the Wavelet Covariance Transform (WCT) method (Brooks, 2003), (ii) the Gradient Method(Palm et al., 1998), (iii) the Threshold Method (Vakkari et al., 2015), (iv) the Richardson Method (Fedorovich et al., 2004)and (v) the Parcel Method (Thorpe et al., 1989). Each method will be analyzed separately, focusing on its theoretical foundations, the specific way it was implemented in this study, and its relevance to understanding ABL dynamics in coastal environments.

The detection of the ABL top is a critical feature to understand boundary layer physics, and can be pretty challenging. In the WCT method, for instance, different peaks may appear, requiring careful assessment to determine which one corresponds to the ABL top. Misidentification could lead to incorrect interpretations of the boundary layer structure and thus, to wrong conclusions for the dynamics. Similarly, when using the Gradient method, strong temperature or humidity inversions may not always correspond to the ABL top, especially in cases where cumulus clouds or other atmospheric features distort the signal. These complications also highlight the difficulty of automating the process for detection of the ABL top, particularly in coastal areas where additional factors such as complex topography (e.g., nearby mountains) or high aerosol loads (e.g., dust in the lower troposphere) can further obscure the boundary layer.

Given these complexities, the methods employed must be adapted to address the environmental factors present in coastal regions. Each method is suited to uncovering different aspects of the ABL, and their combination may provide a more complete image of the ABL behavior. Following the detailed descriptions, a comparative analysis is conducted to evaluate the strengths and weaknesses of each one. This comparison will point out the specific conditions under which each method performs best, as well as any limitations encountered. By integrating the results, it is possible to construct a more comprehensive understanding of the ABL in coastal regions, offering new tools to investigate the atmospheric processes in these complex environments.

It is important to note that this chapter is critical to the overall study, as it contains all the technical information necessary to understand the methodologies applied. Given the complexity involved in the ABL physics, particularly in coastal areas, the study contains a significant amount of technical detail. The precision and depth of these methods are crucial for the accurate interpretation of the data collected and the assessment of different possible scenarios for identifying the ABL top.

3.2 Wavelet Covariance Transform Method (WCT)

The Wavelet Covariance Transform (WCT) is one of the most widely used techniques for detecting atmospheric layers (aerosol layers, ABL). It has the ability to capture both spatial and temporal variability across multiple scales and has been employed extensively in the literature for identifying the ABL top. Numerous studies have demonstrated the effectiveness of WCT method in a variety of environments (Brooks, 2003; Baars et al., 2008; Nakoudi et al., 2019; Dang et al., 2019; Zhong et al., 2020; Kim et al., 2021; Granados-Muñoz et al., 2012; Whitcher et al., 2000; Davis et al., 2000), including coastal areas where the complexity of the boundary layer can be particularly challenging to resolve. In this section, the theoretical foundation of the WCT method will be described, followed by specific applications in this study, highlighting both strengths and limitations.

3.2.1 General Description

WCT method is based on wavelet analysis, which decomposes a signal into both time and frequency components. This is particularly effective for identifying abrupt changes, such as layer boundaries, in atmospheric profiles.

The mathematical expression for the core equation for the continuous wavelet transform (CWT, Subbey et al. (2008)) is:

$$W_{\psi}(f, a) = \frac{1}{\sqrt{a}} \int_{-\infty}^{+\infty} f(t)\, \psi^{*} \left(\frac{t-b}{a} \right) dt \tag{3.1}$$

• f(t) is the original signal (the atmospheric profile, e.g., temperature, humidity or aerosol backscatter as a function of height).

• ψ is the ”mother wavelet” function. The asterisk $*$ denotes the complex conjugate.

• a is the scale parameter, which stretches or compresses the wavelet.

• b is the translation parameter (location).

Wavelets come with a variety of ”mother functions” each with its own properties and applications. Selecting a Wavelet function depends on the application, as they have different properties and strengths (Graps, 1995). The most common are the Marr wavelet, the Morlet wavelet and the Haar wavelet.

Marr wavelet

The or Marr wavelet, also known as Mexican Hat wavelet (Morille et al., 2007), is commonly used in atmospheric applications for boundary detection because of its sensitivity to changes in the second derivative of the signal. It is used for detecting edges and features with smooth transitions. The Mexican Hat wavelet is the second derivative of the Gaussian function, and its form is:

$$\psi(t) = (1 - t^2)e^{-t^2/2} \tag{3.2}$$

The wavelet transform at each height provides a measure of how well the signal matches the wavelet function at various scales, allowing for the detection of boundaries. The Mexican Hat wavelet is named for its shape, which resembles a traditional Mexican hat or sombrero.

Morlet wavelet

The Morlet wavelet (Cohen, 2019) is a complex sinusoidal wavelet, named after Jean Morlet, a French geophysicist who developed it for analyzing seismic signals. It combines a sine function with a Gaussian envelope, that makes it effective for detecting oscillatory patterns. The Morlet wavelet function can be expressed as:

$$\psi(t) = \frac{1}{\sqrt[4]{\pi\sigma^2}} \exp\left(-\frac{t^2}{2\sigma^2}\right) \exp\left(i\omega_0 t\right) \tag{3.3}$$

where σ is the standard deviation of the Gaussian envelope, controlling the width of the wavelet and ω_0 is the central frequency of the sinusoidal component, defining the number of oscillations within the wavelet.

• The component $e^{\frac{-t^2}{2\sigma^2}}$ is the Gaussian envelope and ensures that the wavelet is localized in time, or in other words captures the features that occur within a specific time window of the signal.

• The component $e^{i\omega_0 t}$ is the imaginary part and is a phase-shifted version of the real part, introducing oscillations within the Gaussian envelope.

The Morlet wavelet is used in various applications. It is useful for identifying time-varying frequencies in signals, for extracting features from signals that have oscillatory or periodic components and for analyzing complex signals where frequency content changes over time.

Haar wavelet

The Haar wavelet is one of the simplest wavelets, characterized by its piecewise constant function, and named after Alfréd Haar, a Hungarian mathematician who introduced it.

$$\psi(t) = \begin{cases} 1, & \text{for } 0 \leq t < \frac{1}{2} \\ -1, & \text{for } \frac{1}{2} \leq t < 1 \\ 0, & \text{otherwise} \end{cases} \tag{3.4}$$

The Haar wavelet (Stanković and Falkowski, 2003) is discontinuous step-function, well-suited for detecting abrupt changes or sharp transitions in a signal. For ABL top detection, there are several factors to be taken int account when using the Haar wavelet. It is good for sharp boundaries and strong inversions, and also it is simple and computationally efficient. On the other hand, this method might miss or poorly resolve smoother transitions in the atmospheric profile that could also correspond to important layers, due to its limited sensitivity to gradual changes. In the figure below, a comparison of three wavelet functions (Haar, Marr, and Morlet) is attempted, each applied to the conceptual signal represented by the maroon line. This conceptual signal could represent a typical lidar backscatter profile, commonly used to detect the ABL top. The dashed magenta line indicates the height of the ABL top, derived by wavelet analysis. Each wavelet function is represented by a blue line. The objective here is to assess how well each wavelet function can detect the abrupt change in the signal that may correspond to the ABL top.

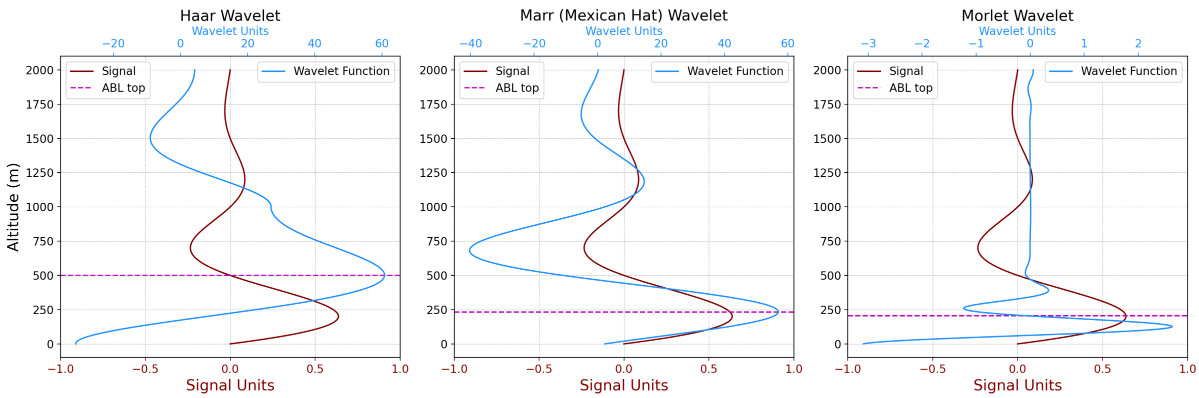

Figure 3.1: Comparison of the Haar (left), Marr (middle), and Morlet (right) wavelet functions (blue lines) applied to a conceptual signal (maroon line), which simulates a Lidar backscatter profile. The dashed magenta line indicates the detected height corresponding to the ABL top.

The interpretation of ABL top from a Lidar signal, primarily relies on the principle that aerosol concentration is typically higher within the ABL compared to the free troposphere above. The system emits laser pulses into the atmosphere and measures the backscattered signal, which is the portion of the back-scattered light by aerosols, molecules, and other particles in the atmosphere. Since aerosol concentration is higher in the ABL, the backscatter intensity is generally stronger within the ABL and decreases sharply at the ABL top, where aerosol concentrations drop off in the free troposphere. Therefore, the ABL top is often characterized by an abrupt decrease in backscatter signal. In Fig. 3.1, a reasonable value for this, is the level of 500 m (especially for a marine atmospheric boundary layer that is usually shallow).

The Haar wavelet detects properly the ABL top close to 500 m. In contrast, both the Marr (Mexican Hat) and Morlet wavelets detect the boundary layer top at a lower altitude: at 250 m. This discrepancy could be attributed to their smoother structure, which tends to blur sharp features in the signal and can result in an over-smoothed detection of the ABL top. However, with appropriate adjustments to their parameters, such as refining the scale or the width of the wavelets, these wavelets could potentially yield a more accurate detection. The results here demonstrate the importance of selecting and tuning the appropriate wavelet for detecting specific features in the signal. While the Haar wavelet may be more accurate in detecting sharp transitions, the other wavelets could provide useful information when applied to smoother or more oscillatory features within the atmospheric boundary layer structure. In this dissertation, the Haar wavelet function is primarily used when applying the WCT method.

After deciding which wavelet function is more proper for detecting the ABL top, the covariance of the wavelet transform is used to highlight the correlation between changes in the atmospheric profile and the wavelet at different scales. The covariance function is computed as:

$$\mathrm{Cov}(f,g) = \sum_{i=1}^{N}(f_i - \overline{f})(g_i - \overline{g}) \tag{3.5}$$

For atmospheric applications of WCT, f and g represent the vertical gradients of variables like temperature, humidity, or aerosol backscatter signal. In case of one vertical profile, like a backscatter profile, the WCT method is adapted to work with a single profile, as long as the wavelet transform reveals features within that profile, particularly the variations or gradients within it.

First, the CWT of the given profile f(z) is computed (where z represents the vertical height) as described in eq. (3.1). Then, the result of the CWT will be a set of coefficients that vary with scale a and position b. These coefficients represent how well the wavelet function matches the profile at different scales and positions. The scale of the wavelet transform corresponds to different vertical resolutions or levels of detail in the profile. In Fig. 3.2, different scale parameters are displayed for the products of backscatter coefficient and water vapor mixing ratio from Lidar. The bigger the scale, the smoothr the profile. If a very big scale parameter is used, there is the risk of smoothing-out specific characteristic of the profiles, while on the other hand, a small scale parameter leads to a very noisy profile that detecting extrema might be challenging.

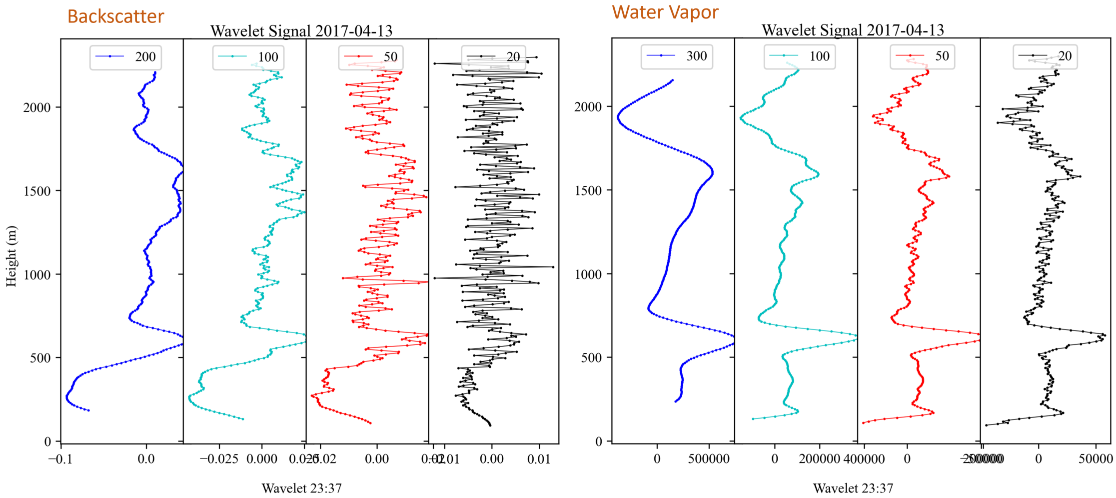

Figure 3.2: Wavelet produced by using different dillations, a=200 (blue), a=100 (cyan), a=50 (red) and a=20 (black), for the variables of backsatter coefficient 1064 nm (left) and WVMR (right)

After this step, the self-covariance of the wavelet coefficients is computed by the covariance at different scales to identify significant features. This way, the self-covariance can reveal patterns within the profile.

$$\mathrm{Cov}(W_\psi(f,a_1), W_\psi(f,a_2)) = \frac{1}{N}\sum_{i=1}^{N}\left(W_\psi(f,a_1,b_i) - \overline{W_\psi}(a_1)\right)\left(W_\psi(f,a_2,b_i) - \overline{W_\psi}(a_2)\right) \tag{3.6}$$

Here, $\overline{W_\psi}(a)$ represents the mean wavelet coefficient at scale a, and b_i are the positions along the profile. The scale parameter a, controls the width of the wavelet function. A larger scale corresponds to a wider wavelet and captures lower-frequency (smooth) components of the signal, while a smaller scale corresponds to a narrower wavelet and captures higher-frequency (fine) components. In other words, scales refer to how the wavelet is stretched or compressed, which affects its sensitivity to different features in the data. When analyzing a signal or profile, it's common to apply the transform at various scales to capture different levels of detail. For example, a scale a_1 might be used to capture broad, smooth features, while a scale a_2 might capture finer, more detailed structures. The covariance function assesses how the wavelet coefficients at those different scales a_1 and a_2 co-vary with each other, in order to understand how different levels of detail in the signal are related and highlight significant features like boundaries. For example, a strong covariance between scales might indicate a consistent feature or transition across different levels of detail, such as the boundary layer top.

In this study, the Haar wavelet function is implemented with a focus on integrating over specific windows of the profile. This implementation doesn't explicitly involve the scale parameter a in the traditional sense. To achieve this, the width of the window used for integration is modified by adjusting the number of data points included in each half of the window. In this case, the alpha parameter can be adjusted to represent different scales. Smaller values of alpha correspond to finer scales (narrower windows), and larger values correspond to coarser scales (wider windows). Once the wavelet line is correctly produced, the peaks are identified using Python tools, or in many cases manually. They correspond to regions of strong vertical gradients (like the ABL top). Multiple peaks may appear, especially in complex environments like coastal areas, or an aerosol-rich lower part of troposphere. The challenge is to distinguish which peak corresponds to the true ABL top. That typically requires additional analysis or thresholds based on the magnitude of the wavelet coefficients at certain scales.

3.2.2 Applications

In this section, some applications of the WCT method are described with technical details. The WCT method can be applied to any profile to detect sharp changes, making it useful for identifying layers in the atmosphere. Figure 3.3 conceptually depicts profiles of Range Corrected Signal (RCS), Water Vapor Mixing Ratio (WVMR) and BackScatter Coefficient, as well as the equivalent wavelet profiles. The Haar function is used, as described in section 3.2.1.

In this study, the WCT is used on backscatter and water vapor data from lidar averaged over 15- or 30-minute intervals. The next figure 3.4 visually represents this process.

On the left, the backscatter coefficient profile at 1064 nm from the PollyXT Lidar is shown. When this profile is averaged over 15 minutes period (blue line on the right), the wavelet transform can be computed (red line). The wavelet transform highlights changes in the profile, with maxima indicating potential layering. In this example, two distinct maxima appear around 900 m and 1500 m, suggesting layer boundaries.

Determining which maximum corresponds to the ABL top involves considering multiple factors, such as the time of day, the geographic location (coastal vs. continental), and the relative strength or depth of each maximum.

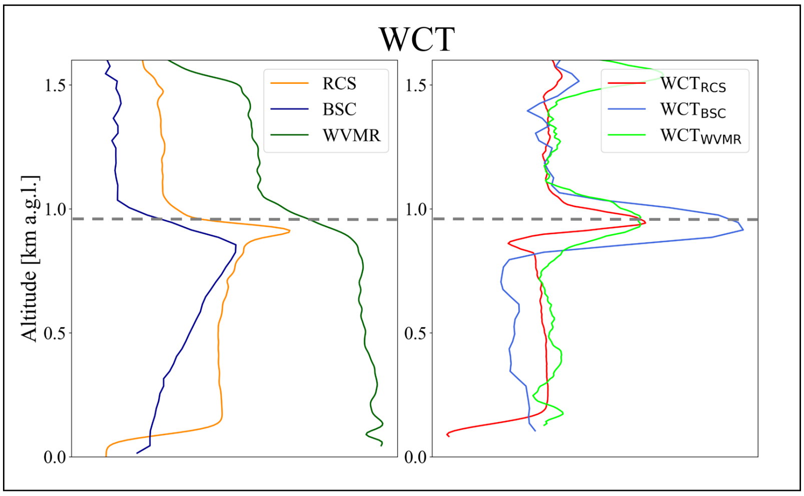

Figure 3.3: Conceptual WCT on different products: RCS (red), BSC (blue) and WVMR (green). The lighter colors are the products' profiles and the darker colors (right) are the corresponding wavelets of these products.

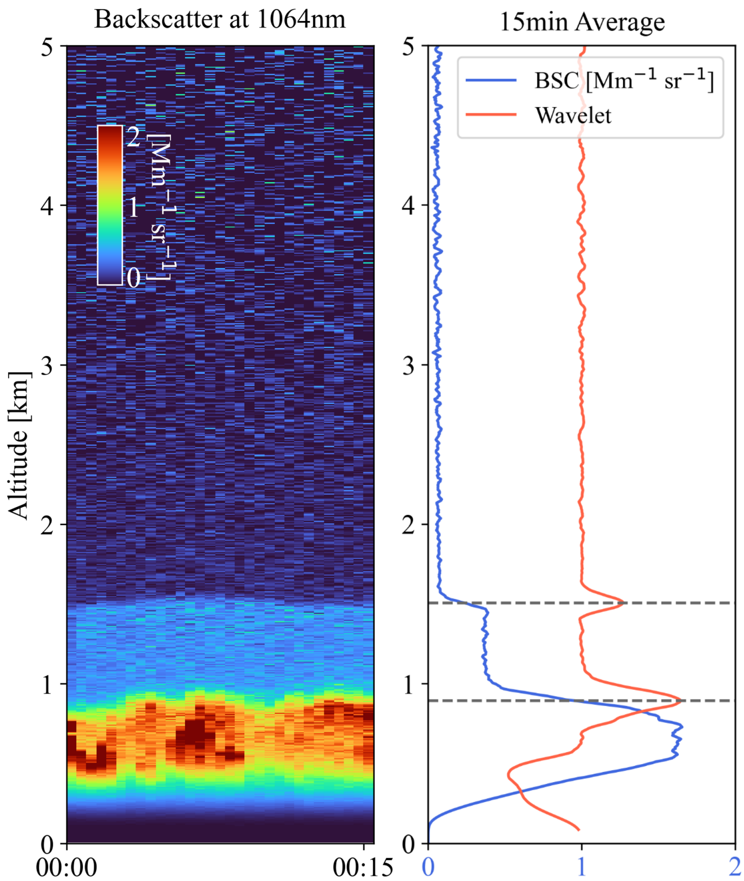

Figure 3.4: WC demonstration. Left: Backscatter coefficiet 1064 nm from PollyXT lidar, time-height cross-section. Right: 15-minute averaged profile (blue color) and the corresponding wavelet (red color).

An example of this technique is shown in Figure 3.5, where the WCT is applied to 10-minute averaged profiles of the 1064 nm backscatter coefficient. When there is a clear difference in the backscatter signal, it becomes relatively straightforward to identify the sharp changes in the wavelet transform, indicated by black stars. This measurement, taken in Finokalia—a coastal region in Crete—exhibits minimal daytime boundary layer evolution, allowing us to estimate an average boundary layer height of 647 ± 113 meters. This is a good example of effectiveness of the WCT in detecting well-defined layering. Further discussion of the dynamics that shape this behavior will follow in Chapter 4.

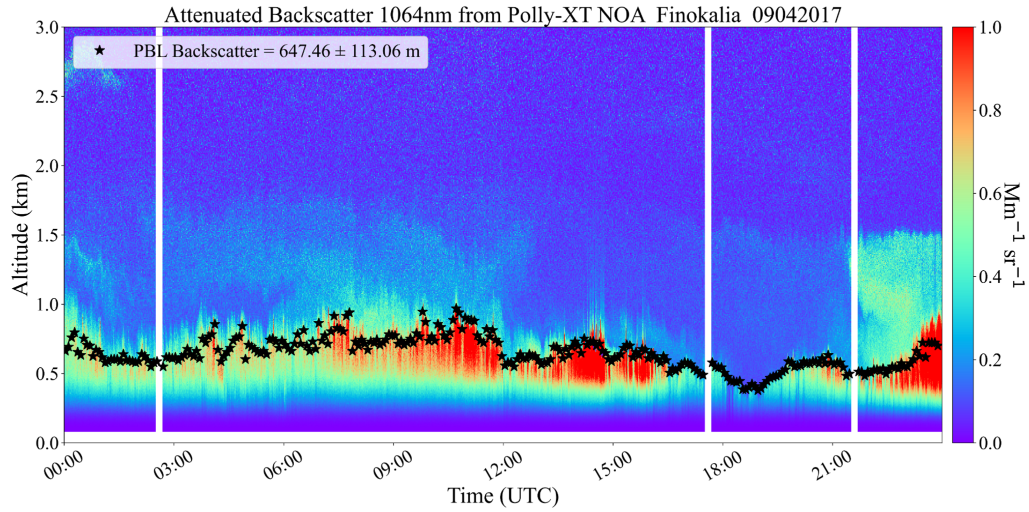

Figure 3.5: Attenuated Backscatter Coefficient 1064 nm, fr the case of 9 April 2017, Finokalia. The black stars indicate the PB height derived from the WCT method, and the mean is found 647.46 ± 113.06m

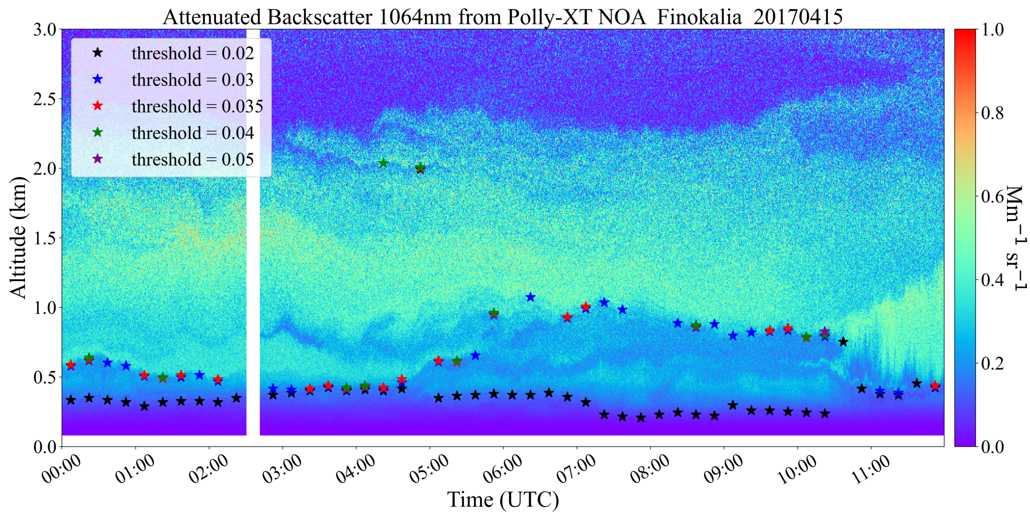

Figure 3.6: WCT method applied on attenuated Backscatter coefficient for the case of 15 April 2017, Finokalia. Different thresholds are tested to detect the layering.

It is not always easy to identify the correct change in the wavelet profile, as it depends on various factors, including the dilation used in constructing the wavelet, the criteria for selecting the maximum corresponding to the layer of interest, and the specific product to which the WCT is applied. One approach is to set a threshold; if the wavelet amplitude exceeds this threshold, the layer is considered identified. Figure 3.6 illustrates different threshold levels applied to the wavelet profile. However, this approach complicates automation, as the optimal threshold may vary with signal strength, being case dependent. Consequently, it was not pursued further in this study.

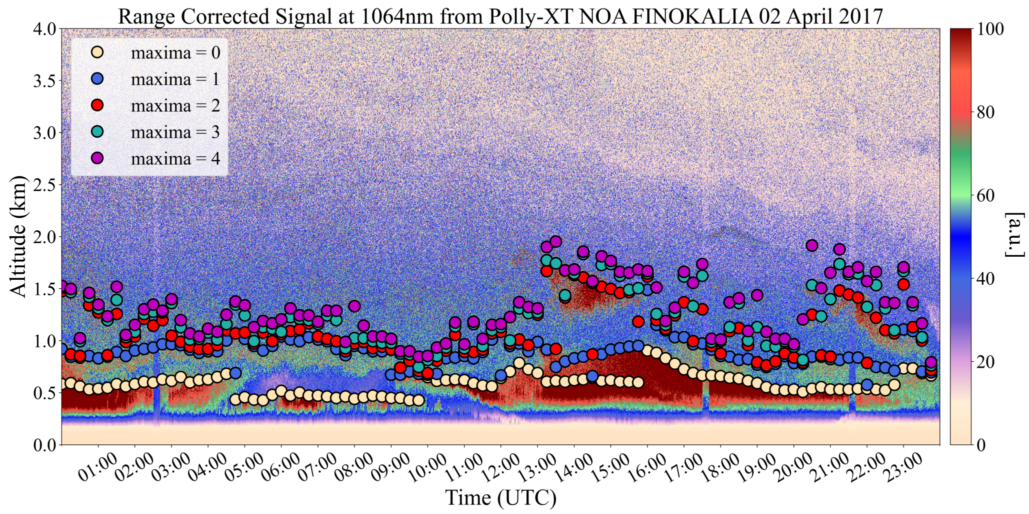

Figure 3.7: WCT method applied on attenuated Backscatter coefficient for the case of 2 April 2017, Finokalia. Different maxima are detected to match the ABL top.

A more effective way, is the automatic detection of extremum (in this case maximum) in each wavelet profile. This can be achieved with the find peaks function of python. The challenge here is in cases where more than one maximum is presented. Several criteria can be set through the function, like the width of the maximum, the intensity, the distance of the different maxima and the prominence. Different maxima are displayed for one case in Fig. 3.7. The white circles identify a shallower layer that likely be the boundary layer or a mixing layer. The blue cirles spot a layer located higher. The maxima higher than these may be attributed to elevated aerosol layers. Empirically in this study, only the first three maxima of wavelet are examined as possible ABL top identifiers.

A more effective approach is automatically detecting extrema (in this case, maxima) within each wavelet profile, which can be accomplished by using the Python's SciPy library `find_peaks` function. For more details, the official documentation is found at SciPy find_peaks. The main challenge lies where multiple maxima appear within the profile. This function allows for setting criteria such as peak width, intensity, distance between peaks, and prominence to refine peak selection. Figure 3.7 illustrates the results, with white circles marking a shallower layer that likely represents the boundary or mixing layer, while blue circles indicate a higher layer. Maxima above these may be attributed to elevated aerosol layers. For this study, only the first three wavelet maxima are considered as potential indicators of the ABL top, based on empirical observations.

Another important factor to consider is the relationship between the dilation (or scale parameter) and the resulting maxima in the wavelet profile. A smoother profile (achieved with a larger dilation) may obscure some maxima, while a more detailed, noisier profile

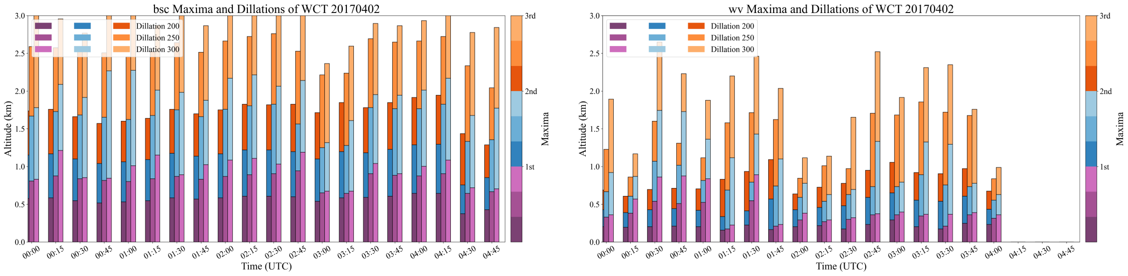

Figure 3.8: Sensitivity Analysis for WCT: the dilation is plotted versus maxima for a single case. The colorbar represents different maxima: purple marks the first maximum, blue indicates the second, and orange shows the third. The color intensity reflects the level of dilation according to the label: darker tones represent lower dilation, while lighter tones correspond to higher dilation. left panel is the backscatter product and right panel is the WVMR product.

(from a smaller dilation) can produce multiple maxima, potentially leading to incorrect interpretations of layer structures. Figure 3.8 presents a sensitivity analysis of dilation versus maxima for a single case. The color scheme highlights different maxima: purple marks the first maximum, blue indicates the second, and orange shows the third, as per the color bar. The color intensity reflects the level of dilation: darker tones represent lower dilation, while lighter tones correspond to higher dilation.

We observe that as dilation increases, the detected maxima tend to shift to higher altitudes. This trend is expected, as smoothing a maximum broadens it, and effectively shifts its perceived location. An empirical guideline from this study suggests that, for backscatter profiles, the first maximum detected with a dilation around 200 (or sometimes lower) often represents the ABL top in the examined cases. However, this does not hold for the water vapor mixing ratio profiles, which are noisier. Due to the inherent variability in lidar-derived water vapor data, higher smoothing (larger dilation) is found beneficial to reveal significant extrema more clearly by reducing noise-induced peaks. This tailored approach ensures that the WCT method in this study, yields meaningful results in the varied conditions across the datasets.

Each lidar product carries distinct information about atmospheric properties. The backscatter coefficient primarily represents aerosol presence, while the water vapor mixing ratio indicates atmospheric moisture levels. Both aerosol concentration and moisture are commonly confined within the ABL, so detecting sharp changes in these quantities can effectively trace the ABL top. This approach is especially relevant in marine environments, like islands and coastal areas, where the lower layer is enriched with marine aerosols from the sea.

In some cases, the lidar overlap function may exceed the ABL top, which limits our ability to detect it using backscatter alone. The water vapor mixing ratio, however, is less affected by overlap issues because it is derived from the ratio of two channels, which reduces the impact of overlap assumptions. In Fig. 3.9, the WCT results for the two products are shown, with red circles marking backscatter results and blue stars indicating water vapor mixing ratio findings. It is important to note that the water vapor mixing ratio measurements are not available during the day because the specific channel (407 nm) does not operate effectively under daylight conditions. Despite this, there is strong agreement

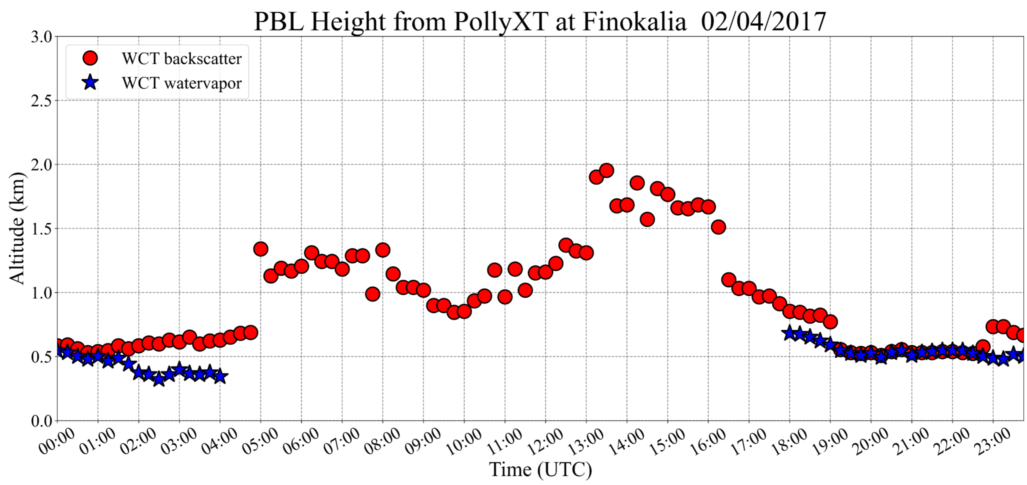

Figure 3.9: WCT applied on two different products of PollyXT Lidar: the backscatter coefficient (red circles) and the watervapor mixing ratio (blue stars).

between the two products in detecting ABL features.

3.3 Gradient Method (GM)

The Gradient Method is a widely used technique for detecting boundaries or transitions in various types of data Palm et al. (1998). In general, it involves calculating the rate of change of a variable with respect to another variable. In atmospheric studies the latter is typically the height or pressure, as the vertical structure is usually the subject of interest. The boundary layer top is often characterized by a sharp change in gradients of atmospheric variables, especially a daytime well-mixed layer, or a very stable nocturnal layer.

3.3.1 General Description

The gradient G(z) of a variable X(z), which is a function of height z, expresses the rate of change of X with height and is defined as:

$$G(z) = \frac{dX(z)}{dz} \tag{3.7}$$

A strong gradient (large G(z)) indicates a rapid change in the variable, which is often associated with the existence of a layer in the atmosphere. In atmospheric studies, the Gradient Method is frequently applied on vertical profiles of temperature, humidity, or other variables to detect layers and boundaries (e.g. Li et al. 2021). For detecting the ABL top, the method can also be applied on specific humidity or potential temperature or wind speed, to identify a significant change, as the boundary layer typically exhibits sharp contrasts with the free atmosphere above it. For example, the gradient of potential temperature $G_\theta(z) = \frac{d\theta}{dz}$ with respect to height z, is used to detect temperature inversions. Similarly, the gradient of humidity can reveal moisture layers, and wind gradients can indicate shear zones at the boundary layer top. In these cases, a rapid increase in potential temperature or a rapid decrease in humidity often means the transition to the free troposphere.

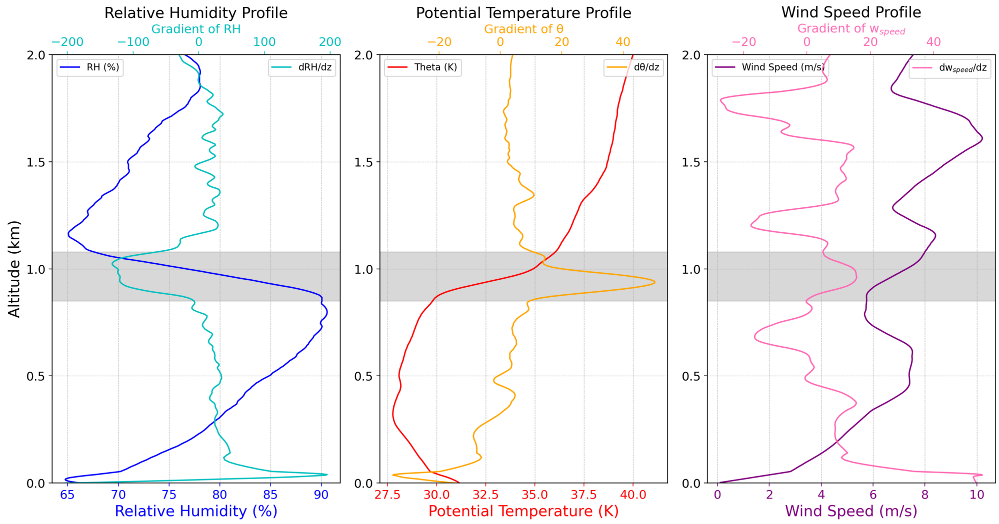

Figure 3.10: Conceptual representation of Gadient method. Left: relative humidity profile (blue line), middle: temperature profile (red) and right: wind speed(purple), along with the corresponding gradients (cyan, orange, pink, respectively).

In Fig. 3.10, the gradient method is demonstrated for application on different atmospheric parameters. The plots display relative humidity (blue), potential temperature (red), and wind speed (purple) on the x-axes, each plotted as a function of height. There is significant reduction of relative humidity and increase of potential temperature around 850 – 110 m (grey shaded area). While these features indicate the top of the ABL, interpreting the wind profile can be more challenging. Wind speed often exhibits various layers of shear and turbulence that can be frequent and complex in the lower troposphere. Consequently, wind speed alone may not reliably pinpoint the ABL top. Instead, it is necessary to combine this with other variables such as temperature and humidity. This way, the risk of misinterpreting wind shear as the boundary layer boundary can be avoided.

3.3.2 Applications

In this study, the Gradient Method is primarily applied to radiosonde profiles. Radiosondes provide high-resolution vertical profiles of atmospheric variables, consisting an excellent tool for identifying the ABL top. By calculating the gradients of key variables such as temperature and humidity, this method will be used to pinpoint the sharp changes that indicate the boundary layer height. Although the Gradient Method can be applied to any vertical profile data, including Lidar and aircraft measurements, in this study, the focus is on radiosonde data for ABL detection. This approach provides a robust and well-established method for identifying the ABL top in complex coastal environments, where gradients can be more subtle or influenced by local factors.

Using the potential temperature over simple temperature in the Gradient Method for detecting ABL top, is based on several important factors. Firstly, potential temperature is a conserved quantity for an air parcel moving adiabatically, meaning it is not significantly influenced by changes in pressure or humidity. This makes it a more reliable indicator of the vertical thermal structure of the atmosphere. On the other hand, the simple temperature is more directly affected by local variations in moisture content, pressure, and surface heating, which can complicate its use in identifying the true boundary layer structure. Additionally, potential temperature provides a better representation of the stability of the atmosphere. A rapid change or gradient in potential temperature is often observed at the boundary between the air of the ABL and the more stable air aloft. This sharp gradient is a key feature for locating the ABL top. Simple temperature, however, may exhibit more gradual changes due to effects like solar heating or diurnal cooling, which do not necessarily reflect the boundary layer's vertical structure.

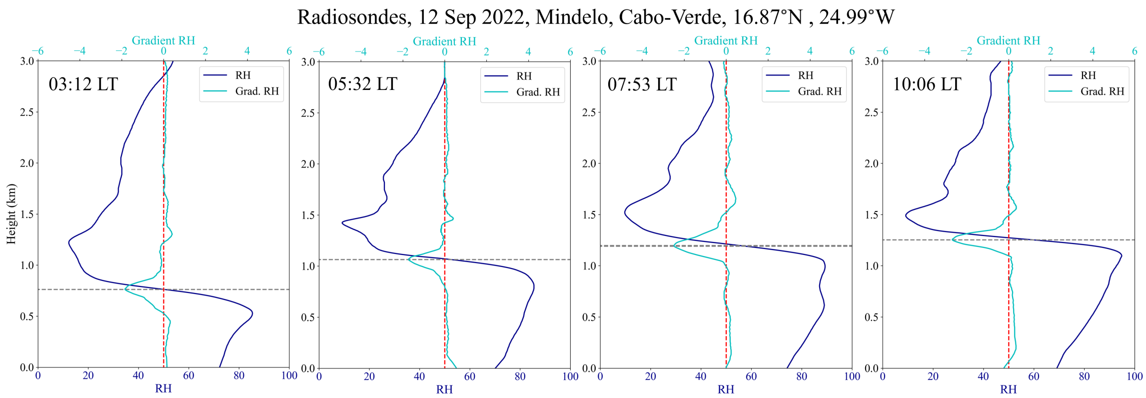

Figure 3.11: RH profiles (dark blue) from Radiosondes launched in 12 September 2022, 03:12, 05:32, 07:53, 10:06 local time, at Mindelo, cabo verde. The gradients are depicted with cyan lines.

Figure 3.11 shows relative humidity (RH) profiles obtained from four radiosondes launched at Mindelo, Cabo Verde, on 12 September 2022, at local times 03:12, 05:32, 07:23, and 10:06. In these profiles, the dark blue lines indicate the RH values, while the light blue lines represent the RH gradients. Minima in the RH gradients are marked by grey dashed lines, which indicate potential Atmospheric Boundary Layer (ABL) top heights.

As time progresses, we observe an increase in the ABL top height. This increase aligns well with the conditions of 12 September, a particularly windy day. Around 07:30, as the sun rose, the heating of the surface led to temperature gradients, and the wind intensified. Given the location—a small island in Cabo Verde—strong daytime ABL evolution might not typically be expected due to the moderating influence of the sea. However, the rise in the ABL height observed here can likely be attributed to the strengthening winds, which enhanced mechanical turbulence. This mixing effect elevated the ABL top throughout the morning.

In Figure 3.12, the profiles for 23 September 2022 present challenges in identifying the ABL top using the gradient method, as the inversions are not particularly strong. The dark red and dark blue lines represent potential temperature and relative humidity respectively,

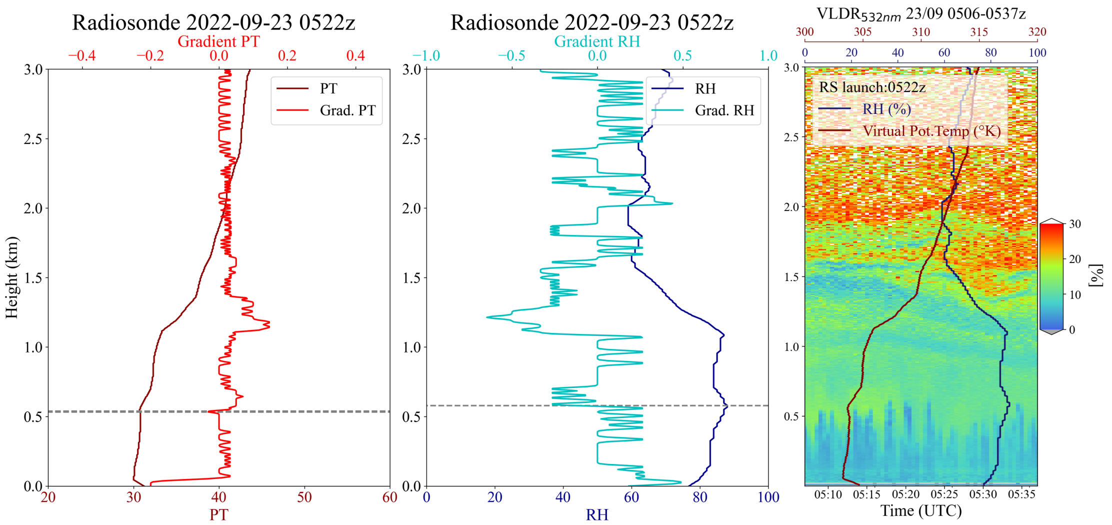

Figure 3.12: left: Potential Temperature (dark red) and the gradient (red), middle: RH profile (dark blue) and the gradient (light blue), right: Volume Linear Depolarization Ratio from PollyXT Lidar, 30 minutes averaging around the radiosonde launch: 05:22 UTC, 23 Sep 2022

while the light red and light blue lines show their corresponding gradients. The ABL top is indicated by the gray dashed line, which marks the maximum of the temperature gradient and the minimum of the RH gradient around 500m.

The most prominent inversion occurs around 1200 m, but it is unlikely to correspond to the ABL top. Given the launch time of 04:22 local time, the coastal location, and weak winds, this higher inversion is probably related to the existence of a residual layer. Instead, a weaker inversion around 500 m is more likely to represent the ABL top. This discrepancy could be due to dust presence in the atmosphere on this particular day. On the right of Fig. 3.12 the volume depolarization ratio from the 532 nm channel of PollyXT shows non-spherical aerosols. Depolarization values around 5% indicate marine aerosols, while values in the range of 20-25% indicate dust, suggesting dust mixtures within the boundary layer. These dust aerosols, with distinct temperature and humidity properties, can alter the thermodynamic profile, which may reduce the inversion strength.

Overall, while the gradient method is highly effective for detecting layering, certain limitations arise when inversions are weak. In such cases, complementary strategies are recommended: examining multiple variables (e.g., temperature and RH), and analyzing wind and aerosol data. This is not an inherent flaw of the gradient method but rather reflects the complexity of identifying the ABL top in environments with strong aerosol and meteorological variations. Consequently, automated detection of the boundary layer top remains challenging in such dynamically complex regions. Comerón et al. (2013) emphasized on identifying layering by using the gradient and the WCT method.

3.4 Threshold Method (TM)

In this chapter, the Threshold Method (TM) is explained. The TM relies on setting a specific, constant threshold value, which is used to identify the turbulent Mixing Layer

Height (MLH) within a profile (Vakkari et al., 2015) and is often used in studies that incorporate Halo Wind Lidar Data (see also 2.3.1), as in O'Connor et al. (2010); Vakkari et al. (2019). Figure 3.13 illustrates this concept: the red dashed line represents the chosen threshold value, the black dashed line shows a conceptual TM profile, and the purple circle highlights a potential MLH top. In this study, the TM is applied to turbulent kinetic energy dissipation rate (TKE) profiles from the Halo Wind Lidar, as introduced in Section 2. The process works as follows: starting from the lowest usable range gate, the algorithm moves upward through the profile as long as the TKE values exceed the set threshold. The altitude at which TKE first falls below this threshold is interpreted as the MLH. It's important to note that the MLH doesn't always align with the ABL top. This is because the ABL may also include a residual layer, especially after sunset, when turbulent mixing from the previous day may persist at higher altitudes.

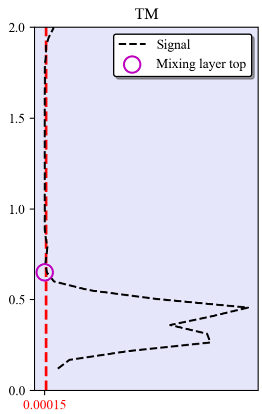

Figure 3.13: TM conceptual representation: black dashed line corresponds to the Signal on which the method is applied (in this study TKE_{dr}), red dashed line is the threshold and the purple circle describes the retrieved MLH top.

In Figure 3.14, the TM is demonstrated using two different threshold values: 10^{-4} and $0.5 \cdot 10^{-4}$ with yellow and brown circles respectively. TKE profiles, averaged every 15 minutes, are analyzed using these thresholds, with specific time steps—06:60 and 15:15—highlighted in detail. While the difference between the identified MLH heights for these two thresholds is relatively small, it illustrates a key challenge: selecting an appropriate threshold value. Minor variations in the threshold can lead to different interpretations of the MLH, which highlights the importance of careful threshold selection for accurate results.

In this dissertation, an empirical approach found that using the median of TKE profiles every hour yields more accurate results for identifying the MLH. Calculating the mean instead of the median would lead to an overestimation of MLH during nighttime, and smoothing alone cannot resolve this. This is due to the logarithmic nature of TKE, where even a single high TKE value within the averaging period can significantly skew the mean upward.

Figure 3.15 illustrates these results, with black stars indicating the detected MLH. While the TM is simple and effective, especially for identifying MLH in cases with clear,

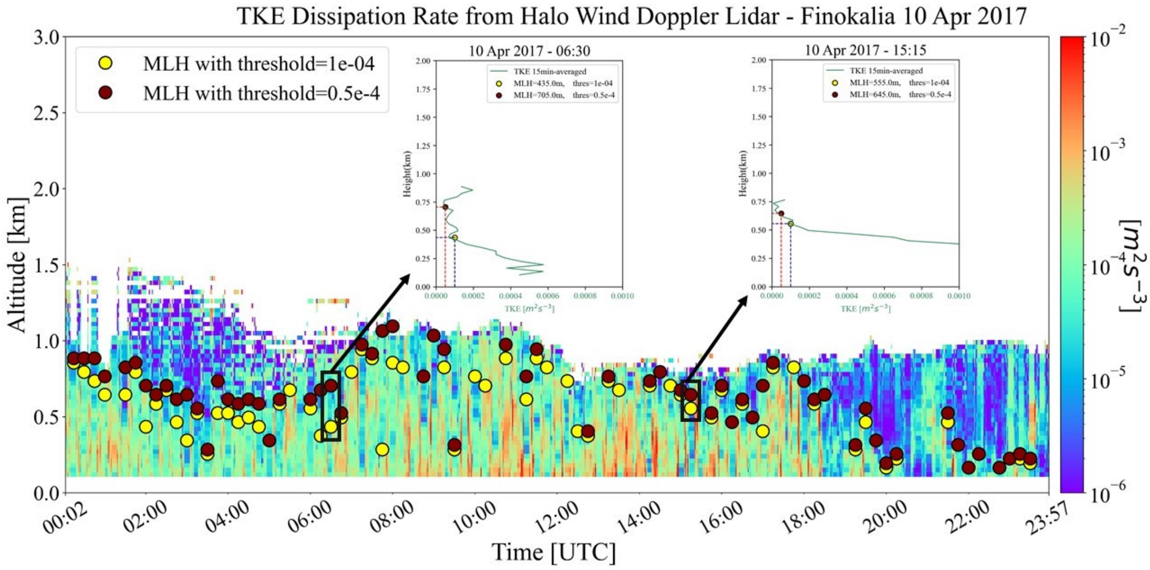

Figure 3.14: TM applied for the case of 10 April 2017, in Finokalia. The thresholds of 10^{-4} (yellow circles) and $0.5 \cdot 10^{-4}$ (brown circles) are tested and 2 profiles for 06:30 and 15:15 are presented in detail.

distinct turbulence, it is applied here specifically to estimate MLH from turbulence parameters. The method works well in straightforward situations but has limitations when it comes to more complex layering conditions.

For example, if a pocket of calm air exists within a turbulent layer, the TM may incorrectly identify this calm region as the MLH. Additionally, in scenarios such as sea breezes or layered flows with different directions at varying altitudes, two distinct turbulent layers can appear with little to no mixing between them. In such cases, excessive smoothing could overestimate the MLH, as it would fail to distinguish between separate turbulent layers. These limitations underscore that while TM is practical for certain purposes, it may not be suitable for capturing the full complexity of layered atmospheric conditions.

3.5 Richardson Method (RM)

The Richardson method is a widely used technique to calculate the top of the ABL based on the analysis of vertical profiles of temperature and wind (Fedorovich et al., 2004, Yamada, 1977). It relies on the Richardson number, which is a dimensionless number that characterizes the relative importance of buoyancy versus shear in the atmosphere. This method is particularly useful in identifying the transition from the well-mixed, turbulent ABL to the more stable air aloft. The Richardson number compares the gradient of the buoyancy (which is related to the vertical temperature gradient) with the shear of the wind velocity in the vertical direction. It can be interpreted as a measure of the stability of the atmosphere. When the Richardson number exceeds a certain threshold, typically around 0.25, the atmosphere is considered to be unstable and turbulent, which is characteristic of the ABL. Conversely, values below this threshold indicate a more stable stratification, where turbulence is suppressed.

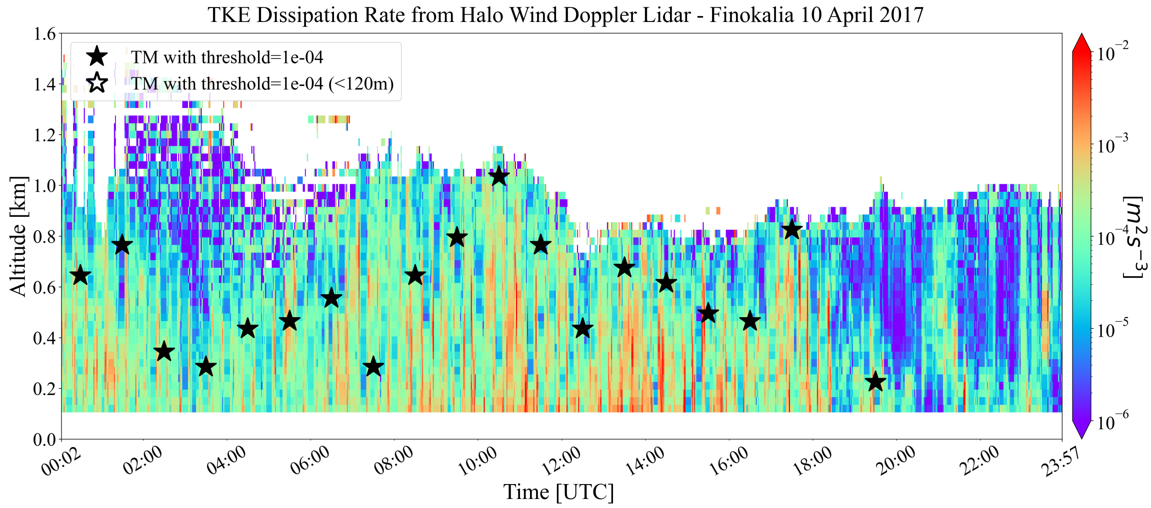

Figure 3.15: TM applied for the case of 10 April 2017, in Finokalia. The thresholds of 10^{-4} (black stars) with the threshold value of $0.5 \cdot 10^{-4}$.

3.5.1 General Description

The Bulk Richardson number (R_B), is useful for atmospheric applications. It is a dimensionless ratio that indicates the likelihood of turbulence in an atmospheric layer (Stull, 2012). This number balances the buoyant forces (which tend to produce or dampen turbulence) against the shear forces (which generally generate turbulence). The Bulk Richardson number is given by the formula:

$$R_B = \frac{g \cdot \Delta\overline{\theta_v} \cdot \Delta z}{\overline{\theta_v} \cdot [(\Delta\overline{U})^2 + (\Delta\overline{V})^2]} \tag{3.8}$$

where g is the gravitational acceleration, $\Delta\overline{\theta_v}$ is the mean difference in virtual potential temperature, Δz is the height difference, $\overline{\theta_v}$ is the mean virtual potential temperature, $\Delta\overline{U}$ and $\Delta\overline{V}$ are the mean changes in the horizontal wind components. The calculations are performed between the bins of each profile of measurement.

For this dissertation, the Richardson number was reconstructed from observational datasets and temperature profiles of the Weather Research and Forecasting (WRF) model. For the model's vertical meteorological parameters, we utilize the Advanced Research Weather Research and Forecasting model version 4.2.1 (WRF-ARW) (Skamarock et al., 2008). The WRF-ARW spatial set up was at 9 × 9 km resolution domain with 600 × 370 grid points and 33 vertical levels. Moreover, Polly-XT Raman Lidar is used to obtain the water vapor mixing ratio, which contributes to calculating the virtual potential temperature. Wind profiles are retrieved from the Halo Wind Lidar, and the temperature profile is derived from the WRF model outputs. By combining these three datasets, the Richardson number is calculated across various heights and times, generating a comprehensive Richardson number quicklook, as presented in the figures of next subsection (3.5.2).

3.5.2 Applications

To identify turbulent layers within the atmosphere, regions where the Richardson number is below a specific threshold are examined, as these are typically areas of active turbulence (Mahrt, 1999). The threshold value distinguishes layers where turbulent mixing is sufficient to consider the region part of the ABL.

Figure 3.16 illustrates this analysis, showing the Richardson number for 02 April 2017 during two time intervals: 00:00-04:00 UTC and 18:00-24:00 UTC. Measurements for daytime hours are unavailable because the water vapor channel of the Polly-XT Raman Lidar cannot function in daylight due to solar noise interference. These figures demonstrate also the chosen threshold's effectiveness in delineating the ABL.

To analyze the Richardson numbers and identify potential layers or sharp transitions, it is challenging to find clear patterns, given that the condition of 0.25 value does not apply in these cases. In the produced quicklooks, the variations in the Richardson number are not immediately obvious, making it difficult to visually discern distinct layering or the boundary layer top. To address this, manual adjustments were made to the colorbar limits in the figures to enhance the contrast between turbulent and non-turbulent regions. By fine-tuning these limits, it becomes easier to highlight areas where rapid changes or layering occur, which might otherwise be obscured in the original data range. These modifications were crucial for revealing the subtle variations in the Richardson number. However, it should be noted that this approach is not always straightforward, and the exact thresholds for defining layers depend on the sensitivity of the data and the atmospheric conditions at the time.

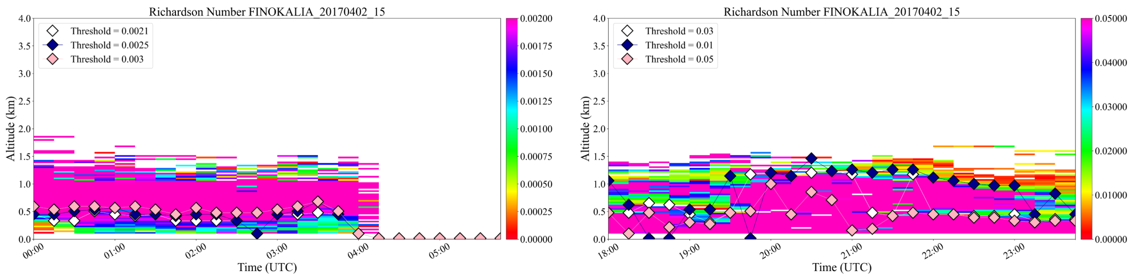

Figure 3.16: 2 April 2017, Richardson method tested with 3 thresholds: 0.0021 (white diamonds), 0.0025 (blue diamonds), and 0.003 (pink diamonds) for 00:00-04:00 UTC on the left panel, and thresholds of 0.03 (white diamonds), 0.01 (blue diamonds), 0.05 (pink diamonds) for 18:00-24:00 UTC on the right panel

In Fig. 3.16 left, the three chosen Richardson number thresholds do not show significant differences in the detected height of the potential PBL, which is consistently found around 500-600 meters. These values are reasonable, as during the nighttime in a stable coastal environment, we would not expect a particularly high boundary layer. In contrast, for the afternoon period of the same day (Fig. 3.16 right), there are noticeable differences in the identified layers across the three thresholds. The threshold of 0.01 (dark blue diamonds) identifies a higher layer around 1100 meters, while the greater threshold of 0.05 (pink diamonds) captures a lower layer around 500 meters. This suggests the potential presence of a residual layer above the more stable nocturnal layer. To further clarify these findings and to enhance the interpretation, it is helpful to compare the Richardson number results with those obtained using the WCT, as discussed in section 3.2.

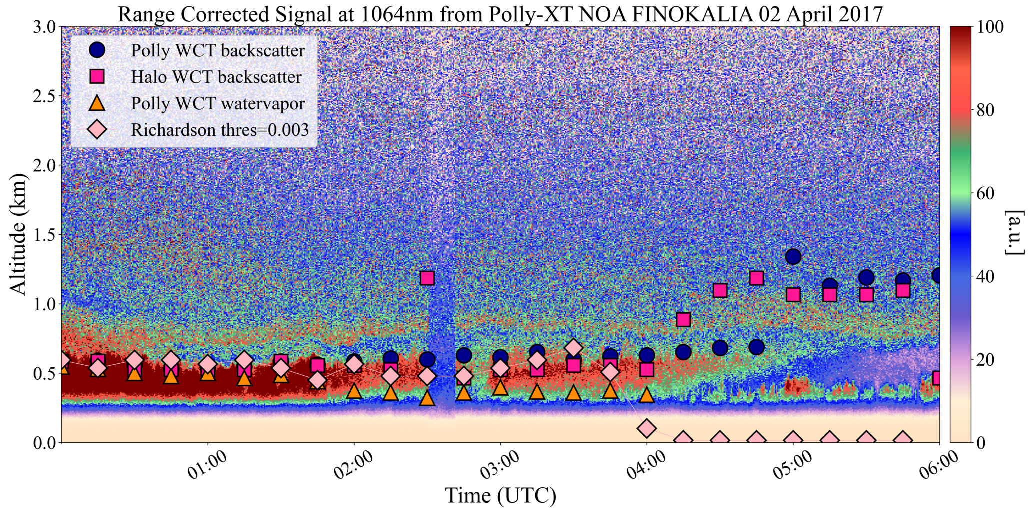

Figure 3.17: Comparison of Richardson method results for threshold 0.003 (pink diamonds), with results from the other methods: WCT on PollyXT backscatter (blue diamonds), and water vapor mixing ratio (orange triangles) for 2 April 00:00-04:00 UTC

Starting with the nighttime period, Fig. 3.17 presents the results from the WCT method. A threshold of 0.003 for the Richardson number is found to best match the other results. The WCT is applied to the 1064 nm backscatter coefficient (blue circles) and the water vapor mixing ratio (orange triangles) from the Polly-XT lidar, as well as the backscatter coefficient from the Halo Wind Lidar (dark pink squares). Early in the night (00:00–02:00 UTC), there is a good agreement across all derived ABL tops. However, after 02:00 UTC (approximately 05:00 local time and about one hour before sunrise), the results begin to diverge, with the backscatter data indicating a higher boundary layer height. The Richardon derived ABL top is not considered after 04:00 because of the unavailability of water vapor mixing ratio measurements. As the sun rises and the surface begins to heat, vertical mixing initiates, marking the start of the diurnal evolution of the ABL. However, in a coastal area like Finokalia, we do not expect strong evolution of ABL, therefore there is overestimation probably due to the complicated dynamics from the interaction of sea and land.

For the afternoon and night period from 18:00 to 24:00 (Fig. 3.18), the Richardson threshold of 0.05 (indicated by pink diamonds) aligns more closely with the results from other methods, especially after 21:30. In general, it is challenging to identify a single threshold value that consistently represents the true ABL top in the Finokalia dataset. This difficulty limits the extensive use of the Richardson method in this study.

Although other methods for detecting the ABL top also involve uncertainties, they generally require less manual adjustment and offer more consistent results than the Richardson number approach presented in this section. Additionally, applying the Richardson method required significant interpolation to align the different resolutions of the instruments (Halo and Polly-XT Lidar) and the WRF model, which is both time-intensive and a potential source of error. Due to these challenges and the lack of a reliable threshold,

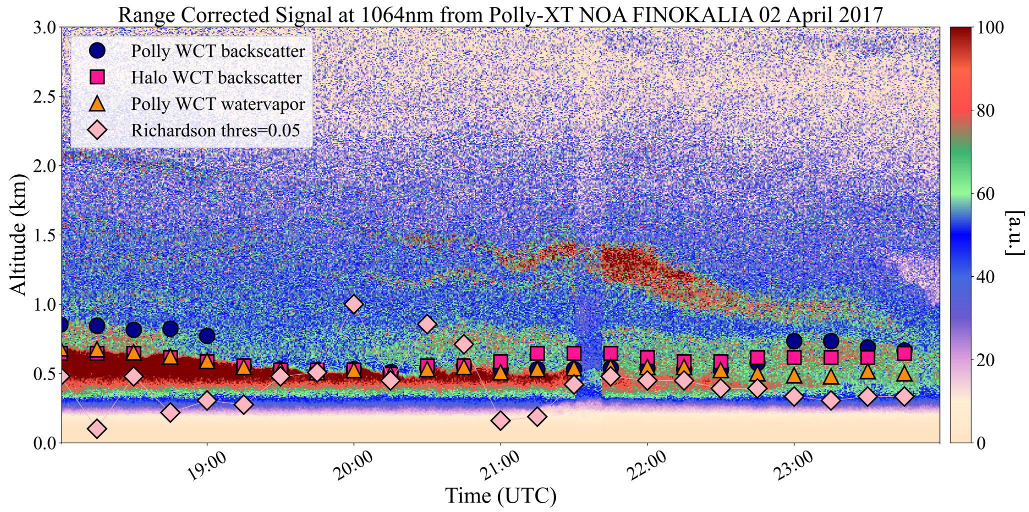

Figure 3.18: Comparison of Richardson method results for threshold 0.003 (pink diamonds), with results from the other methods: WCT on PollyXT backscatter (blue diamonds), and water vapor mixing ratio (orange triangles) for 2 April 18:00-24:00 UTC

the Richardson method is applied only selectively in this analysis.

3.6 Parcel Method (PM)

3.6.1 General Description

The Parcel Method (PM) is a thermodynamic approach, used to estimate the height of the Atmospheric Boundary Layer (ABL) by examining the behavior of an air parcel in relation to its surrounding environment. The PM involves postulating parcel displacements in an undisturbed environment and deducing the likelihood of such a displacement by estimating the kinetic energy change that would result (Thorpe et al., 1989, Collaud Coen et al., 2014). If an air parcel is conceptually lifted from the surface through the atmospheric column, the changes in temperature and density with height as it ascends through the atmosphere are estimated. Based on thermodynamic principles, the parcel's temperature is compared to the surrounding air temperature: if the parcel remains warmer and less dense than its surroundings, it continues to rise until it reaches a level where it is in equilibrium with the ambient air. To assess the buoyancy and stability of the parcel relative to its environment, the virtual potential temperature θ_v is used, rather than just temperature or potential temperature. Virtual potential temperature accounts for the effects of both temperature and moisture content in the parcel and is calculated according to:

$$\theta_v = \theta(1 + 0.61w - w_L) \tag{3.9}$$

where θ is the potential temperature, w is the water vapor mixing ratio (mass of water vapor per mass of dry air), and w_L is the liquid water mixing ratio (mass of liquid water per mass of dry air, accounting for any condensed water droplets, such as in clouds). The term $1 + 0.61w$ adjusts for the buoyancy effect of water vapor in the air, while the $-w_L$

term adjusts for the mass of condensed water, as liquid water droplets make the air parcel slightly heavier and reduce buoyancy. This version of the formula is relevant in saturated conditions (like in clouds) where liquid water is present. In unsaturated air (outside of clouds), w_L is effectively zero, so the simpler form $\theta_v = \theta(1+0.61w)$ suffices and is used in this study to simplify the analysis.

The moist air is less dense than dry air at the same temperature, therefore moisture impacts buoyancy. Virtual potential temperature adjusts the potential temperature to reflect these buoyancy effects, representing more accurately the parcel's tendency to rise or sink in the surrounding atmosphere. This is particularly important in the ABL, where moisture levels can vary significantly, especially in coastal areas. To determine the height of the ABL the virtual potential temperature of the lifted parcel is compared to that of the surrounding environment. In Fig. 3.19, a θ_v profile is presented. The ABL height is generally considered to be the level at which the environmental virtual potential temperature matches the surface value (purple dashed line). This point (red point) is significant because it indicates that the lifted parcel is no longer warmer (or more buoyant) than its environment and will stop rising due to the loss of buoyancy. This is the natural "cap" for the buoyant parcel, marking the top of the well-mixed boundary layer. This height also marks the boundary between the well-mixed, turbulent air below and the more stable air above. In a convective boundary layer, the air is mixed well enough that θ_v is roughly uniform with height. The top of the ABL is where the environmental θ_v increases sharply, indicating the beginning of a more stable layer with less vertical mixing.

The Parcel Method presents some limitations under certain atmospheric conditions, where identifying the ABL top becomes challenging.

• In weakly convective or Stable Conditions, as surface heating decreases, buoyancy weakens, and turbulent mixing slows down. This could happen in coastal areas and/or on cloudy days where the ABL is more stable and therefore the temperature gradient is weakened, making it difficult to precisely detect the ABL top.

• The residual layer can also pose limitations in this method. Usually in the afternoon, the daytime Convective Boundary Layer (CBL) begins to decay. This layer often has remnant turbulence from earlier in the day, but without strong buoyancy. The Parcel Method might misinterpret this residual layer as the ABL top, causing inaccurate detection. This is not exactly the case for coastal areas, as there is not strong daytime thermodynamic evolution.

• Lastly, moisture effects can also affect the results of PM. Over moist or coastal areas, high humidity near the surface and fluctuating moisture profiles can complicate the virtual potential temperature profile, making it harder to determine when the parcel reaches equilibrium with its environment. The PM is sensitive to surface virtual potential temperature as a starting point. If surface conditions fluctuate rapidly, it can lead to wrong results. For instance, sea breezes and local winds can alter the ABL structure in ways the method doesn't account for, leading to errors in ABL detection.

3.6.2 Applications

The radiosondes presented below, were collected during the ASKOS campaign, conducted in one of Cabo Verde islands, a region strongly influenced by marine and desert dust aerosols. Figures 3.20 and 3.21 display multiple profiles of virtual potential temperature, from different radiosoundings, classified over distinct time periods: 00:00-06:00 (deep

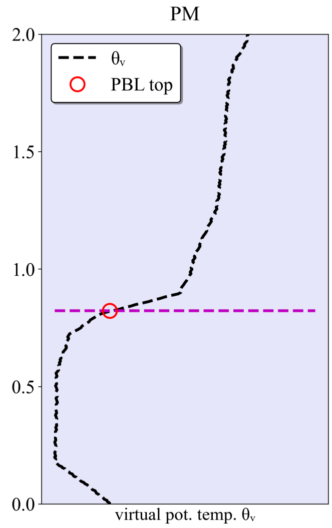

Figure 3.19: Conceptual representation of parcel method. The black dashed line is the virtual potential temperature (θ_v)and the purple dashed line corresponds to the level where the θ_v has the same value as the surface.

night), 06:00-09:00 (morning), 09:00-14:00 (noon), 14:00-17:00 (afternoon), and 17:00-24:00 (night), all local time. Each of these intervals represents different stability and lighting conditions of the lower troposphere, influencing the vertical structure and thermal stratification of the air. The virtual potential temperature at the surface is approximately $17-18°C$, but this temperature does not appear at any reasonable point in the profiles to be matched with the ABL top (according to the methodology), because of instability. This is likely due to the increased moisture near the surface from the sea, which can affect the virtual potential temperature. As a result, the ABL top is more accurately identified at the area where there is an increase in virtual potential temperature (shaded areas in Fig. 3.20 and 3.21), reflecting the transition from the mixed boundary layer to the more stable air above.

The deep night profiles (00:00-06:00) consistently show an increase in virtual potential temperature at heights between approximately 700-1000 meters, indicating a stable and relatively uniform ABL top during this period. In contrast, the morning (06:00-09:00) and noon (09:00-14:00) profiles locate this increase across a wider and more dispersed range of altitudes. Though this is a coastal region with limited daytime evolution, there is still some influence from the continental surface, which drives a moderate daytime rise of ABL. This evolution is influenced not only by thermodynamic changes—as solar heating increases mixing—but also by the development of winds driven by temperature gradients. As morning progresses, these winds gain strength, shaping the ABL structure as they respond to the differences in temperature between land and sea.

In the next figure, we are examining the afternoon (14:00-17:00) and the night (17:00-24:00) profiles. During the afternoon, buoyancy remains strong, though gradually decreasing as the sun lowers, leading to less vigorous mixing. As the sun sets, the surface cools, leading to the re-establishment of stable stratification, marked by a new surface-based inversion layer, with the possibility of the creation of a residual layer. The night profiles show variations in the possible ABL height region, which may be influenced by

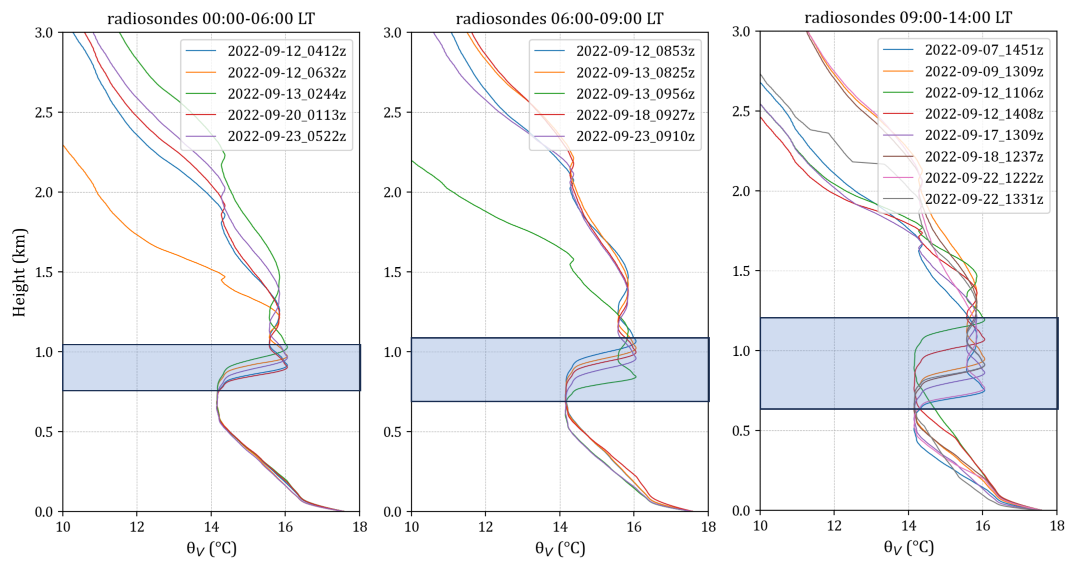

Figure 3.20: Parcel method applied on θ_v variable as measured from radiosondes launched during daytime: local time periods of 00:00-06:00 left panel, 06:00-09:00 middle panel and 09:00-14:00 right panel

the lingering effects of the afternoon sea breeze. Although the sea breeze typically weakens after sunset, its residual impact can still lead to some variability in the ABL structure during the night. The cooler, stable air that is carried inland during the afternoon may persist for several hours, affecting the height at which the ABL top is observed and introducing some spread in the profiles during the nighttime period.

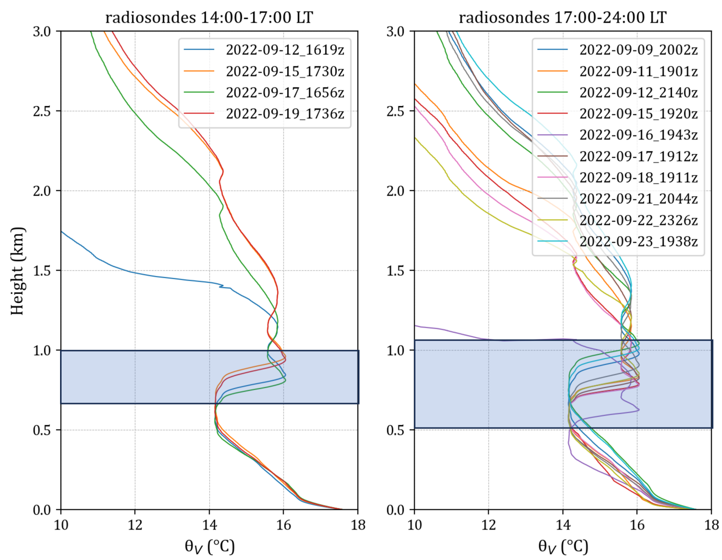

Figure 3.21: Parcel method applied on θ_v variable as measured from radiosondes launched after noon: local time periods of 14:00-17:00 left panel, and 17:00-24:00 right panel

Chapter 4

ABL in the Mediterranean: a coastal site

Abstract of Chapter 4

The objective of this chapter is the estimation of the dynamic evolution of the Planetary Boundary Layer (PBL) height, using advanced remote sensing measurements from Finokalia Station, where the Pre-TECT Campaign took place during 1-26 April 2017. PollyXT Raman Lidar and Halo Wind Doppler Lidar profiles are used to study the daily vertical evolution of the PBL. Wavelet Covariance Transform (WCT) and Threshold Method (TM) are performed on different products acquired from Lidars. According to the analysis, all methods and products are able to provide reasonable boundary-layer height estimates, each of them showing assets and barriers under certain conditions. Two cases are presented in detail, indicating the limited daytime evolution of a coastal area, the decisively role of winds speed-direction in the formation of a shallow or high boundary layer and the differences when using aerosols or turbulence as tracers for the PBL height retrieval. Comparison between the observed PBL and ECMWF model results is made, establishing the importance of actual PBL measurements, in coastal regions with complex topography.

Studying the Planetary Boundary Layer (PBL) characteristics at a coastal site by using remote sensing, can prove challenging, primarily due to the variability in wind patterns and the high moisture content typical of these regions. Unlike continental areas, the PBL in marine environments often lacks a pronounced daytime evolution (Sandu et al., 2010). However, as detailed analyzed in this chapter, it can exhibit a structured composition comprising a mixed layer (ML), a residual layer (RL), and a stable boundary layer.

This chapter focuses on the Eastern Mediterranean region, specifically Finokalia on the island of Crete, where the PreTECT campaign was conducted. Section 1 provides an overview of the PreTECT campaign and the data utilized. Section 2 shows the detailed analysis of two selected case studies, highlighting their distinct characteristics. Section 3 presents a statistical analysis based on one month of observations. The primary conclusions from this chapter are summarized in chapter 6.

4.1 The PreTECT experimental campaign

4.1.1 Finokalia Site

The PreTECT Campaign took place during April 2017, at Finokalia island of Crete, Greece, organized by the National Observatory of Athens (NOA). Finokalia [35.34°N, 25.67°E, 250m a.s.l.] (Fig. 4.1), is a coastal region in the northern coast of Crete located at the top of a hilly elevation, facing the sea within a sector 270° to 90° that present different characteristics comparing to urban sites. The location of the island, along with the atmospheric circulation patterns (Gerasopoulos et al., 2010), elaborate a rich aerosol scene on the area, originating from natural sources (marine aerosols from Aegean, dust particles from Africa) or anthropogenic activities (pollution from big regional centers like Istanbul and Heraklion). On a synoptic scale, the Eastern Mediterranean is at the crossroads of air mass outflows from European and Asian pollution sources (Bossioli et al., 2016) as well as receiving significant amounts of desert dust from Africa and the Middle East. The region is characterized by considerable variability in cloud systems, ranging from frontal and convective to cyclones (Jacobeit, 1987, Lionello and Galati, 2008, Miglietta et al., 2011). It is a climate "hot spot", exhibiting more frequent and more intense weather phenomena associated with severe winds (Etesians), floods, and dust events during the transition seasons (Marinou et al., 2021, Tombrou et al., 2015, Hoerling et al., 2012, Field and Barros, 2014, Solomos et al., 2017). Therefore, accurate PBL height is needed to correctly interpret the numerous measurements at the Finokalia site. This study contributes to the discussion of PBL evolution and height detection, comparing methods for two case studies characterized by different meteorological conditions and through month-long analysis of different methods.

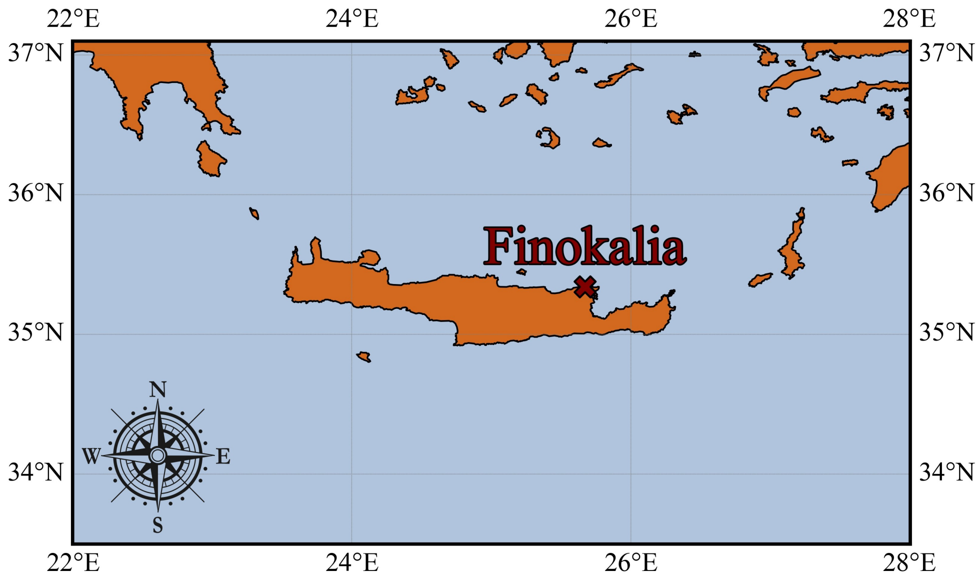

Figure 4.1: Finokalia station [35.34°N, 25.67°E, 250m a.s.l.] on the north coast of Crete.

An ensemble of active remote sensing instrument observations is used in order to study the atmospheric boundary layer characteristics at this coastal site. Observations from PollyXT Raman Lidar (Engelmann et al., 2016) and a Halo scanning Wind Doppler Lidar (Pearson et al., 2009), are processed. The brief overview of the two active remote sensing instruments operating during the PreTECT campaign is presented in chapter 2).

4.1.2 Dataset

For the case studies analyzed herein, several products are retrieved from each instrument. Range Corrected Signal (RCS), attenuated BackSCatter coefficient (BSC) and Water Vapor Mixing Ratio (WVMR) are calculated from the PollyXT Lidar, using the signal from 532 nm Near Field (NF) and 1064nm Far Field (FF) channel for the BSC product and the ratio of 387 nm and 407 nm signals for the WVMR product (Whiteman et al., 1992). WVMR profiles from PollyXT lidar are calibrated by the collocated Microwave Radiometer (MWR) (Dai et al., 2018, Foth et al., 2015). The WVMR retrievals are only available during nighttime hours, 00:00-04:00 and 18:00-24:00 UTC.

The Halo Doppler Lidar measurements were post-processed according to (Manninen et al., 2016, Manninen et al., 2018, Vakkari et al., 2019) and a SNR-threshold of 0.0075 was applied to the data. Horizontal wind speed and direction were retrieved from the conical scans (Browning and Wexler, 1968) and turbulent kinetic energy dissipation rate (TKE_{dr}) was estimated following O'Connor et al., 2010.

For the meteorological analysis of the case studies, ERA5 Re-Analysis dataset from European Centre for Medium-Range Weather Forecasts (ECMWF) is used (link). For the vertical meteorological parameters needed for the retrieval of WVMR from PollyXT Lidar, we utilize the Advanced Research Weather Research and Forecasting model version 4.2.1 (WRF-ARW) (Skamarock et al., 2008). The WRF-ARW spatial set up was at 9 × 9 km resolution domain with 600 × 370 grid points and 33 vertical levels. Simulations were initiated at 00:00 UTC on 01 April 2017 and were completed at 18:00 UTC on 30 April 2017. Finally, the atmospheric transport modeling used in this study, is based on the FLEXPART v10.4 (FLEXible PARTicle) Lagrangian dispersion model (Stohl et al., 2005, Pisso et al., 2019). The following are reproduced:
a) 7-day air masses back-trajectories prior to their arrival at 2 altitudes (0.5 and 5 km) above Finokalia ground station on 10^{th} April 2017 at 10 UTC and
b) 5-day air masses back-trajectories at 500 m above Finokalia ground station on 14^{th} April 2017 at 10:00 UTC.

A total of 50000 particles are released over the Finokalia station both in two simulations. FLEXPART was driven with 3-hourly meteorological data from the National Centers for Environmental Prediction (NCEP) Global Forecast System (GFS) analyses provided at 0.5° × 0.5° resolution and for 41 model pressure levels.

The Wavelet Covariance Transform (WCT) and the Threshold Method (TM) are applied with several modifications on the products of the campaign dataset. WCT is applied on 532nm NF RCS and WVMR profiles acquired from PollyXT Lidar and on BSC profiles from Halo Lidar. RCS and BSC are proportional to the air concentration (molecules and aerosols). TM is applied on TKE_{dr} profiles from Halo Lidar. All the product profiles used in this chapter, are 15-minutes averaged, with the exception of TKE_{dr} profiles where 1-hour median is calculated.

As explained in detail in section 3, the WCT method applied on the above mentioned products, assumes that the majority of aerosol particles are contained in the PBL, rather than in the free troposphere. Hence, a strong decrease of the signal is observable at ML top. The wavelet covariance function is calculated for every single averaged profile according to the formula of eq. 3.1. The signal (f(z)) to perform WCT, is in this case it the RCS, BSC or calibrated WVMR. A critical detail for the accurate WCT application, is the selection of an appropriate value of the dilation so as to distinguish PBL, cloud layers and aerosol layers (Baars et al., 2008). For the examined cases, sensitivity studies were performed, resulting in different dilations, an algorithm was developed to detect the maxima of the time-averaged vertical profiles for each product (more information in section 3.2). In Fig. 4.2, an example of wavelet signal profiles of 14 April 2017 02:00 UTC is presented (blue color), along with the corresponding product from PollyXT and Halo Lidar, showing the detection of the peak around 400 m. The selection of a fixed dilation of 20 Δz = 150 m, where Δz corresponds to the lidar vertical resolution 7.5 m, works well for the cases of this study.

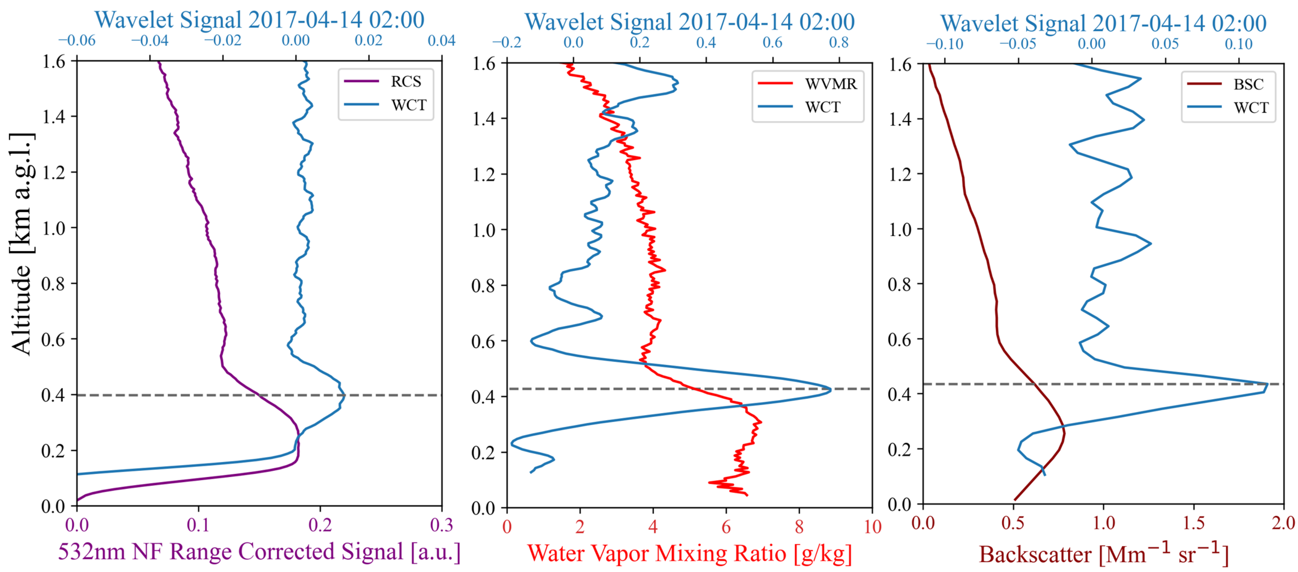

Figure 4.2: Wavelet Signal (Blue lines) from 14 April 2017 02:00 UTC, for (left) 532 nm Near Field channel Range Corrected Signal (purple line) from PollyXT Lidar, (center) Water Vapor Mixing Ratio (red line) from PollyXT Lidar and (right) Attenuated Backscatter Coefficient (brown line) from Halo Lidar.

The Threshold Method (TM) is based on the set of a condition that includes a constant threshold value. More information on this method can be found on 3.4. For the cases analyzed, MLH is determined using the threshold of $10^{-4} m^2 s{-}3$. The products from each instrument and the method that is applied in each case, are presented in Table 4.1.

4.2 Detailed Analysis of Selected Cases

Before analyzing statistics of PBL height at Finokalia during the PreTECT Campaign, two days are presented with different meteorological conditions and aerosol mixtures. Firstly, 10 April 2017 is described by the presence of clouds and aerosols and secondly 14 April

Table 4.1: Instruments-Products-Methods used in Chapter 4

Instrument	Product	Method
PollyXT Lidar	RCS	WCT
PollyXT Lidar	WVMR	WCT
Halo Wind Lidar	BSC	WCT
Halo Wind Lidar	TKE_{dr}	TM

2017, is a brighter day without clouds and significant aerosol load. In Fig. 4.3, wind conditions are illustrated. For the first case, mostly N/NW moderate winds are dominant (Fig. 4.3 left) in addition to the second case, where W winds are present up to 600 m, turning to NW above (Fig.4.3 right). The main wind flow is from the North that due to the presence of Crete island it becomes NW and W near the surface.

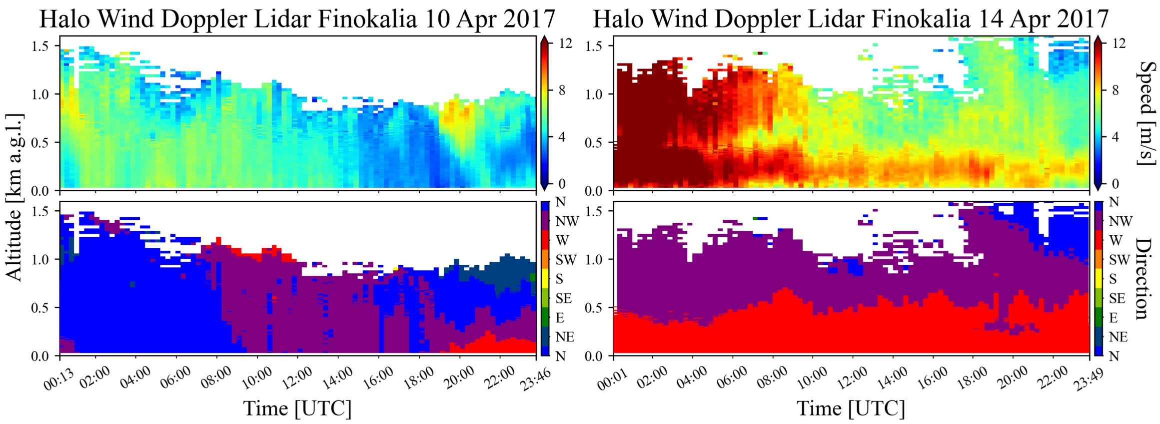

Figure 4.3: Time-Height Cross Section of top: Wind Speed and bottom: Wind Direction from Halo Wind Doppler Lidar for (left) 10 April 2017, (right) 14 April 2017. Wind directions depicted in the colorbar are classified in degrees as follows: [North: 0°, NW: 45°, W: 90°, SW: 135°, S: 180°, SE: 225°, E: 270°, NE: 315°, N: 360°].

4.2.1 Case 10 April 2017

Meteorological Analysis

The existence of a deep trough over the Black Sea, forces the atmospheric circulation in Eastern Balkans and the weather conditions in Greece on this day. The movement of the polar jet stream southwards in Europe, that started on 7 April 2017, permitted colder air masses to enter Eastern Europe and spin with the support of the associated trough system. As shown in Fig. 4.4 left, the low-pressure system is located over Black sea at 500 hPa, accompanied by the colder air mass, presented at 850 hPa with temperature 0°C (Fig. 4.4 middle).

As a result, the weather in Crete, Greece is characterized by low temperatures, favoring cloud formation. The wind field in Aegean Sea is mostly N/NE, stronger in the central and southern parts reaching up to 12 m/s (6 Beaufort-fresh to strong breeze, Fig. 4.4 right).

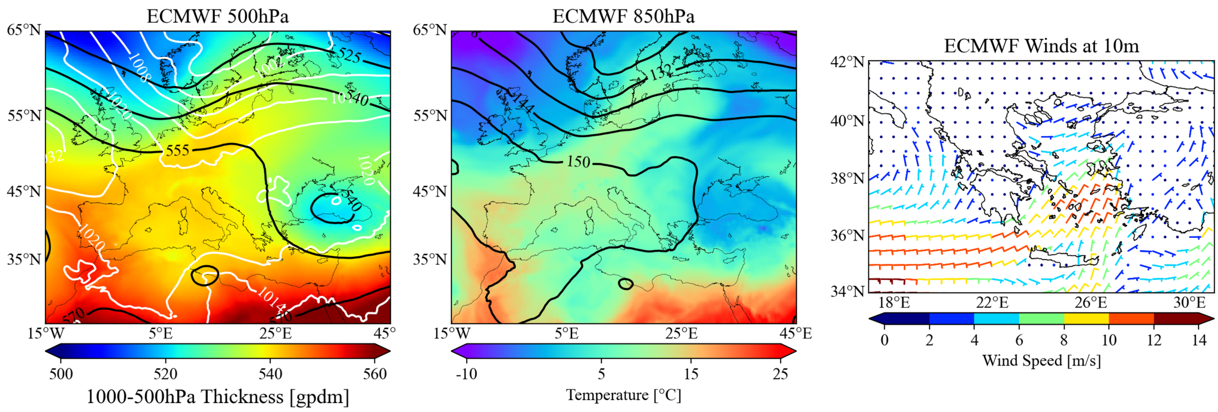

Figure 4.4: ECMWF Reanalysis Data for 10 April 2017, 06:00UTC (a) 500 hPa Geopotential Height (black lines), MSLP (white lines), 1000-500 hPa Thickness, (b) 850 hPa Geopotential Height (black lines), 850 hPa Temperature, (c) 10 m Wind Speed and Direction.

Cloud and aerosol conditions

During 10 April 2017, sparse high level (8-10 km) and mid-level (5-8 km) clouds are observed above Finokalia Station, as shown in Fig. 4.5a, depicting the attenuated BSC coefficient at 1064 nm (upper panel) and the volume depolarization ratio (bottom panel) from PollyXT Lidar. Low level (0-2 km) clouds also form inside and above the PBL. The thin aerosol layer observed at 5-6 km presents depolarization ratio of 15-30% (Fig.4.5b) and according to FLEXPART model, originate from NW Africa (green line Fig. 4.5c-d) which suggest a mixture of dust and pollution aerosols. Moreover, marine and pollution aerosols with volume depolarization ratio 5-10% exist up to 700 m, arriving from Balkans and the Aegean Sea (blue line Fig.4.5c-d).

PBL diurnal evolution on 10 April 2017

Winds from the northern sector (NNW and NNE) are blowing during whole day, as shown in Fig.4.3, stronger from 00:00 to 14:00 UTC (up to 8m/s), comparing to the afternoon. A jet is present after 18:00 UTC, causing changes in wind speed and direction: west-northwesterly (W/NW) winds reach up to 300 m, switching to north-northeasterly (N/NE) above 700m, playing an important role to the nighttime PBL structure.

PBL height is retrieved by applying WCT on the RCS from the 532 nm Near Field channel (Fig. 4.6 a – brown circles) and the WVMR (Fig. 4.6 c – green triangles) from PollyXT Lidar, as well as on the attenuated BSC from Halo Wind Lidar (Fig. 4.6 b – blue circles), resulting to PBL_{RCS}, PBL_{WVMR}, PBL_{BSC} respectively. The TM is applied on the TKE_{dr}, provided by Halo (Fig. 4.6 d – red stars), resulting to MLH_{TKE} retrievals. In the beginning of the day (00:00-04:00 UTC), PBL_{BSC}, PBL_{WVMR} and PBL_{BSC}, reach up to 1 km and then drop gradually to 400 m until 03:00 UTC, whereas MLH_{TKE}, reaches 800 m and then drops to 300 m. During 03:00-11:00 UTC, PBL (where available) presents a rising tendency, from 400 m to 1 km, corresponding to the daytime evolution. After 11:00 UTC, the PBL_{RCS} and PBL_{BSC} is descending from 1 km to 600 m until 18:00 UTC, presenting some local peaks in the meantime. MLH_{TKE} follows that descending

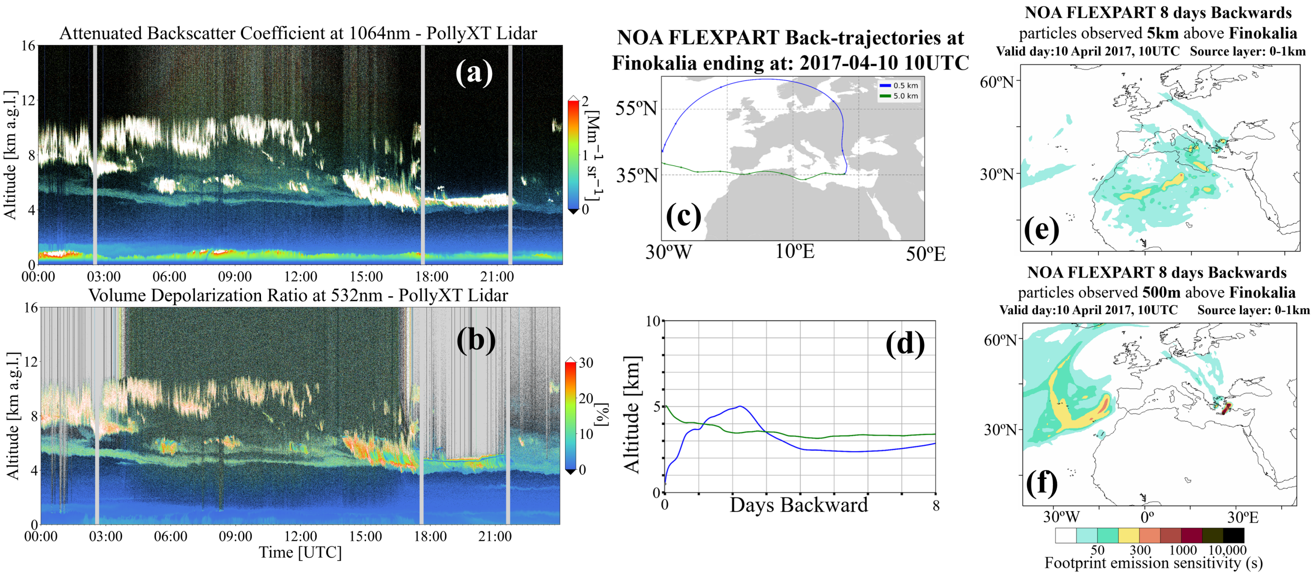

Figure 4.5: (a-b) PollyXT Lidar parameters for 10 April 2017 00:00-24:00 UTC: Attenuated Backscatter Coefficient at 1064nm channel in arbitrary units (a.u.); Volume Depolarization Ratio in percentage units, (c) Air mass backward trajectories, based on FLEXPART simula-tions, ending at 0.5 (blue) and 5 (green) km above the Finokalia station on 10th April 2017 at 10 UTC (d) Altitudes, above ground level, of the air masses on their route prior their arrival over the ground station (e-f) FLEXPART Source–Receptor Relationships (s) for air masses originating from 0–1km a.s.l. arriving above Finokalia at: 0.5 and 5 km accordingly on 10th April 2017, 10:00 UTC.

from 1 km to 500 m between 10:00-17:00 UTC. After 18:00 UTC, an aerosol layer with top ranging from 500 to 800 m is observed from WCT on RCS, WVMR and BSC products.

In Fig. 4.7, the PBL height and MLH retrievals for 10 April 2017 are compared, showing strong agreement for most of the day. All approaches capture a high nocturnal mixing layer between 00:00-02:00 UTC. This is probably the result of mechanical turbulence induced by the northerly winds, meeting the coastline. Aerosols and water vapor are transported above the site (as explained in 4.2.1), by the same flow and track the mixing layer indicated by TKE_{dr}. After 02:00 UTC, the descending tendency of PBL is captured from all products, as well as the daytime evolution that takes place after 04:00 UTC, when the sun rises and thermal turbulence starts to form. During daytime (5:00-16:00 UTC), PBL_{RCS}, PBL_{BSC} and MLH_{TKE}, present accordance in capturing a well-mixed layer reaching 1000 m, which is probably a result of both mechanical and thermal turbulence. After 18:00 UTC, PBL_{RCS}, PBL_{BSC} and PBL_{WVMR} track a layer around 750 m, but MLH_{TKE} is significantly dropping. This remarkable difference arises from the fact that WCT on aerosol tracers, detect a layer which is rich in aerosols and probably coincides with the residual layer, without following the above mentioned MLH_{TKE} drop (similar to e.g. Schween et al. (2014)). MLH_{TKE} conceives a very stable nocturnal layer, and PBL from the other products reflects a layer, that is not affected by turbulent transport of surface-related properties and hence does not fall within the nocturnal boundary layer. Also, the formation of a low level jet within the lowest 100 m a.g.l. after 21:00 UTC (Fig.

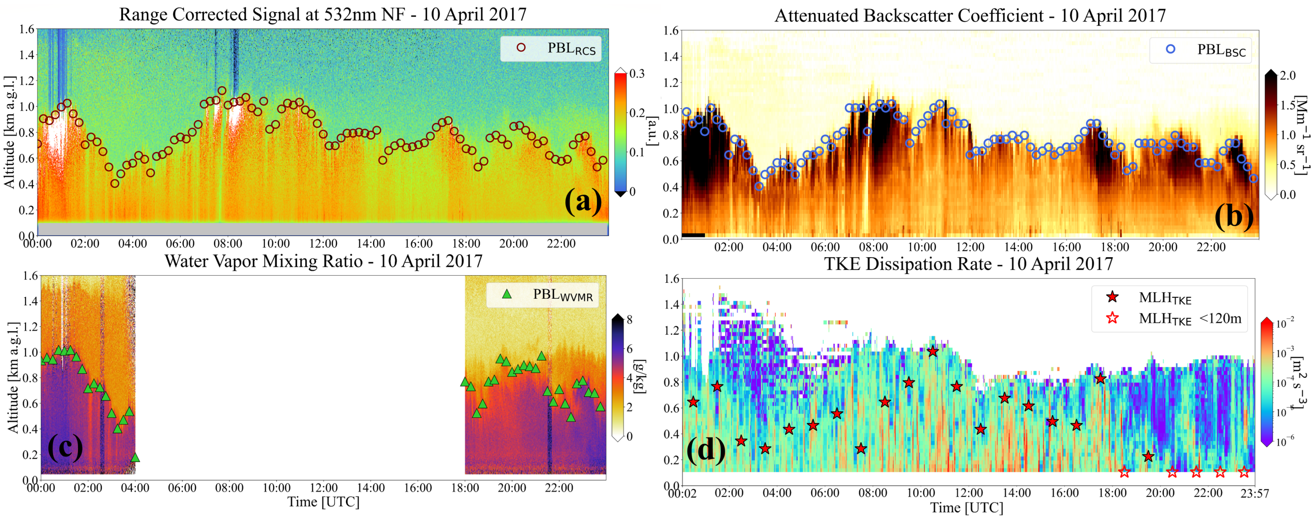

Figure 4.6: PollyXT Lidar (a,c) and Halo Wind Doppler Lidar (b,d) products for 10 April 2017: (a) Range Corrected Signal (RCS) at 532nm NF channel (Grey color at the bottom of the Figure, identifies the incomplete overlap of PollyXT Lidar) – Brown circles: PBL height from Wavelet Covariance Transform (WCT) on RCS (PBL_{RCS}); (b) Attenuated Backscatter Coefficient (BSC) – Blue circles: PBL height from WCT on BSC (PBL_{BSC}); (c) Water Vapor Mixing Ratio (WVMR) – Green Triangles: PBL height from WCT on WVMR (PBL_{WVMR}); (d) Turbulent Kinetic Energy dissipation rate (TKE_{dr}) – Black stars: PBL Height from Threshold Method (TM) on TKE_{dr} (MLH_{TKE}).

4.5 a) indicates highly stable conditions. The lower layer is characterized by west (W) winds and the upper layer is affected by a north (N) jet form 18:00 UTC onwards. The layer near the surface is directly affected from the land and becomes cooler during the night, while above 300 m the wind flow is from the sea (warmer) and contributes to the continuous transfer of aerosol load and water vapor above Finokalia, used as tracers from the WCT method.

The PBL height estimated by the ECMWF model, is presented in Fig. 4.7 for two points that belong in different grid: the purple diamond ($PBL_{ECMWF_{SEA}}$) belongs to a grid simulated over sea and the orange diamond ($PBL_{ECMWF_{LAND}}$) belongs to a grid simulated over land. Finokalia Station, is located between the two model bins. During all day, there is good agreement between $PBL_{ECMWF_{SEA}}$ and PBL height measured by the instruments. $PBL_{ECMWF_{SEA}}$ does not present a sharp daytime evolution, in addition to $PBL_{ECMWF_{LAND}}$ that ascents between 04:00-10:00 UTC and descents after 14:00 UTC. Nighttime (00:00-04:00 UTC, 18:00-24:00 UTC) measurements of PBL height are in sufficient agreement with the $PBL_{ECMWF_{SEA}}$. On the other hand, daytime measurements are found to agree mostly with the rising tendency that $PBL_{ECMWF_{LAND}}$ presents (04:00-08:00 UTC), but there is a discordance after 16:00 UTC, where $PBL_{ECMWF_{LAND}}$ drops very smoothly. MLH_{TKE}, also captures this drop, since the stable nocturnal layer is formed.

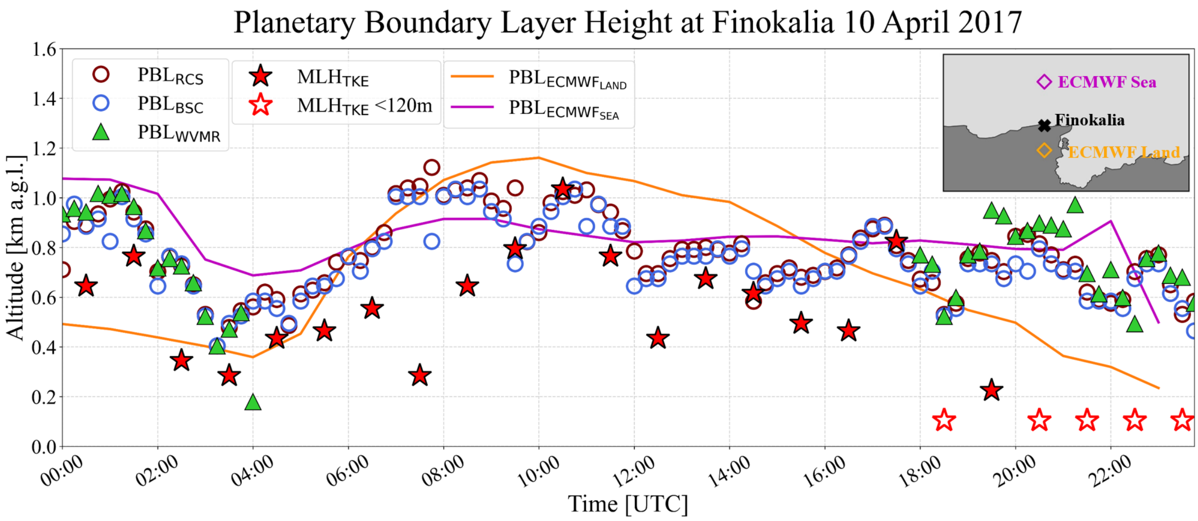

Figure 4.7: 10 April 2017 PBL height diurnal evolution from WCT applied on 532nm NF RCS (brown circles - PBL_{RCS}), WVMR from PollyXT Lidar (green triangles - PBL_{WVMR}), BSC from Halo Lidar (blue circles - PBL_{BSC}) and TM applied on TKE_{dr} from Halo Lidar (red stars - MLH_{TKE}). Top right: map with Finokalia's location between ECMWF Land bin (orange diamond) and ECMWF Sea bin (purple diamond).

4.2.2 Case 14 April 2017

Meteorological Analysis

On 14 April 2017, zonal flow is restored above Europe, with the polar jet stream limited in the northern paths (500 hPa Fig. 4.8a). Warmer air masses are approaching the Mediterranean Sea with temperatures ranging 10-15°C at the 850 hPa level (Fig. 4.8b). Under these atmospheric conditions, the weather in Crete is sunny and warmer. The W/NW wind field that dominates the southern parts of the Aegean (Fig. 4.8c), does not exceed 12 m/s during all day.

Cloud and aerosol conditions

Above Finokalia station, during 14 April 2017, skies are cloudless all day, according to the attenuated BSC coefficient derived from PollyXT Lidar (Fig. 4.9a). The aerosol concentration is very low; probably a mixture of marine and pollution particles with particle linear de-polarization ratio less than 10% (Fig. 4.9b), originating from NE (Fig. 4.9c-d-e), are present in the lower levels.

PBL diurnal evolution on 14 April 2017

The second case examined, 14 April 2017, is a day with much stronger winds, especially at the beginning of the day, in comparison with 10 April 2017. At the lower levels (below 500 m), the W wind field prevails, with speed exceeding 15 m/s, in addition to the higher levels (above 500 m), affected by N/NW winds (Fig 4.3 b). After 08:00 UTC, winds above 500 m decrease significantly, but the vertical difference in wind direction is maintained

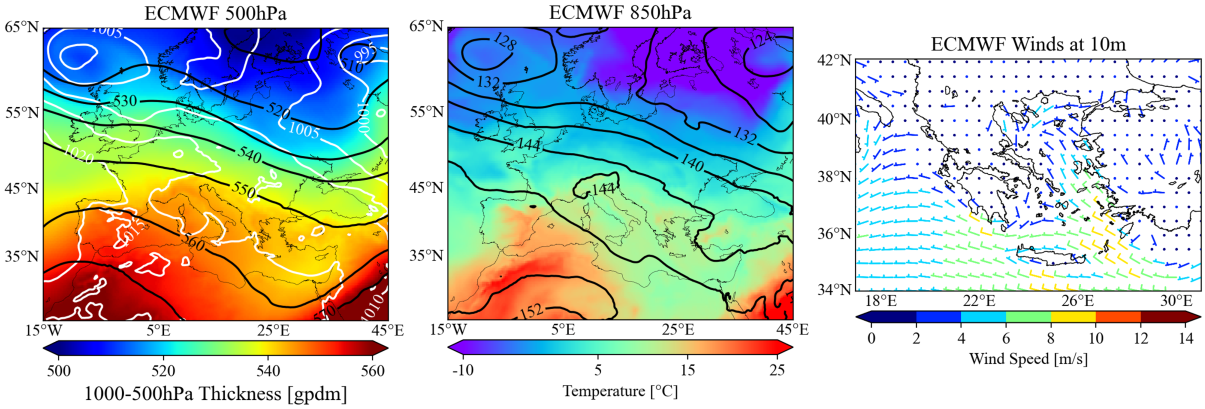

Figure 4.8: ECMWF Reanalysis Data for 14 April 2017, (a) 18:00 UTC 500 hPa Geopotential Height (black lines), MSLP (white lines), 1000-500hPa Thickness, (b) 18:00 UTC 850 hPa Geopotential Height (black lines), 850 hPa Temperature, (c) 06:00 UTC 10m Wind Speed and Direction (d) 06:00 UTC 2m Temperature, MSLP (white lines).

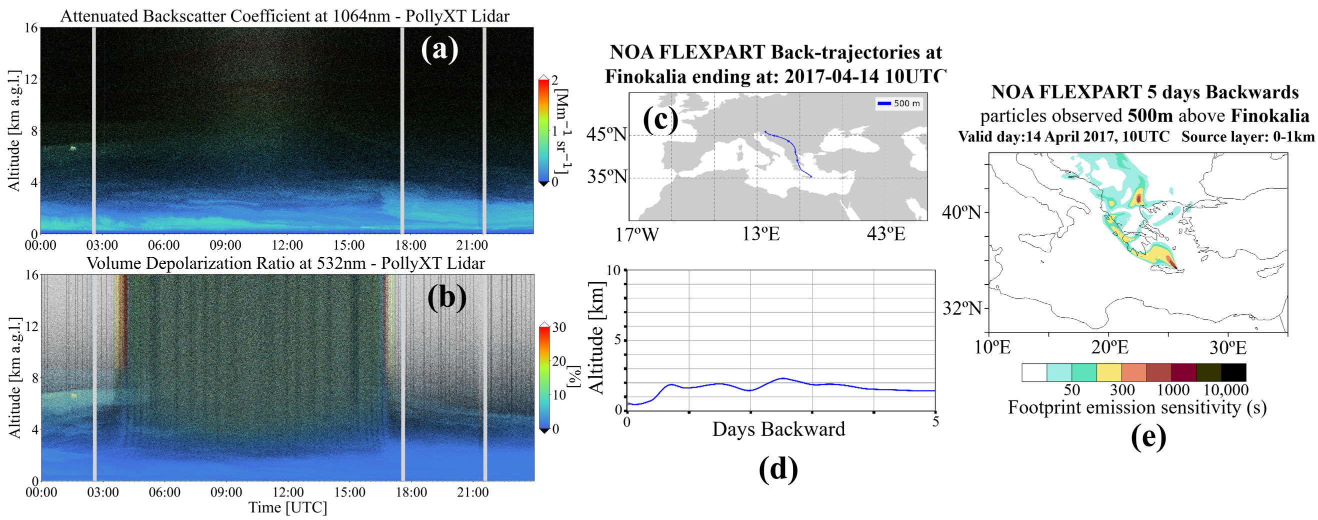

Figure 4.9: PollyXT Lidar parameters for 14 April 2017 00:00-24:00 UTC: Attenuated Backscatter Coefficient at 1064 nm channel in arbitrary units (a.u.); Volume Depolarization Ratio in percentage units, (c-d) Air mass backward trajectories, based on FLEXPART simulations, ending at 500 m above the Finokalia station on 14th April 2017 at 10 UTC; Altitudes, above ground level, of the air masses on their route prior their arrival over the ground station, (e) FLEXPART Source–Receptor Relationships (s) for air masses originating from 0–1 km a.s.l. arriving above Finokalia at 500 m on 14th April 2017, 10 UTC.

throughout the day. A low level jet is present throughout the day with peak height at approx. 200 m a.g.l. Overall, the vertical profile of horizontal wind indicates persistent layering, which suggests different characteristics of the air masses at surface and above 500 m a.g.l.

Before sunrise (00:00-04:00 UTC), WCT on RCS, BSC and WVMR products, locate a layer around 400 m (Fig. 4.10a,b,c), while MLH_{TKE} is captured between 200 and 350 m (Fig. 4.10d). After 04:00 UTC, daytime evolution takes place and the PBL starts rising as captured by RCS and BSC products and then drops again after 06:00 UTC to 200 m with small fluctuations. TKE_{dr} from Halo, records a very turbulent layer below 400 m during all day, likely caused by mechanical turbulence generated by the W winds (Fig. 4.3b). During the daytime (05:00 to 14:00 UTC), there is also another turbulent layer present between 400 m and 800 m a.g.l., but this layer seems to be unconnected to the surface. Moreover, the lower detected layer is rich in water vapor, reaching around 400 m before sunrise and 200 m after sunset.

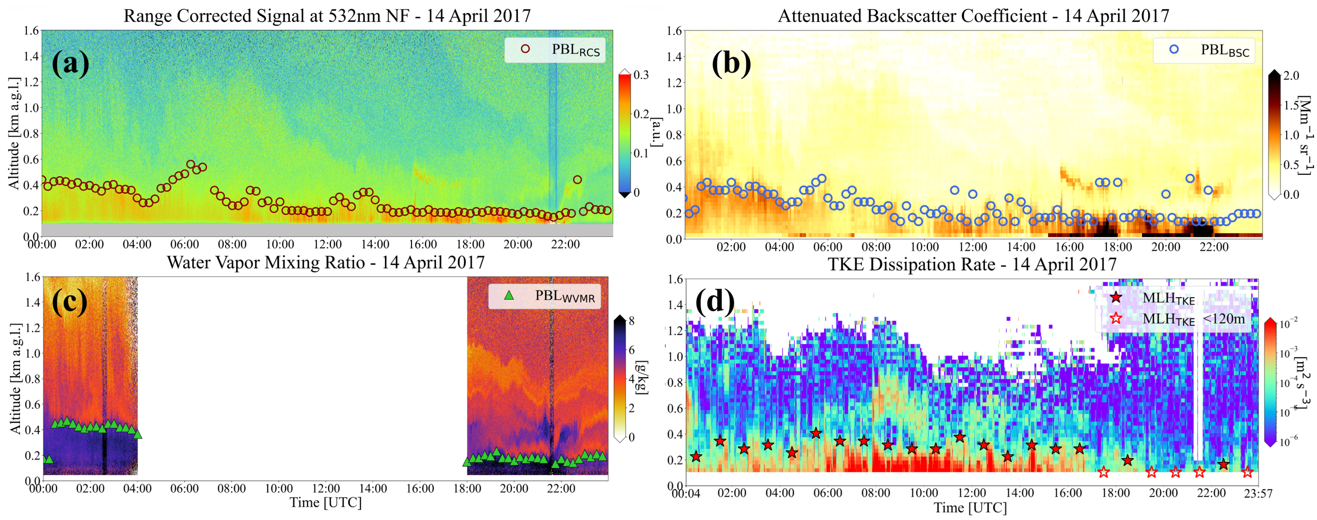

Figure 4.10: PollyXT Lidar (a,c) and Halo Wind Doppler Lidar (b,d) products for 14 April 2017: (a) Range Corrected Signal (RCS) at 532nm NF channel (Grey color at the bottom of the Figure, identifies the incomplete overlap of PollyXT Lidar) – Brown circles: PBL height from Wavelet Covariance Transform (WCT) on RCS (PBL_{RCS}); (b) Attenuated Backscatter Coefficient (BSC) – Blue circles: PBL height from WCT on BSC (PBL_{BSC}); (c) Water Vapor Mixing Ratio (WVMR) – Green Triangles: PBL height from WCT on WVMR (PBL_{WVMR}); (d) Turbulent Kinetic Energy dissipation rate (TKE_{dr}) – Black stars: PBL Height from Threshold Method (TM) on TKE_{dr} (MLH_{TKE}).

Examining all the results together (Fig. 4.11), indicates a significant accordance between all methods and retrievals during nighttime (before 04:00 UTC and after 18:00 UTC) with a slightly lower MLH_{TKE}. When the sun rises (after 04:00 UTC), weak daytime evolution takes place, with the PBL height and MLH_{TKE} captured by the two Lidars, being in sufficient agreement. Some profiles of Halo BSC and PollyXT RCS, capture a layer around 400 m after 16:00 UTC. This could happen because the northern winds that are imposed from the synoptic system, are modified by the surface due to the presence (obstacle) of Crete and slightly switch to western direction (Fig. 4.3). As a result, lifting marine and pollution aerosols on the site, are detected by WCT method and causing the outliers of PBL_{RCS}, PBL_{BSC}.

Furthermore, comparing our results with the ECMWF retrievals, there is a slight underestimation of $PBL_{ECMWF_{LAND}}$ at the beginning of the day (00:00-04:00 UTC) and good agreement at the end (18:00 UTC onwards). The underestimation occurs because lidars detect aerosols trapped in the boundary layer, whereas the model predicts a lower nocturnal layer above land. On the other hand, MLH_{TKE} is closer to the $PBL_{ECMWF_{LAND}}$ at the beginning of the day, as it represents a lower turbulent layer. $PBL_{ECMWF_{SEA}}$ presents the same tendency as PBL_{WVMR}, PBL_{RCS} and PBL_{BSC} during 00:00-04:00 UTC, but deviates after 16:00 UTC, maintaining the values of the nocturnal layer (around 400 m). This overestimation of $PBL_{ECMWF_{SEA}}$ is closer to the outliers of PBL_{BSC} and PBL_{RCS}. Nevertheless, a substantial difference arises from 06:00 to 16:00 UTC, with the model's overestimated $PBL_{ECMWF_{LAND}}$ during the convective daytime period. As expected, $PBL_{ECMWF_{SEA}}$ is not developing as quickly and is in better accordance with the measurements, still overestimating PBL during 07:00-16:00 UTC. This divergence between $PBL_{ECMWF_{SEA}}$, $PBL_{ECMWF_{LAND}}$ and the measurements, especially during daytime, is attributed at the complexes induced by Finokalia's location. The station is at the edge of a steep cliff between the land and sea, but the model conceives a land surface with high convective activity in case of $PBL_{ECMWF_{LAND}}$ and a maritime area in which the marine atmospheric boundary layer forms in case of $PBL_{ECMWF_{SEA}}$. The influence of changes in surface roughness at Finokalia station, occurs at a scale that is too fine for the model, hence the above mentioned differences arise.

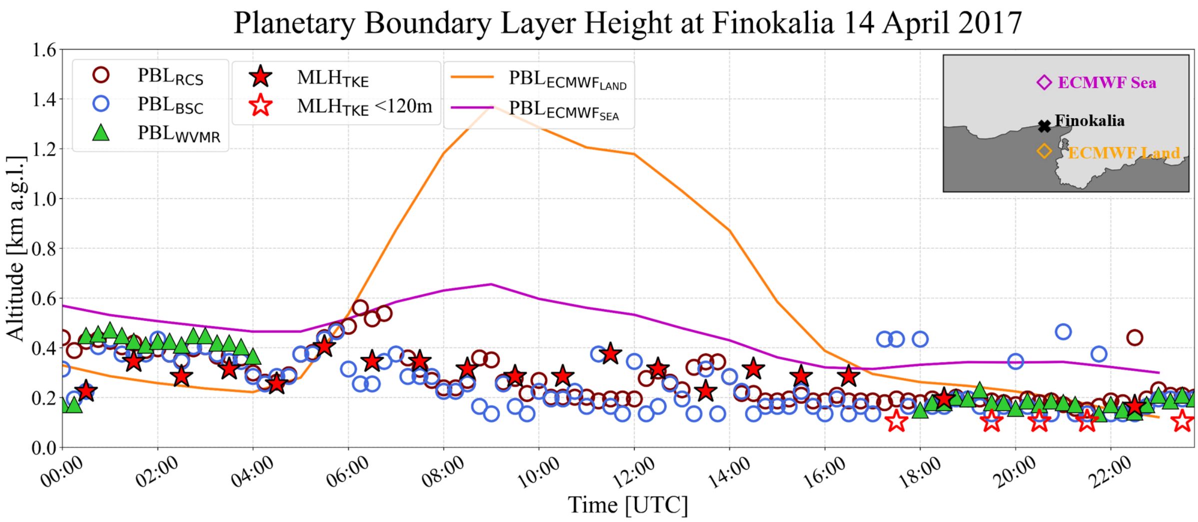

Figure 4.11: 14 April 2017 PBL height diurnal evolution from WCT applied on 532 nm NF RCS (brown circles - PBL_{RCS}), WVMR from PollyXT Lidar (green triangles - PBL_{WVMR}), BSC from Halo Lidar (blue circles - PBL_{BSC}) and TM applied on TKE_{dr} from Halo Lidar (red stars - MLH_{TKE}). Top right: map with Finokalia's location between ECMWF Land bin (orange diamond) and ECMWF Sea bin (purple diamond).

4.3 Statistical Analysis

An overview of wind speed and direction during 1-26 April at Finokalia, is presented in Fig. 4.12b-c, indicating variable meteorological conditions and aerosol transportation. In Fig 4.12a, attenuated backscatter coefficient at 532 nm is displayed, along with the PBL_{RCS}. White parts of the plot, signify the presence of low clouds and black parts

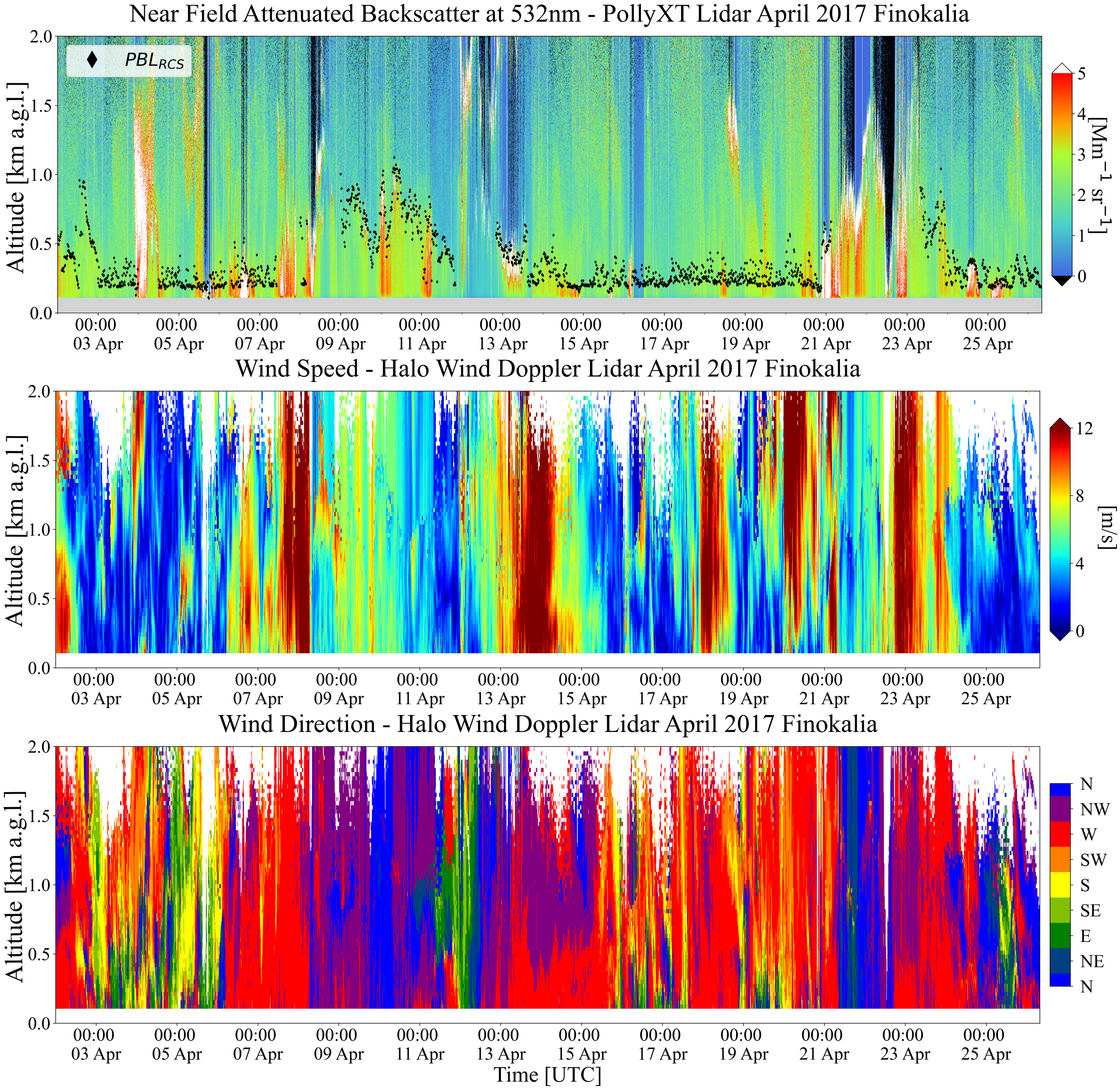

Figure 4.12: Period 1-26 April 2017 (a): Attenuated Backscatter Coefficient at 532 nm NF channel of PollyXT Lidar – PBL height retrieved by WCT on RCS (Black Diamonds), Grey color at the bottom of the Figure, identifies the incomplete overlap of PollyXT Lidar for 532 nm NF channel, (b): Wind Speed (m/s) from Halo Wind Doppler Lidar and (c): Wind Direction from Halo Wind Doppler Lidar.

stand for the attenuated signal above clouds. Time periods with low level clouds were excluded from PBL retrievals. No sharp daytime evolution of PBL is observed and its height varies between 200 and 1000 m approximately. It is also shown that when N winds are present vertically (1-3, 9-12 April), PBL is higher. NW winds in the lower levels, favor a shallower PBL, (6-8, 13-16 April) and winds from eastern and southern sector, favor the cloud formation (3-6, 12, 21-23 April).

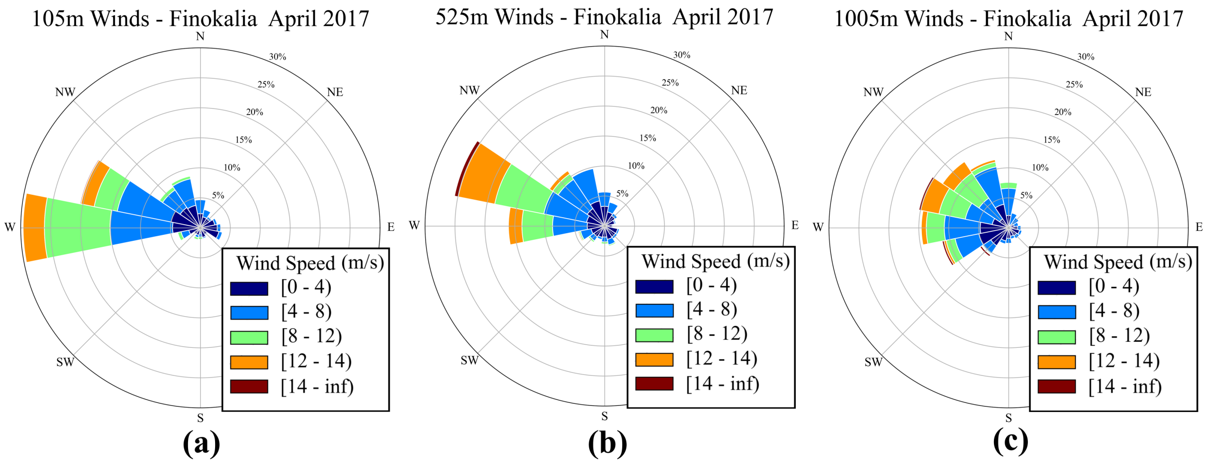

Figure 4.13: Wind Rose from Halo Wind Doppler Lidar during 1-26 April 2017 for (a) 105 m level, (b) 525 m level and (c) 1005 m level above ground.

Almost 30% of wind measurements of the campaign on the lower levels (105m) come from W, as shown in the wind rose of Figure 4.13a. At 525 m, the dominating direction slightly shifts to NW (Fig. 4.13b) and at 1005 m, there is fluctuation of winds from south-western to northern sector(Fig. 4.13c). This vertical change of wind direction between 105 m and 525 m, is also observed at the second examined case (14 April), where the PBL was very shallow and did not exceed 600 m. The domination of W winds at 105 m and the vertical shift at the first 500 m above ground level, suggest strong layering in the lower levels. More specifically, in Figure 4.14, the 2-hour mean PBL height is calculated for each product: there is no strong daytime evolution and the mean PBL does not exceed 400 m, demonstrating the low layers dominance in Finokalia station. During 04:00-08:00 and 16:00-18:00 UTC, MLH_{TKE} present larger variability comparing to the other 2-hour averages. PBL_{RCS} and PBL_{BSC}, present the highest deviation at 12:00-14:00 UTC, in addition to the smaller deviations during the rest of the 24 hours. The nighttime PBL is overestimated by $PBL_{ECMWF_{SEA}}$ and underestimated by $PBL_{ECMWF_{LAND}}$, while both overestimate the observed daytime PBL.

Mean Bias Error (MBE), standard deviation (σ) and coefficient of determination (R^2) are calculated for the differences between PBL retrievals from different products for 1-26 April 2017 (Fig. 4.15). The absolute value of MBE ranges from 0.2 m to 43.9 m, but only 2 out of 9 comparisons exceed 20 m, which given the resolution of PollyXT (7.5 m) and Halo (30 m) Lidar, can be characterized as reliable MBE. Least-squares regression is used to derive the linear fit between the 15 min PBL height estimates. As observed, there is reasonably good correlation PBL_{WVMR} - PBL_{RCS}, PBL_{BSC} - PBL_{RCS} and PBL_{BSC} - PBL_{WVMR} ($R^2 = 0.92$, $R^2 = 0.92$, $R^2 = 0.9$ respectively) for nighttime measurements and PBL_{BSC} - PBL_{RCS} ($R^2 = 0.93$) for daytime measurements during 1-26 April. Cases where TKE_{dr} indicates $MLH_{TKE} < 120$ m , were replaced with $MLH_{TKE} = 60m$, corresponding to half the "lower detection limit" of the instrument, in order to avoid positive or negative biases by excluding or zeroing respectively. Hence, strong deviations occurred in the comparisons that included PBL retrieved from TKE_{dr} (MLH_{TKE} - PBL_{BSC}, MLH_{TKE} - PBL_{RCS}, MLH_{TKE} - PBL_{WVMR}), with standard deviation exceeding $\sigma = 223$. This is expected, given the different nature of direct observations

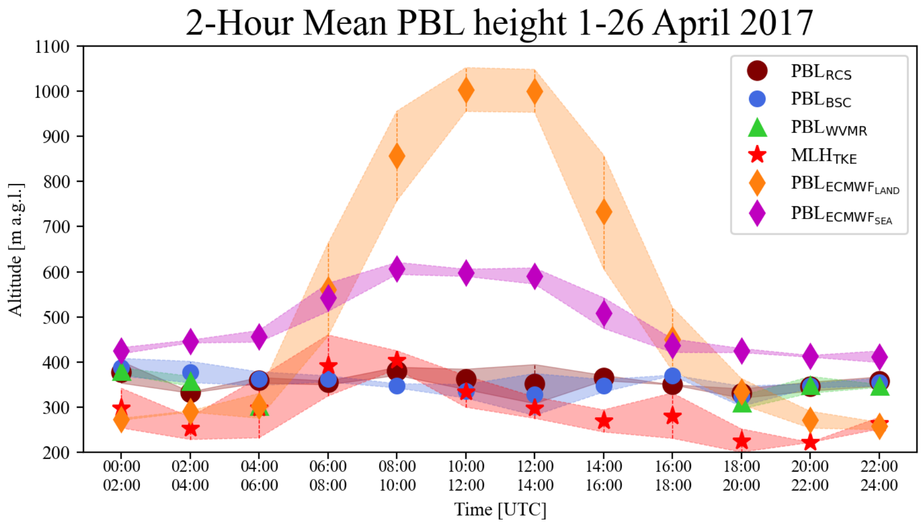

Figure 4.14: 1-26 Mean PBL height calculated every 2 hours from WCT on RCS (brown circles), BSC (blue circles), WVMR (green circles), TM on TKE_{dr} (red stars) and ECMWF land bin (orange diamonds) and sea bin (purple diamonds) as described in figures 4.7 and 4.11. Standard deviations are displayed with the same color shading for each product.

of turbulence and tracers of turbulent mixing as well as previous observations (Schween et al., 2014). In addition to this, the differences of PBL_{WVMR} - PBL_{RCS} (σ = 94.7), PBL_{BSC} - PBL_{RCS} (σ = 85.7), PBL_{BSC} - PBL_{WVMR} (σ = 101) during nighttime and from PBL_{BSC} - PBL_{RCS} (σ = 87.4) during daytime, are described by smaller standard deviation.

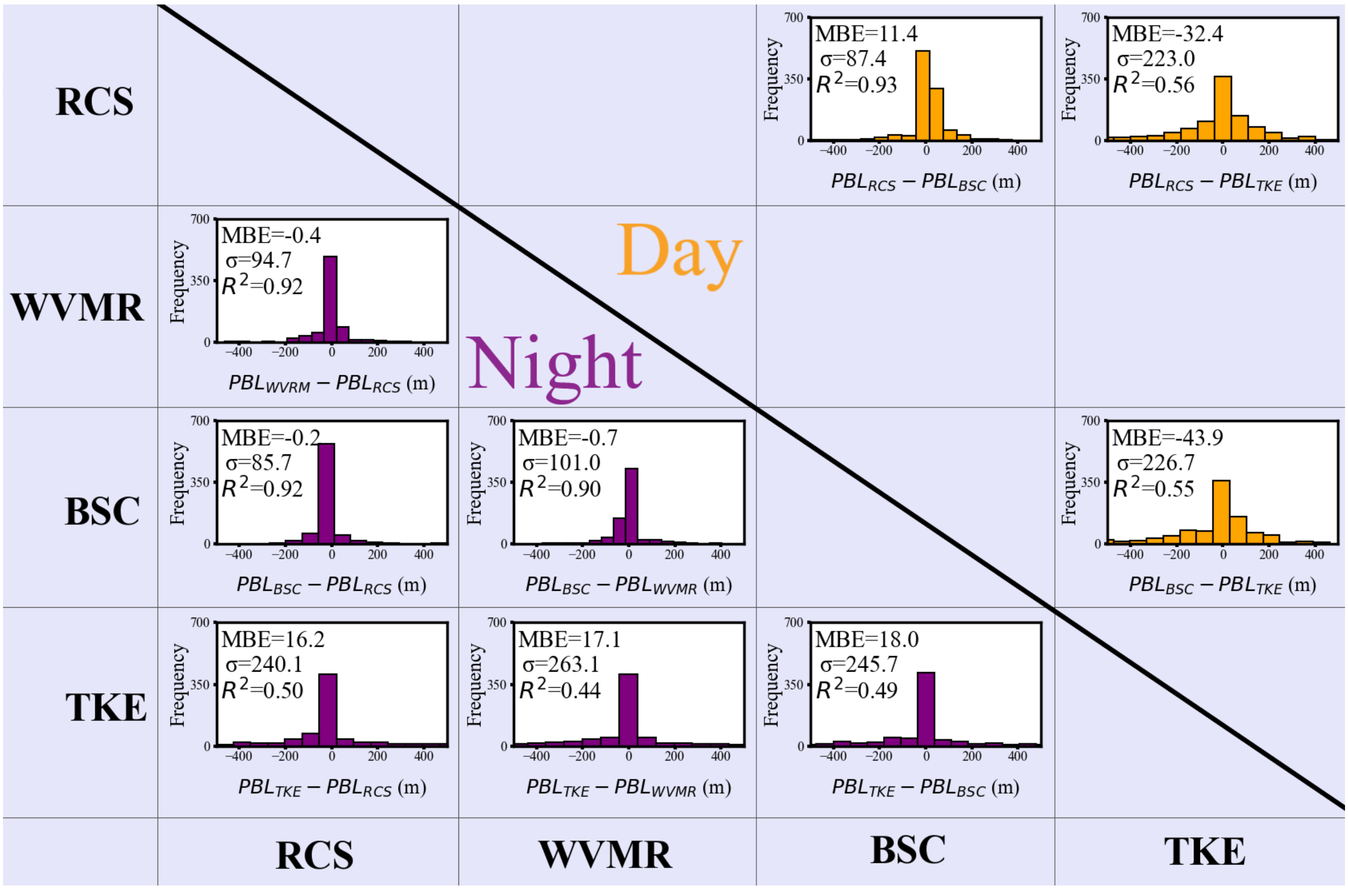

Figure 4.15: Statistical analysis of the differences between products and methods for 1-26 April 2017, separated in day and night periods.

Chapter 5

ABL in the Atlantic: the desert dust impact

Abstract of Chapter 5

This chapter investigates the dynamics of the atmospheric Boundary Layer (BL) over the Atlantic Ocean, with a focus on the region surrounding Cabo Verde during the Joint Aeolus Tropical Atlantic Campaign (JATAC) and the ASKOS experiment, using a combination of ground-based PollyXT and Doppler lidars, satellite lidar data from Cloud-Aerosol Lidar and Infrared Pathfinder Satellite Observations (CALIPSO), radiosondes, and the model outputs of the Integrated Forecasting System (IFS) of the European Centre for Medium-Range Weather Forecasts (ECMWF). The comparison of CALIPSO lidar results with ECMWF/IFS reanalysis for 2012-2022, revealed strong correlations for BL top over open ocean regions but weaker relation over dust-affected areas closer to the African continent. In these regions, space lidar indicated lower BL tops during daytime than those estimated by ECMWF/IFS. Observations in Cabo Verde highlight distinctive Marine Atmospheric Boundary Layer (MABL) characteristics, such as limited diurnal evolution, but also show the potential for BL heights to reach up to 1 km, driven by factors like strong winds that increase mechanical turbulence. Additionally, the challenges in estimating the BL height using lidar-derived aerosol mixing height versus profiling of meteorological parameters acquired from radiosondes are illustrated, examining cases with strong and weaker inversions that affect the vertical mixing and the penetration of dust particles within the BL. The findings underline the need for further improvements in the ECMWF/IFS reanalysis model towards capturing the complex interactions between marine and dust-laden air masses over the Atlantic, which are essential for constraining the dynamic processes in BL and aerosol-cloud interactions.

The Boundary Layer (BL) over the Atlantic Ocean is strongly influenced by large-scale atmospheric circulation, surface conditions, and aerosol presences. In the tropical Atlantic, one of the dominant aerosol sources is mineral dust transported from the Sahara Desert. As discussed in section 2.2.3, this dust significantly impacts the radiative balance, thermodynamic structure, and turbulence characteristics of the ABL. Understanding these interactions is crucial for improving the characterization of the BL's vertical structure and developing more robust methods for identifying its top.

In this chapter, we focus on the tropical Atlantic, with particular emphasis on the BL conditions in Cabo Verde. This region, located in the eastern tropical Atlantic, is frequently affected by Saharan dust outbreaks. By using ground-based and satellite lidar along with radiosonde measurements, we analyze how dust modifies key boundary layer properties, such as temperature stratification, humidity, and turbulence. The primary conclusions from this chapter are summarized in chapter 6.

5.1 The ASKOS experimental Campaign

This chapter utilizes data from the ASKOS Campaign (Marinou et al., 2023), which is the ground-based component of the Joint Aeolus Tropical Atlantic Campaign (JATAC) organised by the European Space Agency (ESA). ASKOS took place at the Ocean Science Centre Mindelo (OSCM), at the island of São Vicente, Cabo Verde, during 2021-2022.

For this analysis, we use the comprehensive ASKOS dataset that, among others, includes lidar observations and radiosonde datasets that are crucial for understanding atmospheric dynamics in the region. More specifically, radiosonde profiles, ground-based PollyXT lidar measurements as well the LIVAS (LIdar climatology of Vertical Aerosol Structure for space-based lidar simulation studies) dataset (Amiridis et al., 2015) of CALIPSO mission are examined. Additionally, the measurements-derived BL is compared to the ERA5 Re-Analysis dataset from European Centre for Medium-Range Weather Forecasts (ECMWF), at $0.25° \times 0.25°$ resolution with 137 levels (Vogelezang and Holtslag, 1996). Finally, Hybrid Single-Particle Lagrangian Integrated Trajectory (HYSPLIT) is employed to analyze the backward trajectories of air masses arriving at the site of the ASKOS Campaign, Mindelo, Cabo Verde. This model allows for the tracking of air parcels over time, providing valuable information about the origins of the air parcels and their potential interactions with dust and other atmospheric constituents (Rolph et al., 2017). By identifying these pathways, a clearer understanding of the sources and transport mechanisms of the atmospheric conditions at Cabo Verde can be established.

To detect the BL heights within the lidar measurements of ASKOS, the WCT and the Gradient Method are applied (Brooks, 2003; Li et al., 2021) on the backscatter coefficient profiles of the CALIOP and ground-based PollyXT lidar for the channels of 532 and 1064 nm respectively (see also Chapter 3). For the radiosonde data, layer detection is achieved with the gradient method. Sometimes detecting the BL top relies on visual inspection to accurately locate the inversion cap, particularly when automated methods fail to capture subtle features. Figure 5.1 presents example measurements from the ASKOS Campaign, which are used in this section. Specifically, profiles of backscatter coefficient at 1064 nm from ground-based PollyXT (left), of Relative Humidity (RH) from radiosonde (middle) and backscatter coefficient at 532 nm from CALIPSO satellite lidar (right) are shown. The grey lines represent the method for detecting BL top, namely WCT method for PollyXT Lidar and Gradient method for the rest two. A local maximum of the wavelet profile for WCT method, and a local minimum of the gradient for the gradient method, represent steep reduction in the investigated signal (red dashed lines).

Several significant challenges arise when studying the BL with lidars (both ground-

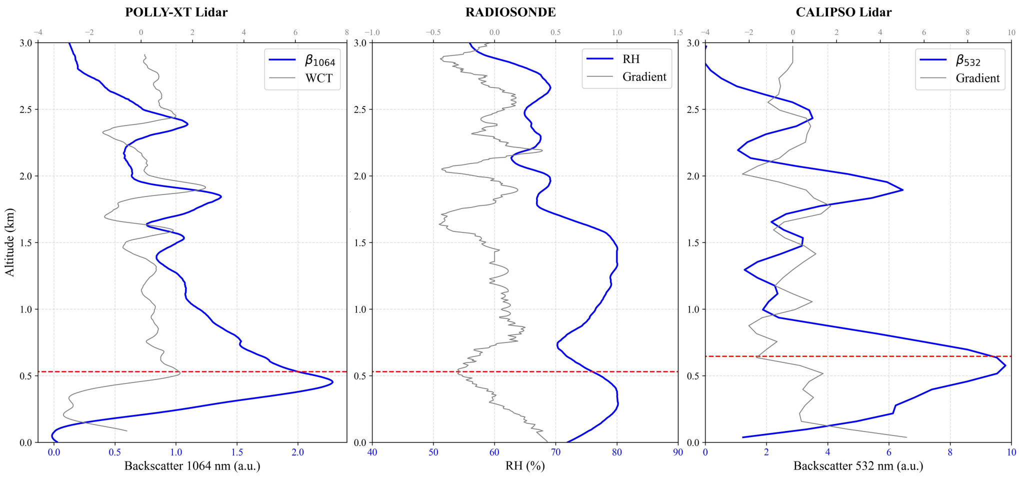

Figure 5.1: Profiles of atmospheric variables and their corresponding detection methods for determining the boundary layer (BL) top. The blue lines represent the observed signals, while the gray lines correspond to the applied methods for BL top detection. Left: Backscatter coefficient at 1064 nm from the ground-based PollyXT lidar, Middle: Relative Humidity (RH) from radiosonde, and Right: backscatter coefficient at 532 nm from the CALIPSO satellite lidar. The selected BL top is highlighted by the red dashed lines.

based and satellite), particularly in complex environments. For a satellite-based lidar like CALIOP, the signal can become highly attenuated as it approaches the Earth's surface, due to the existence of clouds above the BL. This can compromise the reliability of detecting lower tropospheric features and lead to inaccurate identification of the BL top. To mitigate this, only cloud-free profiles were selected to ensure data quality, though this restriction reduces the dataset and introduces observational limitations. Additionally, in marine environments, cumulus clouds frequently form at the BL top, which can serve as a useful, albeit indirect, marker for BL height for ground-based lidars that can detect the cloud base. Moreover, if a thin cumulus cloud is present above the BL top and allows partial laser penetration, the WCT may incorrectly identify the cloud's upper boundary as the BL top instead of the actual BL height. A similar issue occurs in the presence of dust layers, as the WCT detects reductions in the lidar signal caused by these layers. This can lead to misclassification of the dust layer boundaries as the BL top, complicating the accurate identification of the atmospheric structure. These limitations underscore the need for visual inspection to ensure accuracy in identifying the BL top in such settings, as automated methods may struggle to locate the correct layering.

5.2 Boundary Layer Characteristics in diverse environments

The characteristics of the BL during JATAC/ASKOS are examined across the contrasting environments depicted in Figure 5.2: over the Atlantic Ocean (blue rectangle - Area 1), within the ocean-desert transition zone (orange rectangle – Area 2), and in the region of Mindelo in Cabo Verde (red circle). The Sahara Desert and the Atlantic Ocean exhibit distinct conditions in terms of weather, aerosol concentrations, and therefore atmospheric dynamics. These variations are expected to influence respectively the structure and evolution of BL in selected the Areas.

The lower troposphere above the Atlantic Ocean is rich in marine aerosols, and presents relatively stable meteorological conditions, typical for open-ocean broad-scale circulations (Croft et al., 2021). In contrast, the lower troposphere over the desert is characterized by high dust aerosol concentrations, intense solar heating, and variable atmospheric stability (Giménez et al., 2010). The border region between ocean and desert introduces an interaction zone where different aerosols co-exist in big concentrations, producing unique BL characteristics due to the convergence of these differing air masses. Moreover, the existence of SAL has an impact on the on the surface radiation budget (Evan et al., 2009) and hence on the sea surface temperature (SST). Foltz and McPhaden (2008) found that Saharan dust outflows at the Tropical North Atlantic, were consistently associated with a reduction in solar radiation, with approximately 35% of SST variability attributed to dust outbreaks, while other SST cooling anomalies were linked to wind stress. The dust aerosol effect on SST depends on several factors, such as the temperature contrast between the dust layer and SST, the characteristics of the dust layer, concentration and altitude (Luo et al., 2021).

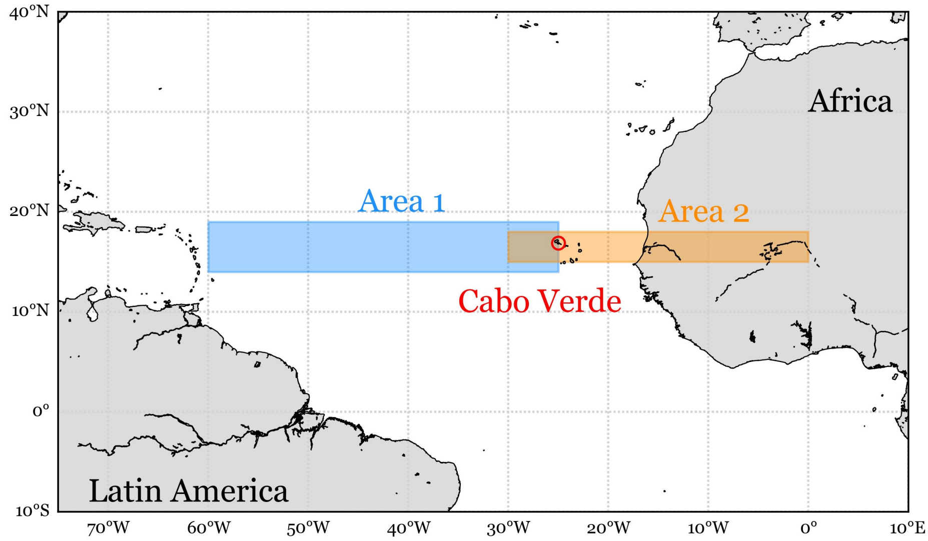

Figure 5.2: Map displaying the study areas for BL analysis: The blue rectangle (Area 1) represents the open-ocean Marine Atmospheric Boundary Layer (MABL) discussed in Section 5.2.1. The orange rectangle (Area 2) marks a transition zone at the ocean-desert interface, analysed in Section 5.2.2. The red circle is the ground-based measurements site at the Ocean Science Center Mindelo (OSCM) in Cabo Verde.

5.2.1 The ABL in the Atlantic Ocean (Area 1)

The Atlantic Ocean is characterized by dynamic weather systems and cyclonic activity, incorporating continuous exchange of heat and moisture between the sea surface and the adjacent air parcel (Schnitker, 1982). In open ocean areas such as Area 1, there is no direct interaction of the lower troposphere and the land, allowing for the development of a MABL. The MABL contains higher humidity levels and the airflow is smoother due to reduced friction from the water surface, comparing to land. Wind and temperature profiles in the MABL are mainly influenced by sea surface temperature, oceanic currents and large-scale atmospheric circulation.

In this section, we focus on the MABL characteristics within the blue rectangle of Area 1 (Figure 5.2). 10 years of CALIOP data (2012–2022) are examined, using only the profiles recorded in month September. By limiting the data to one month, we aim to achieve more homogeneous conditions to better capture the prevailing environmental characteristics (e.g. relatively consistent sea surface temperatures). Figure 5.3-left illustrates the conceptual trajectories of the CALIPSO satellite across the study area. The analysis targets cloud-free profiles measured within approximately 40 km around latitude 16.87° N, corresponding to the latitude of ground-based measuring site in Cabo Verde, as represented by the red points in Figure 5.3-left. A total of 6392 nighttime and daytime profiles (conceptually indicated in green and purple, respectively) are analyzed across longitudes from 60° W to 25° W. The spatial range of 40 km is suitable for capturing representative MABL characteristics in the study area because the selected profiles are cloud-free and measured over the ocean surface, maintaining generally homogeneous conditions of temperature, and humidity. For each profile, the derivative of the backscatter-coefficient profile at 532 nm is calculated (as in Fig. 5.1) and the minima are constrained at the lower 3 km.

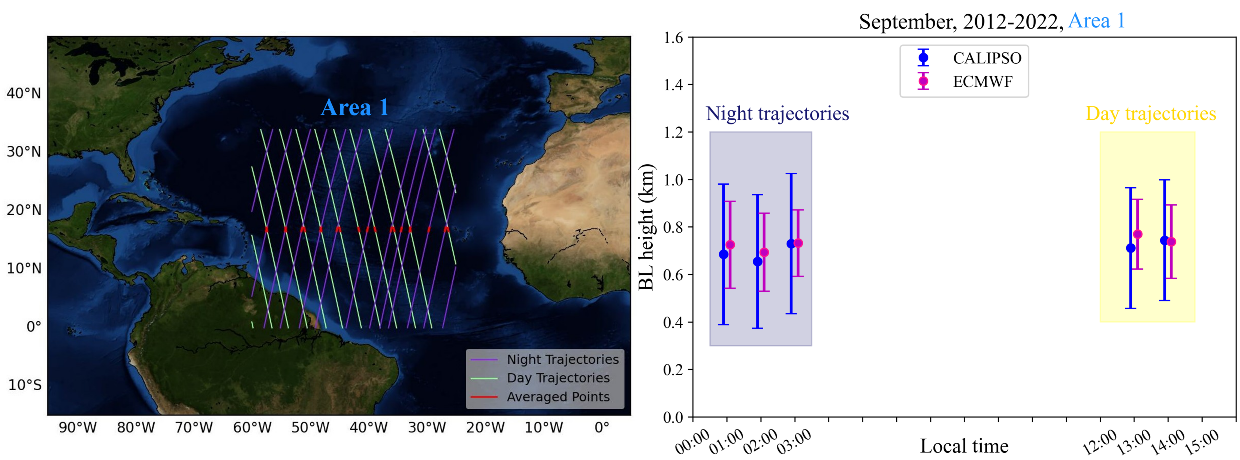

Figure 5.3: Conceptual illustration of the trajectories of the CALIPSO satellite across the study area. Right: Comparison of BL top derived from CALIPSO (blue points) and ECMWF (magenta points) for 10 years (2012-2022) in Area 1.

The results of the MABL analysis from CALIOP data are compared with BL heights derived from the ECMWF/IFS dataset. To account for longitudinal time differences, each profile's measurement time is converted to local time based on its longitude. For each CALIOP lidar profile, a temporally and spatially matched ECMWF point at the same local time is selected for direct comparison. The findings are presented in Figure 5.3-right.

The blue circles display the MABL top heights derived from CALIPSO profiles, averaged hourly in local time. The magenta points represent the corresponding hourly-averaged BL top heights from ECMWF. The data points are clustered within the 00:00–04:00 and 12:00–16:00 local time windows, because they correspond to CALIPSO's nighttime and daytime overpasses in the Atlantic region. The results show very good agreement overall, though lidar-derived BL heights carry greater uncertainty and sensitivity. This is expected, as uncertainties in the lidar profiles, occur not only from time averaging but also from the gradient method used to derive heights from CALIOP profiles, which can be challenging to automate due to low signal to noise ratios especially during daytime. In contrast, the model is less sensitive to small-scale variations, as it provides an averaged representation over a relatively large grid (0.25° or 27.83 km around 16°N). The BL top in Area 1 under cloud-free conditions, is found to consistently range between 600 and 800 meters above sea level. Although uncertainties in deriving the BL and time averaging broaden this estimate, these findings align well with expected MABL behavior that typically do not show a significant diurnal evolution.

5.2.2 The ABL in the Ocean-Desert Transition Zone (Area 2)

Area 2, highlighted by the orange rectangle in Figure 5.2, spans within longitudes of 35°W-0°: from the eastern Atlantic Ocean to the Western Africa, including the region around Cabo Verde. This area lies at the interface of two significantly different environments, as land and water interact differently with solar radiation due to their distinct heat capacities and reflective properties. On the West Africa land side, the lower troposphere directly interacts with the continental surface and the air is enriched with desert dust aerosols originating from the Sahara, where high temperatures, dry conditions, and strong winds are dominant. In contrast, the Eastern Atlantic Ocean side is predominantly influenced by marine aerosols within the lower troposphere, reflecting the ocean's stable, moisture-laden environment. In terms of heat capacity, land absorbs and releases heat quickly, leading to larger temperature fluctuations, while water absorbs energy more gradually, storing and slowly releasing it. These sharp contrasts in meteorological conditions and aerosol composition across the Area 2, are expected to have a notable impact on the BL structure.

For this analysis, similarly to section 5.2.1, cloud-free profiles were selected from the CALIPSO satellite lidar for September 2012-2022 to derive the BL top and are compared with the corresponding ECMWF data. Figure 5.4 presents the BL top results obtained from CALIPSO lidar measurements (blue points), and from the corresponding ECMWF points (magenta) along the cross-section at latitude 16.87° N (the latitude of the Mindelo observatory). The CALIPSO trajectories are divided into daytime (Fig. 5.4-left) and nighttime (Fig. 5.4-right) intervals after converting o local time, to highlight the distinct patterns of BL during different phases of the diurnal cycle.

Over the ocean surface, from 35° W to 17° W, the BL heights derived from CALIPSO and ECMWF data show good agreement for both daytime and nighttime trajectories, with values ranging from approximately 500 to 800 meters. This aligns with the findings from section 5.2.1 (Area 1). However, discrepancies arise when examining the area above the African land, extending from 17° W to 0°. During the daytime, both the CALIPSO and ECMWF measurements show high BL heights, typical for continental and desert areas where the BL top is usually elevated (Garcia-Carreras et al., 2015). Notably, ECMWF

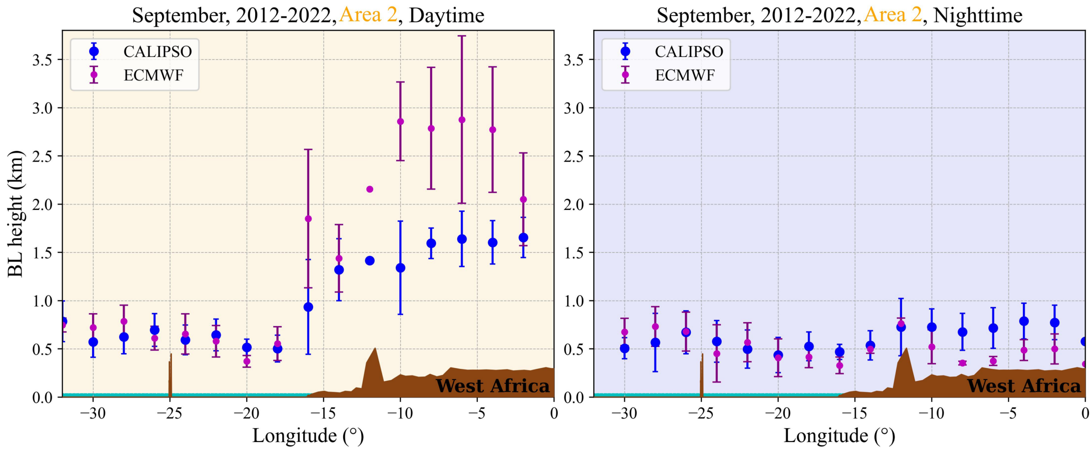

Figure 5.4: BL height along the latitude of 16.84°N for September 2012–2022 (Area 2), derived from CALIPSO lidar (blue points) and ECMWF model data (magenta points). CALIPSO trajectories were collocated with the nearest ECMWF model grid, and data were averaged over 2° longitudinal intervals. The error bars represent the variability in the BL height. The brown shaded region represents the topography of West Africa, indicating landmass and orographic features influence on the BL structure (sourced from Google Earth). The left figure illustrates daytime and the right illustrates nighttime trajectories.

reports significantly higher ABL than CALIPSO in this region during the daytime. Conversely, at night, CALIPSO often detects a higher ABL top than ECMWF. The observed discrepancies in boundary layer height over West Africa can be attributed to several factors. First, the ECMWF's Richardson-based diagnostic method may fail in cases of weak stratification, insufficient vertical resolution (especially when the ABL top is high), or significant turbulence above the classical $Ri > 0.25$ threshold, leading to overestimations. On the other hand, CALIPSO is limited in its ability to resolve the lowest few hundred meters of the atmosphere, particularly over desert regions, where signal attenuation is pronounced. CALIPSO detects the BLH primarily through changes in aerosol concentration, which may not always coincide with the thermodynamic ABL top. Furthermore, the ECMWF model outputs may be less reliable in this region due to the lack of surface stations and radiosonde data for assimilation, combined with the fact that aerosol concentrations are not assimilated in real time but based on climatology—potentially affecting the radiative balance and subsequent boundary layer development.

5.3 Focusing on Cabo Verde and JATAC/ASKOS

Cabo Verde is an archipelago in the eastern tropical Atlantic, with distinctive BL dynamics shaped by both the insular geography and the influence of surrounding mountains on airflow patterns. Specifically, the highest point is the Monte Verde (744m) on the eastern side, but there are also Caixa (535m) and Madeiral (680m) on the southern part, as well as Monte Cara (490 m) on the western part. Another geographical characteristic, is that Cabo Verde is situated directly in the path of frequent Saharan dust transport, so the region is often impacted by large dust plumes originating from the African continent and crossing over the islands. These dust events vary significantly in intensity, sometimes accumulating right above the BL or penetrating into it, while at other times showing minimal impact due to lower dust loads.

The islands of Cabo Verde, are located nearly 1000 km from the West African coast. The region of São Vicente spans approximately 227 km^2, while the neighbouring (northern) island of Santo Antão covers around 785 km^2, creating an interface where land and sea effects influence local atmospheric conditions. The origins of air drawn in to the trade winds arriving at Cape Verde are diverse depending on the season; from North America, the Atlantic, Arctic, European and African regions. During autumn, Cape Verde is situated in the direct transport pathway of easterly dust from Africa to the North Atlantic (Carpenter et al., 2010). These sea-air temperature contrasts, rough land surfaces, and fluctuating humidity contribute to a dynamic environment that reflects both marine and coastal BL characteristics.

Figure 5.5 presents the hourly average BL height over Mindelo, during September 2021 and 2022 from ECMWF data. The two grids represented in the map (blue and red), are the closest to the point of measurements in Mindelo. The BL height reveals a very small, consistent diurnal pattern with a very slight rise observed in the beginning of the morning, likely due to the day's onset of heating over the land surface. The BL top ranges from approximately 400-700 m for both grids, with a variation of around 150 m.

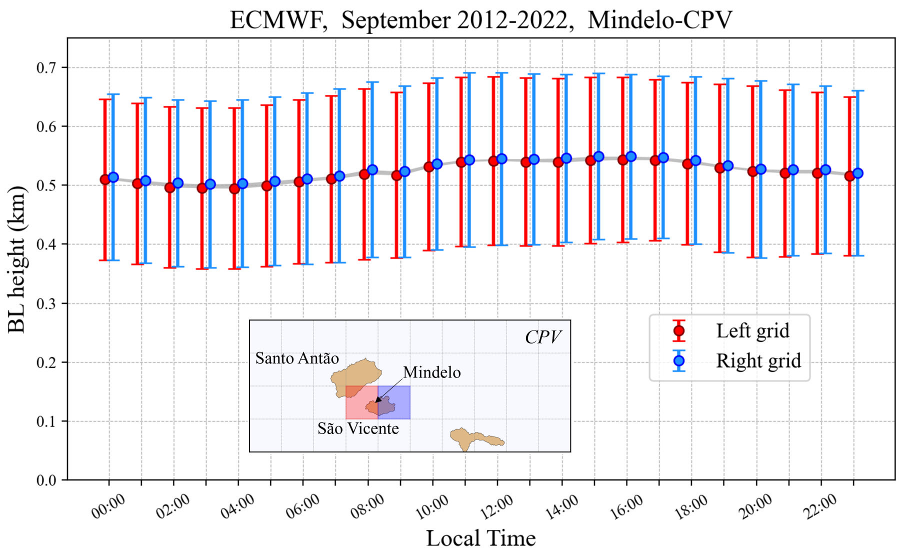

Figure 5.5: Hourly averaged diurnal evolution of Boundary Layer (BL) height over Cabo Verde for September 2022, derived from different ECMWF bins as depicted on the map: one at the top (red) and one one at the bottom (blue). The error bars represent the variability. The green dots are the difference of the BL derived from the two grids (top-bottom).

To further investigate the BL above Cabo Verde, we examine data from Radiosondes, ground-based PollyXT and Halo Lidar, CALIPSO and ECMWF/IFS model for September 2021 and 2022 (the intensive-measurements period of ASKOS). For this analysis, CALIPSO trajectories passing over the point of ground-based observations(16.87°N, 24.99°W) within a 300 km radius were carefully selected (Fig. 5.6, left). In Figure 5.6-right, the x-axis represents the BL top retrieved from CALIPSO ECMWF. The blue circles correspond to BL heights from ECMWF output, the red rectangles represent BL heights retrieved from the PollyXT Lidar and the black hexagons represent MLH retrieved from the Halo Lidar. The PollyXT and Halo points are fewer because the instruments were not operational during several overpasses. Additionally, three collocated radiosonde measurements are depicted as green stars.

The black dashed line indicates the 1:1 line (y=x), representing perfect agreement between CALIPSO and the other datasets. The grey shaded area illustrates a ±20% error margin, while the cyan shaded region corresponds to a ±100 m error margin, providing a way to assess deviations from perfect correlation and evaluate whether the data points lie within an acceptable error range. From the analysis, 77% of the red points (PollyXT), 50% of the blue points (ECMWF) and 30% of the black points (Halo) fall within the grey shaded area, indicating agreement within 20% error when comparing with CALIPSO BL height.

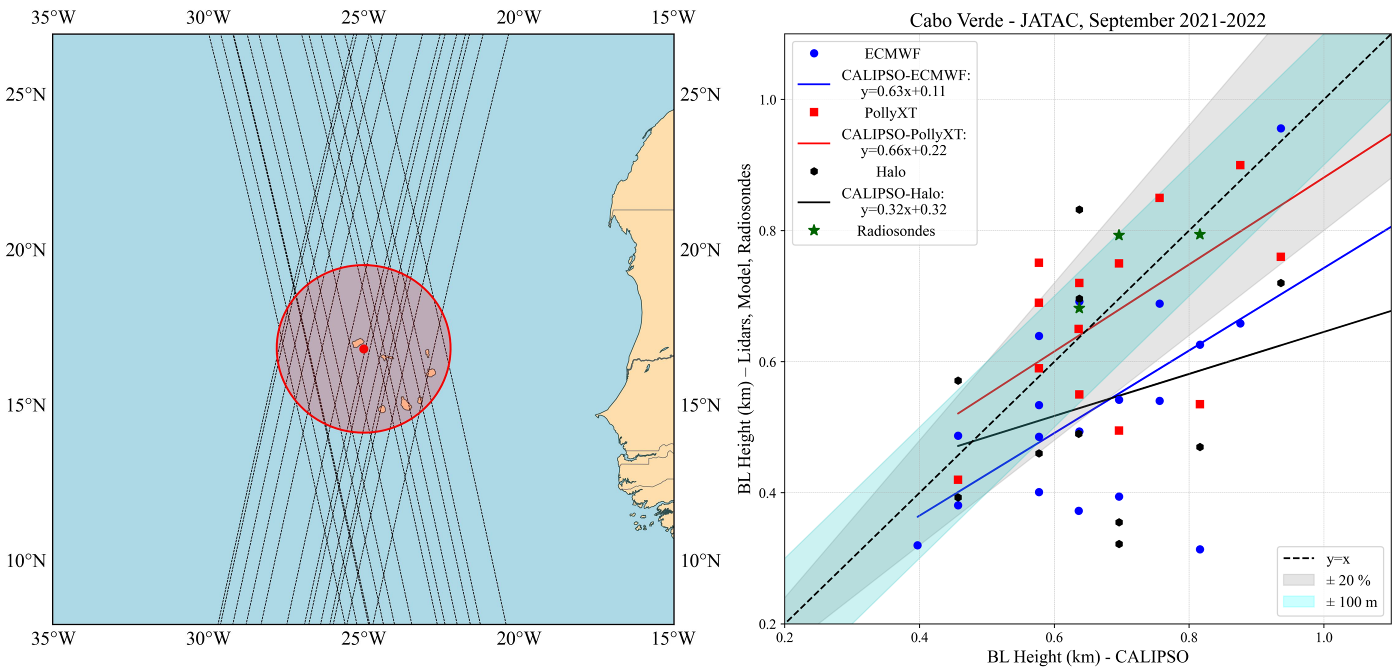

Figure 5.6: Left: Map showing CALIPSO trajectories (black dashed lines) passing over the ground-based observations site (red point: 16.87°N, 24.99°W) within a 300 km radius (red circle). Right: BL top retrieved from ECMWF (blue points), PollyXT Lidar (red rectangles), Halo Lidar (black hexagons) and Radiosondes (green stars) plotted against the corresponding BL heights from CALIPSO (x-axis). The black dashed line represents the 1:1 line (y = x), indicating perfect agreement. The gray shaded area denotes a ±20% error margin, while the cyan shaded region corresponds to a ±100 m error margin. The correlation lines are given as follows: i) CALIPSO-ECMWF y=0.66x+0.22 (blue line), ii) CALIPSO-PollyXT y=0.63x+0.11 (red line), iii) CALIPSO-Halo y=0.32x+0.32 (black solid line).

The slopes for PollyXT (0.66) and ECMWF (0.63) lines are both below 1, indicating that CALIPSO data present a satisfactory agreement with the model and the ground-based lidar. However, given their small positive intercepts (0.22 and 0.11), these datasets tend to estimate slightly lower BL compared to CALIPSO, even when their trends are generally aligned. The Halo lidar, with the lowest slope (0.32), shows the weakest correlation with CALIPSO. Its larger intercept (0.32) suggests that, while it tends to estimate lower BL heights than CALIPSO, it may show a slight overestimation at lower values of BL. This discrepancy may arise from the different detection methodologies: Halo lidar estimates the MLH using the TKE dissipation rate, whereas the gradient method applied to CALIPSO data primarily identifies layering structures, which may include the entrainment zone or remnants of a residual layer. Similarly, ECMWF use a different retrieval method (thermodynamic approach according to ECMWF, ch. 3). These differences in detection/retrieval methods could also explain why most ECMWF (blue) and Halo (black) points fall below the y=x line, suggesting a potential systematic overestimation of BL height by the space lidar.

Dust Layer above the Boundary Layer

Figure 5.7 shows HYSPLIT backward trajectories overlaid on the SST data from the ECMWF/IFS model. The trajectories trace the air masses 48 hours prior to September 12, 2022, at 16:00 (close to the radiosonde launch time), with altitudes at 500 m, 1000 m, and 2600 m. The air at 500 m and 1000 m (black dashed and grey) in Cabo Verde originate over cooler SSTs near the African shoreline (blue dashed-dotted), while the air from higher levels (2600 m-green) comes from the African continent, likely transporting desert dust.

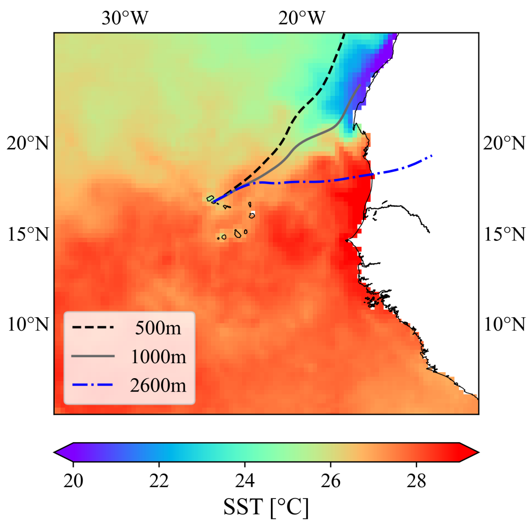

Figure 5.7: HYSPLIT backward trajectories depict air masses arriving in Mindelo, Cabo Verde, at altitudes of 500 m (black dashed line), 1000 m (grey solid line), and 2600 m (blue dashed-dotted line), 48 hours prior to 16:00 UTC on 12 September 2022, overlaid on ECMWF sea surface temperature (SST) data.

As previously discussed, it is common to observe dust layers transported from Africa to Cabo Verde, creating a distinct layering effect (Carpenter et al., 2010). At lower levels, the marine air mass is in direct contact with the sea surface, while a dust layer lies above it

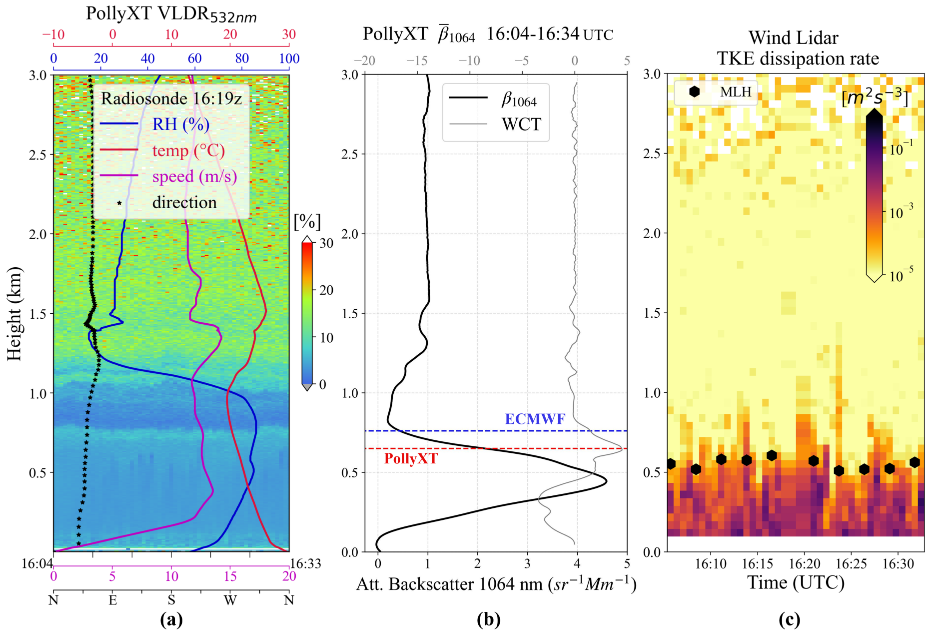

Figure 5.8: a) Radiosonde profiles for relative humidity (blue), virtual potential temperature (red), wind speed (magenta), and wind direction (black) are plotted over the Volume Depolarization Ratio at 532 nm ($VLDR_{532}$) from the PollyXT lidar, averaged within 30 minutes around the launch time at 16:19 UTC on 12 September 2022 (16:04-16:34 UTC). b) Profile of attenuated backscatter coefficient at 1064 nm (β_{1064}), averaged over the same 30-minute window, with the grey line indicating the WCT, the blue dashed line marking the BL height from ECMWF at 760 m, and the red dashed line highlighting the chosen WCT maximum at 650 m. c) Halo Wind Doppler Lidar Turbulent Kindetic Energy (TKE) dissipation rate for the same 30-minute period. The black hexagons represent the Mixing Layer Height (MLH).

(Tsikoudi et al., 2023). These two layers differ significantly in stability and aerosol composition, resulting in a stratified profile where the dust layer rests on top of the BL. Figure 5.8a, illustrates the Volume Depolarization Ratio (VLDR) of the 532nm channel from the PollyXT lidar, combined with radiosonde profiles. The greenish colour in the colorbar represents non-spherical aerosols, with depolarization values around 20%, indicative of dust particles. The PollyXT lidar data are plotted for a 30-minute period surrounding the radiosonde launch time (16:19 UTC), ensuring a close temporal match between the two datasets. The relative humidity (blue) and virtual potential temperature (red) profiles from the radiosonde reveal a pronounced inversion near 1 km, aligning well with the stratified layers observed in the depolarization data from the lidar. This inversion acts as a cap, limiting vertical mixing and promoting layer stratification. Additionally, a subtle inversion is present around 500 m in the humidity profile, which may suggest another layered structure. The wind direction (black) remains predominantly northeasterly, with a marked increase in wind speed between 1 and 1.3 km. The BL top, could be signified along the strong humidity inversion, around 1 km. Up to this range, the virtual potential temperature profile (red line) shows instability, continuously decreasing. This indicates that turbulence near the land surface promotes mixing within this layer. This is a typical profile of an unstable layer, where thermal and mechanical eddies near the surface contribute significantly in enhancing mixing. 1 km is quite elevated for a BL in this region, suggesting that local dynamics may be contributing to this feature. The high wind measured at approximately 13 m/s ($\approx$ 6 Beaufort-magenta color) at about 350 m, introduce strong wind shear and thus considerable mechanical turbulence.

Figure 5.8b presents the attenuated backscatter coefficient ($\bar{\beta}_{1064}$) profile at 1064 nm from the PollyXT lidar (black line). The profile is averaged over a 30-minute period around the radiosonde launch time (16:24–16:34 UTC). The grey line represents the WCT method, with its maximum indicating a layer top at 650 m (red dashed line). For comparison, the ECMWF BL top at the radiosonde launch time is shown as a blue dashed line at 760 m. The TKE dissipation rate from the Halo Wind Lidar (5.8c) shows larger values below approximately 520 m, aligning with the identified MLH (black hexagons). This agrees well with the BL top derived from PollyXT (red line in fig. 5.8b), indicating that both ground-based lidars consistently capture the well-mixed layer.

This aerosol condition represents a common day in Mindelo, Cabo verde. In Figure 5.9, all the retrievals of that case are cumulatively depicted. Orange shading represents the dust layer and blue shading represents the turbulence. Overall, the results for PBL height, show good agreement during the entire day (after 17:00 UTC Halo measurements are not available). $PBL_{WVMR\_PollyXT}$ is only available during 00:00-06:00 and 20:00-24:00 UTC, because of the nighttime operation of PollyXT water vapor channel. Northwestern winds dominate below 1 km (not shown), with the exception of 2:00-4:00, when they become north. At this time space, TKE is dampened and TM method does not suggest the existence of a mixing layer, while $PBL_{WVMR\_PollyXT}$ seems to be overestimated comparing to the other observations at the beginning of the day. On the other hand, during daytime a shallow PBL is observed for all methods. That limited daytime evolution is an indicative feature of coastal areas. The radiosonde launched at 10:00 captures the highest PBL top at 1.1 km. PBL_{ECMWF} is in good agreement with the rest of the retrievals.

Dust Mixture within the Boundary Layer

According to the HYSPLIT trajectories in Fig. 5.10,the air masses arriving over Mindelo at 1000 m and 2000 m altitudes originate from inland Africa, while the lower-level air mass, reaching 500 m, follows a path from the northwest coastline. This again indicates an influx of air masses with distinct characteristics, where the higher layers likely carry Saharan dust, in line with the VLDR measurements of PollyXT Lidar. Additionally, Aerosol Optical Depth (AOD) measurements from the Aerosol Robotic Network (AERONET) for this day report values around 0.6 at 500 nm (data not shown), further supporting the presence of significant dust transport.

Turbulence at the top of a daytime BL, driven by surface heating and convection, can lead to the entrainment of dust particles from an elevated layer above into the BL (Marsham et al., 2008). In these situations, the dust particles become integrated into the marine and coastal air masses, impacting aerosol concentrations and BL dynamics. In Figure 5.11a, the values of VLDR inside the BL are close to 20%, indicating the existence of dust particles in the MABL, mixed with marine particles. The radiosonde profiles of virtual potential temperature and relative humidity reveal weaker inversions than those observed in Section 5.3, with a notable inversion around 500 m, which may indicate the

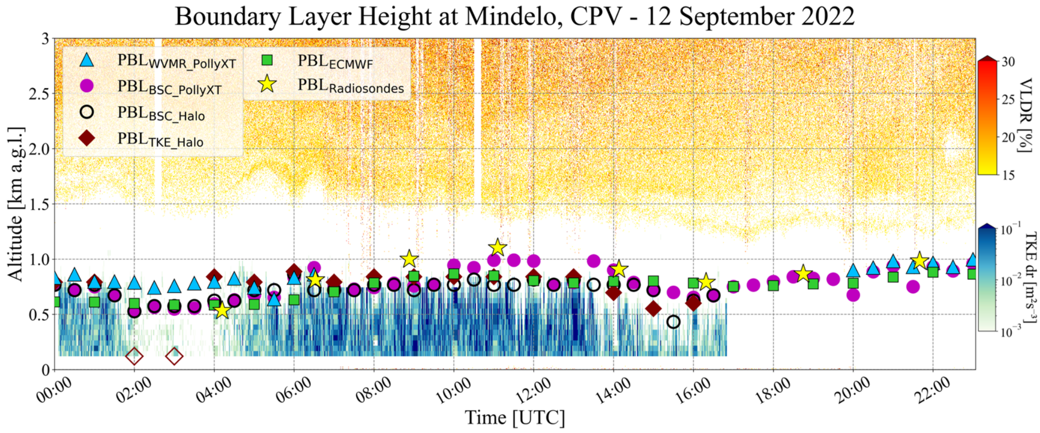

Figure 5.9: Boundary Layer Height observed on 12 September 2022:
$PBL_{WVMR\_PollyXT}$ (blue triangles) is retrieved by WCT on WVMR product of PollyXT Lidar,
$PBL_{BSC\_PollyXT}$ (purple circles) is retrieved by WCT on 1064nm BSC product of PollyXT Lidar,
PBL_{BSC_Halo} (black circles) is retrieved by WCT on BSC product of Halo Lidar,
PBL_{TKE_Halo} (maroon diamond) is retrieved by TM on TKE product of Halo Lidar and
PBL_{ECMWF} (green square) is the output of ECMWF model.
Orange shading corresponds to Volume Depolarization Ratio (VLDR) at 532 nm channel of PollyXT Lidar and blue shading corresponds to TKE dissipation rate measured by Halo Lidar.

approximate BL top in this case. This weakened inversion also suggests that the BL may be more susceptible to vertical mixing, facilitating dust intrusion from higher altitudes into the BL. On this particular day, the wind speed profile (magenta line) shows milder conditions, reaching speeds up to 10 m/s (~5 on the Beaufort scale). The direction of the wind is northern (black stars) relatively to the previous case. At the northern side of the measurements' site, there is the neighbouring Santo Antão island that could act as an obstacle to the wind's flow, shaping local dynamics that affect the vertical mixing.

The WCT method (grey line) applied to the averaged $\bar{\beta}_{1064}$ profile (Fig. 5.11b) identifies multiple maxima, none of which are particularly dominant. The most pronounced feature below 1.5 km appears at 500 m (red dashed line). The ECMWF BL top for the same time is located at 720 m (blue dashed line). The WCT method used to detect the BL top has limitations when the lidar signal is influenced by such overlying features. In such cases, it is essential to cross-check the results with independent measurements. Even when the WCT method provides a clear maximum to define the BL top, cross-checking remains essential. For instance, the radiosonde identifies the strongest humidity and temperature inversion around 1 km (Fig. 5.8a), while the PollyXT lidar detects the BL top at 650 m (Fig. 5.8b), and ECMWF estimates it at 760 m. Such discrepancies arise in complex environments like Cabo Verde, where the interplay of dust, marine aerosols, and variable meteorological conditions introduce challenges to understand the BL dynamics.

In this case, turbulent motions extend up to 600 m (Fig. 5.11d), followed by a layer of downdrafts (blue color in Fig. 5.11c) reaching approximately 1.5 km. Above this level,

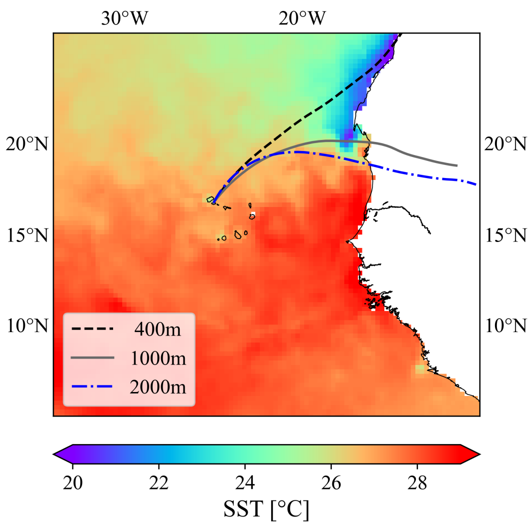

Figure 5.10: Same as Figure 5.7 for 23 September 2022. The backward trajectories are calculated at altitudes of 400 m (black dashed line), 1000 m (grey solid line), and 2000 m (blue dashed-dotted line), 48 hours prior to 19:00 UTC on 23 September 2022.

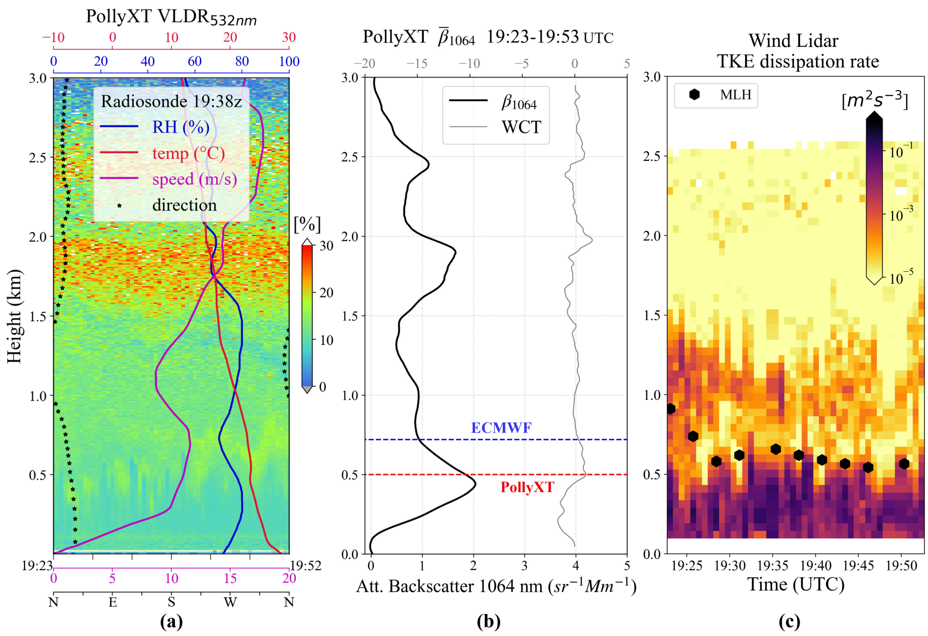

Figure 5.11: Same as Figure 5.8 for 23 September 2022. a) The radiosonde launch time at 19:38 UTC on 23 September 2022. b) ECMWF BL height (blue dashed line) at 720 m, WCT maximum (red dashed line) at 500 m. c) Halo Wind Doppler Lidar TKE dissipation rate for the same time period as PollyXT, with the black hexagons representing the MLH.

updrafts (red color) reappear, suggesting a complex vertical circulation pattern that may be influenced by local dynamics or interactions between the dust layer and the BL.

In Figure 5.12, the diurnal boundary layer for 23 September 2022 is presented. There are some alienated points above 1 km before 6:00 and after 15:00 that do not correspond to

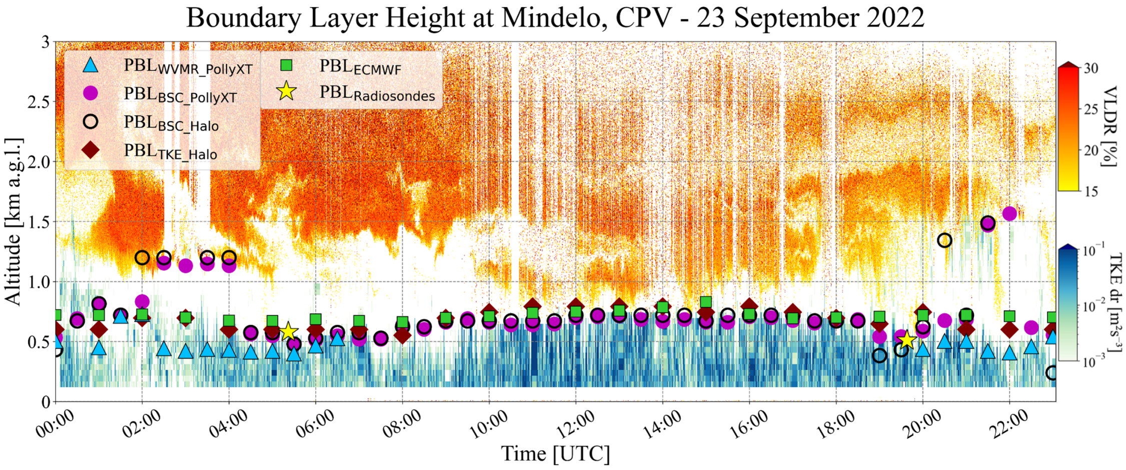

Figure 5.12: Same as Figure 5.9 for 23 September 2022.

PBL values. These 'outliers' of $PBL_{BSC\_PollyXT}$, PBL_{BSC_Halo} and $PBLWVMR\_PollyXT$ are the results of WCT, detecting elevated aerosol layers instead of the PBL top. However, TM at TKE dissipation rate and ECMWF, result in a more effective PBL representation than WCT. As mentioned also in the previous case, no sharp daytime evolution is observed. On the contrary, lower PBL values are recorded during the convective hours, relatively to 12 September. PBL_{ECMWF} is in good agreement with $PBL_{TKE_{Halo}}$ during all day and with all the results during 10:00-18:00. The radiosondes of 05:22 and 19:38 UTC capture PBL heights that are in good accordance with remote sensing captured $PBL_{BSC\_PollyXT}$, PBL_{BSC_Halo} and PBL_{TKE_Halo}, nor with the PBL_{ECMWF}.

Comparison of 12 and 23 Sep 2022

In both cases the measured PBL presents several characteristics that resemble a Marine Atmospheric Boundary Layer (MABL): it is a relatively shallow layer with no significant variability on the top. Table 5.1 shows the average and standard deviation of $PBL_{BSC\_PollyXT}$, PBL_{BSC_Halo}, PBL_{TKE_Halo} and PBL_{ECMWF}.

Table 5.1: Average and Standard deviation of PBL height retrievals

Time (UTC)	$PBL_{BSC\_PollyXT}$	PBL_{BSC_Halo}	PBL_{TKE_Halo}	PBL_{ECMWF}
12 Sep 10:00-14:00	918.6 ± 86.4 m	784 ± 24 m	811.2 ± 64.4 m	821.3 ± 35.3 m
23 Sep 10:00-14:00	672.9 ± 27.3 m	698.7 ± 25.3 m	782.4 ± 21.5 m	$748.4 \pm 27.7m$

During the period 10:00-14:00 UTC (that corresponds to 9:00-13:00 local time), standard deviation for both cases varies between 21.5 and 86.4 m, indicating low variability, that is connected with the limited daytime evolution. 23 September presents lower PBL retrievals and also smaller uncertainties comparing to 12 September during that time period. This result is a combination of the dust amount and the dust layer level. On 23 September the layer is thick and infiltrates in lower levels (approx. 1km), reducing the amount of solar radiation (Gutleben et al., 2019) that reaches the surface and also capping the top of PBL. Moreover, the lower troposphere is less turbulent than in 12 September and is therefore more stable.

The PBL results using WCT and TM are in good agreement with the PBL derived from radiosonde profiles, indicating trustworthy references for the detection of layering. BSC and WVMR are proportional to the aerosol concentration and constitute a possible indicator for PBL detection. However, when an elevated aerosol layer approaches the surface, it is likely that WCT result in big variability for the detection of layering, since this elevated layer is captured instead of PBL (23 September 02:00-04:00 and 20:30-22:00). Mindelo is an area directly influenced by the continuous ocean-atmosphere exchange of heat, moisture, and momentum. Thus, the measured PBL presents MABL characteristics. No sharp daytime evolution, or big vertical variability are observed on those relatively shallow PBL retrievals.

Chapter 6

Conclusions and Future Work

6.1 Overview of the investigated areas, aims, objectives.

This dissertation focused on investigating the dynamics and structure of the ABL in marine environments using active remote sensing instruments and radiosondes. The study leverages datasets from two distinct locations: the first is Finokalia, Crete, in the Mediterranean (PreTECT Campaign), and the second is São Vincente, in the Atlantic Ocean (ASKOS Campaign). These sites present unique conditions but also challenges for exploring the interaction of meteorology and aerosol properties with the ABL. Finokalia, a coastal site with complex terrain and distinctive meteorological patterns, contrasts with São Vicente, an island in the Atlantic influenced by desert dust transport from Western Africa. Both locations are marked by the presence of marine aerosols within the boundary layer, underscoring the interaction between marine and continental influences.

Measurements from ground-based aerosol (Raman) and Wind (Doppler) lidars provided continuous, high-resolution information on the vertical structure of the troposphere, enabling detailed analysis of meteorological and aerosol characteristics. Radiosondes were also investigated to derive reliable and detailed information on the dynamics. To expand the spatial scope, satellite lidar data from CALIPSO were employed to study the ABL dynamics over remote regions of the tropical Atlantic and investigate potential changes as the focus shifts towards the African continent. Additionally, the performance of the ECMWF model in capturing the ABL's structure was assessed in this dissertation by comparing modeled outputs with observations, examining its reliability in these complex environments.

One of the objectives of this dissertation is to identify the most effective and reliable method for studying ABL evolution. Specifically, the boundary layer top was determined using multiple approaches, including the WCT, Gradient Method, Parcel Method, Richardson Method, and Threshold Method. Additionally, this study explores the role of aerosols in influencing ABL dynamics and structure, investigates the defining characteristics of the ABL in complex coastal environments, and assesses the extent to which models accurately capture ABL evolution.

6.2 Technical Methodology and Sensitivity Analysis

Several methods were evaluated for detecting the ABL top, focusing on their performance and sensitivity under diverse environmental conditions. The **WCT** was applied to lidar-derived backscatter coefficients and water vapor mixing ratio. A sensitivity analysis highlighted the importance of selecting effective parameters to enhance the detection of ABL top features. Empirical testing identified a dilation value of 200 as optimal for this study, balancing the need to preserve profile characteristics without excessive smoothing. This parameter proved critical for accurately identifying layering potential, emphasizing that the choice of dilation and maxima detection plays a pivotal role in interpreting results reliably. Therefore, WCT is found to be the most effective method in this study for detecting the layering as long as the right parameters are set.

The **Parcel Method** demonstrated effectiveness in stable conditions, where surface heating decreases, buoyancy weakens, and turbulent mixing slows. Such conditions often occur in marine environments and during cloudy days. However, in these environments, shallow surface layers introduce instability, resulting in high values of virtual potential temperature that is impossible to encounter along the vertical profile in order to define the boundary layer top.

The **Threshold Method** is simple and straightforward, but it is most meaningful when applied to turbulent kinetic energy products, which limits its broader applicability.

The **Richardson Method**, is based on weighting the buoyant suppression and shear-driven turbulence, explaining the most importan factors that account for BL behavior. To perform this method in this study, winds from halo Wind Lidar, water vapor mixing ratio from PollyXT Lidar and temperature profiles from WRF were used. The critical 0.25 threshold was tested, but did not consistently produce meaningful results, and a universally effective critical threshold was lacked. Although this method successfully detected layering under certain thresholds, its computational intensity and inconsistent performance made it less practical for routine use in this study.

6.3 Findings from Finokalia: Complex Terrain and Meteorological Variability

The ABL evolution in Finokalia is found to be affected by the coastal steep cliff that shapes local meteorological characteristics. It has been specifically observed that the wind direction is the main driver of the ABL structure. Statistical analysis shows that W winds along the coast are dominant in the lower levels most of the time during PreTECT Campaign, forming a shallow ABL that does not present sharp daytime evolution. In addition, when N winds meet the coastline, the forming ABL is clearly higher. North winds are orthogonal to the local cliff terrain, and force mechanical lifting of the air, resulting in an elevated MABL up to 1 km above ground level. In contrast, the above-mentioned westerly winds originate from inland regions of Crete and typically carry warmer air, creating a shallower ABL. It is remarkable that during a sunny day (14 April 2017) the ABL is more shallow than in comparison to a cloudy one (10 April 2017). As a conclusion, ABL above Finokalia, appears to be dominated by coastal flows rather than thermal convection. The strong winds along the coast, is capping the development of the ABL. The sensitivity of various detection methods, combined with the influence of clouds and aerosols, highlights the challenges of automatically determining ABL characteristics using remote sensing.

Comparing our observations with the ECMWF/IFS model results, using a sea surface bin and a land surface bin close to the station, lead to the conclusion that in both cases, there is overestimation of the boundary layer, with the exception of nighttime hours (00:00-06:00, 18:00-24:00 UTC), where the land bin underestimates the observed boundary layer. A coastal region with complex topography like Finokalia, where convection plays a much smaller role in ABL evolution, favors the formation of a PBL that is not well described by the relatively coarse scale model. The model-measurements differences are addressed to the influence of changes in surface roughness in combination with the horizontal advection of air across this discontinuity. This also emphasizes the importance of the actual ABL measurements when the models are uncertain in such regions.

6.4 Findings from Cabo Verde: Marine Boundary Layer and Dust Aerosols

Understanding the Atlantic BL is of critical importance for accurately characterizing the complex interactions between the ocean and the atmosphere, particularly in the presence of transported Saharan dust. These interactions govern fundamental processes such as evaporation, sea surface temperature variability, and the formation of marine clouds, all of which have significant implications for climate modelling and marine ecosystem productivity due to dust nutrient deposition.

Our findings demonstrate that, based on 10 years (2012-2022) of CALIPSO measurements over the open Atlantic (Area 1), the BL height ranges from 600 m to 800 m for both daytime and nighttime trajectories, with cloud-free profiles considered during September. Furthermore, a strong correlation is observed between the CALIPSO measurements and ECMWF/IFS model outputs for this Area during the decade. However, the variations associated with CALIPSO BL are significantly larger than those of the ECMWF/IFS model outputs. CALIPSO's sensitivity to small-scale features such as aerosols and clouds leads to more variability in the data. In contrast, ECMWF/IFS model outputs are based on global atmospheric simulations that provide a more general, smoothed estimate with less sensitivity to local disturbances.

The analysis of Area 2 reveals distinct BL characteristics over the ocean and land, shaped by differences in surface properties, meteorological conditions, and aerosol composition. Over the ocean (35°W–17°W), CALIPSO and ECMWF show strong agreement in BL heights, typically ranging from 500 to 800 meters, consistent with findings from Area 1. However, over the examined area of land (17°W–0°), discrepancies emerge, particularly during the daytime, when ECMWF estimates a significantly higher BL top than CALIPSO. This likely stems from limitations in both datasets: the ECMWF Richardson-based method may fail under weak stratification or poor vertical resolution, while CALIPSO cannot resolve the lowest atmospheric layers well, especially over desert. The satellite lidar detects the boundary layer using aerosols as tracers, whereas the model estimates it based on the Richardson number, relying on thermodynamic variables such as temperature, humidity, and wind, along with certain assumptions (see Section 2.3.4). Additionally, the lack of observational data on the surface and the under-representation of aerosols in the model (Morcrette et al., 2008; Bozzo et al., 2020; Rémy et al., 2024) may also contribute to these differences by affecting the radiation budget. At night overland, CALIPSO generally reports higher BL than ECMWF, which is most probably due to the presence of the residual layer that provides an aerosol layer height higher than the thermodynamically defined BL top.

In Cabo Verde, collocated data from CALIPSO, PollyXT, Halo Lidar and radiosondes were analyzed for September 2021–2022. Correlations between all measurements and ECMWF with CALIPSO data were assessed. 77% of the PollyXT points, 50% of the ECMWF points and 30% of the Halo points indicate agreement within 20% error when comparing with CALIPSO BL height. The weakest correlation is observed between CALIPSO and Halo Lidar, due to methodological differences —CALIPSO primarily detects layering that may include the residual layer, while Halo Lidar estimates the mixing layer height based on TKE dissipation rate. Moreover, systematic differences could arise from variations in measurement techniques, retrieval algorithms, or even inherent model biases in representing BL processes.

To further investigate the situation in Cabo Verde, two cases with distinct thermodynamic conditions were examined. The first case (12 September 2022) is characterized by stronger inversions and dust aerosols primarily above the capping layer. Temperature and humidity inversions are observed at approximately 1 km; however, PollyXT and Halo Lidar detect the top of the BL at 650 and 520 m, respectively, aligning more closely with the marine BL. Although the two ground-based lidars show good agreement, the radiosonde profile indicates a higher BL top near 1 km. This discrepancy likely arises because the lidars primarily capture the well-mixed layer, whereas the radiosonde inversion marks a more stable upper boundary, potentially corresponding to the entrainment zone or a decoupled residual layer. Such differences are anticipated in complex environments like Cabo Verde, where the interplay of dust, marine aerosols, and variable meteorological conditions introduce challenges in understanding the dynamics of BL. In the second case (23 September 2022), characterized by a weaker inversion and dust aerosols within the BL, the BL top was found lower, with both ground-based lidars detecting it around 500 m. The key differences in this case are the smoother wind speed and a more northerly wind direction. The northern wind flow may have been influenced by the presence of Santo Antão island to the north, impacting local dynamics. Additionally, the slope of the virtual potential temperature profile suggests less unstable conditions, promoting better vertical mixing and enabling dust to enter the BL.

The observed differences in BL height can be mainly attributed to the mechanical turbulence driven by strong winds in the first case, highlighting the variability of the atmospheric conditions in this region, that is influenced by a combination of marine and dust aerosols, as well as the complex sea-land interactions in between, that contribute to the diverse atmospheric conditions. SST emerges as a key factor, driving BL evolution, fostering an unstable lower troposphere. This dissertation suggests that when these complex conditions favor less instability, desert dust from the SAL is more efficiently penetrating to the BL. This mechanism should be further examined on its importance as a facilitator of dust deposition to the ocean. Experiments such as JATAC bring the observational synergies needed to study complex BL dynamics governing dust transport.

6.5 Future Work

In future work, the study shall be expanded to additional locations with unique atmospheric characteristics, particularly PANhellenic GEophysical observatory of Antikythera (PANGEA), which is being developed as a "superstation" for advanced atmospheric observations. This site will host a variety of remote sensing instruments, including PollyXT Raman lidar, Halo Doppler lidar, cloud radar, and radiosondes. PANGEA will serve as a ground-based reference station for the calibration and validation of satellite missions, such as the Earth Cloud Aerosol and Radiation Explorer (EarthCARE), launched in 28 May 2024. Using data from these instruments, it is important to study boundary layer dynamics and develop an automated tool tailored to this region. Another possible future research study, could be the creation of an automated algorithm that retrieves the PBL height in Finokalia, given an established pattern of the winds interfering the PBL height behavior. Such advancements could improve the understanding of ABL behavior in marine environments and provide reliable techniques for the detection of the top using remote sensing, even under cloudy conditions.

Additionally, future work includes leveraging the cloud radar to detect low-level clouds that often form atop the boundary layer. These clouds are challenging to identify using lidar due to overlap limitations at such low altitudes, and due to attenuation of the laser signal within the cloud. Integrating cloud radar data with other remote sensing observations will help characterize these phenomena and their interaction with the boundary layer. This research will contribute to improving measurement strategies of marine atmospheric boundary layer processes.

Bibliography

Amiridis, V., Kazadzis, S., Gkikas, A., Voudouri, K. A., Kouklaki, D., Koukouli, M.-E., Garane, K., Georgoulias, A. K., Solomos, S., Varlas, G. et al. (2024), 'Natural aerosols, gaseous precursors and their impacts in greece: A review from the remote sensing perspective', *Atmosphere* **15**(7), 753.

Amiridis, V., Marinou, E., Tsekeri, A., Wandinger, U., Schwarz, A., Giannakaki, E., Mamouri, R., Kokkalis, P., Binietoglou, I., Solomos, S., Herekakis, T., Kazadzis, S., Gerasopoulos, E., Proestakis, E., Kottas, M., Balis, D., Papayannis, A., Kontoes, C., Kourtidis, K., Papagiannopoulos, N., Mona, L., Pappalardo, G., Le Rille, O. and Ansmann, A. (2015), 'Livas: a 3-d multi-wavelength aerosol/cloud database based on calipso and earlinet', *Atmospheric Chemistry and Physics* **15**(13), 7127–7153.
URL: *https://acp.copernicus.org/articles/15/7127/2015/*

Amiridis, V., Melas, D., Balis, D., Papayannis, A., Founda, D., Katragkou, E., Giannakaki, E., Mamouri, R., Gerasopoulos, E. and Zerefos, C. (2007), 'Aerosol lidar observations and model calculations of the planetary boundary layer evolution over greece, during the march 2006 total solar eclipse', *Atmospheric Chemistry and Physics* **7**(24), 6181–6189.

Ansmann, A., Rittmeister, F., Engelmann, R., Basart, S., Jorba, O., Spyrou, C., Remy, S., Skupin, A., Baars, H., Seifert, P. et al. (2017), 'Profiling of saharan dust from the caribbean to western africa–part 2: Shipborne lidar measurements versus forecasts', *Atmospheric Chemistry and Physics* **17**(24), 14987–15006.

Aryee, J., Amekudzi, L., Preko, K., Atiah, W. and Danuor, S. (2020), 'Estimation of planetary boundary layer height from radiosonde profiles over west africa during the amma field campaign: Intercomparison of different methods', *Scientific African* **7**, e00228.

Baars, H., Ansmann, A., Engelmann, R. and Althausen, D. (2008), 'Continuous monitoring of the boundary-layer top with lidar', *Atmospheric Chemistry and Physics* **8**(23), 7281–7296.
URL: *https://acp.copernicus.org/articles/8/7281/2008/*

Barlow, J., Best, M., Bohnenstengel, S. I., Clark, P., Grimmond, S., Lean, H., Christen, A., Emeis, S., Haeffelin, M., Harman, I. N. et al. (2017), 'Developing a research strategy to better understand, observe, and simulate urban atmospheric processes at kilometer to subkilometer scales', *Bulletin of the American Meteorological Society* **98**(10), ES261–ES264.

Bates, T. S., Quinn, P. K., Coffman, D. J., Johnson, J. E., Miller, T. L., Covert, D. S., Wiedensohler, A., Leinert, S., Nowak, A. and Neusüss, C. (2001), 'Regional physical and chemical properties of the marine boundary layer aerosol across the atlantic during aerosols99: An overview', *Journal of Geophysical Research: Atmospheres* **106**(D18), 20767–20782.

Belamari, S. and Céron, J.-P. (2005), Gabor analysis of the intraseasonal oceanic variability simulated in the tropical pacific ocean by a regional coupled model, *in* 'EGU General Assembly'.

Ben-Ami, Y., Koren, I. and Altaratz, O. (2009), 'Patterns of north african dust transport over the atlantic: winter vs. summer, based on calipso first year data', *Atmospheric Chemistry and Physics* **9**(20), 7867–7875.

Benjamin, S. G. (1986), 'Some effects of surface heating and topography on the regional severe storm environment. part ii: Two-dimensional idealized experiments', *Monthly weather review* **114**(2), 330–343.

Benjamin, S. G. and Carlson, T. N. (1986), 'Some effects of surface heating and topography on the regional severe storm environment. part i: Three-dimensional simulations', *Monthly weather review* **114**(2), 307–329.

Berhane, S. A., Kumar, K. R. and Bu, L. (2024), 'A 13-year space-based climatological evolution of desert dust aerosols in the middle east and north africa regions observed by the calipso', *Science of The Total Environment* **948**, 174793.

Bjerknes, J. (1964), Atlantic air-sea interaction, Vol. 10 of *Advances in Geophysics*, Elsevier, pp. 1–82.
URL: *https://www.sciencedirect.com/science/article/pii/S0065268708600059*

Blay-Carreras, E., Pino, D., Vilà-Guerau de Arellano, J., van de Boer, A., De Coster, O., Darbieu, C., Hartogensis, O., Lohou, F., Lothon, M. and Pietersen, H. (2014), 'Role of the residual layer and large-scale subsidence on the development and evolution of the convective boundary layer', *Atmospheric Chemistry and Physics* **14**(9), 4515–4530.

Bossioli, E., Tombrou, M., Kalogiros, J., Allan, J., Bacak, A., Bezantakos, S., Biskos, G., Coe, H., Jones, B., Kouvarakis, G. et al. (2016), 'Atmospheric composition in the eastern mediterranean: Influence of biomass burning during summertime using the wrf-chem model', *Atmospheric Environment* **132**, 317–331.

Bougiatioti, A., Fountoukis, C., Kalivitis, N., Pandis, S. N., Nenes, A. and Mihalopoulos, N. (2009), 'Cloud condensation nuclei measurements in the marine boundary layer of the eastern mediterranean: Ccn closure and droplet growth kinetics', *Atmospheric Chemistry and Physics* **9**(18), 7053–7066.

Bozzo, A., Benedetti, A., Flemming, J., Kipling, Z. and Rémy, S. (2020), 'An aerosol climatology for global models based on the tropospheric aerosol scheme in the integrated forecasting system of ecmwf', *Geoscientific Model Development* **13**(3), 1007–1034.

Brooks, I. M. (2003), 'Finding boundary layer top: Application of a wavelet covariance transform to lidar backscatter profiles', *Journal of Atmospheric and Oceanic Technology* **20**(8), 1092–1105.

Browning, K. and Wexler, R. (1968), 'The determination of kinematic properties of a wind field using doppler radar', *Journal of Applied meteorology and climatology* **7**(1), 105–113.

Canché-Cab, L., San-Pedro, L., Ali, B., Rivero, M. and Escalante, M. (2024), 'The atmospheric boundary layer: a review of current challenges and a new generation of machine learning techniques', *Artificial Intelligence Review* **57**(12), 1–51.

Carlson, T. N. (2016), 'The saharan elevated mixed layer and its aerosol optical depth', *The Open Atmospheric Science Journal* **10**(1).

Carpenter, L., Fleming, Z. L., Read, K., Lee, J., Moller, S., Hopkins, J., Purvis, R., Lewis, A., Müller, K., Heinold, B. et al. (2010), 'Seasonal characteristics of tropical marine boundary layer air measured at the cape verde atmospheric observatory', *Journal of Atmospheric Chemistry* **67**, 87–140.

Carrillo, J., Guerra, J., Cuevas, E. and Barrancos, J. (2016), 'Characterization of the marine boundary layer and the trade-wind inversion over the sub-tropical north atlantic', *Boundary-layer meteorology* **158**(2), 311–330.

Cebeci, T. (2012), *Analysis of turbulent boundary layers*, Elsevier.

Change, I. P. O. C. (2007), 'Climate change 2007: The physical science basis', *Agenda* **6**(07), 333.

Chen, Z., Schofield, R., Keywood, M., Cleland, S., Williams, A. G., Wilson, S., Griffiths, A. and Xiang, Y. (2023), 'Observations of the boundary layer in the cape grim coastal region: Interaction with wind and the influences of continental sources', *Remote Sensing* **15**(2), 461.

Choi, Y. and Noh, Y. (2020), 'Comparison of the atmospheric and oceanic boundary layers during convection and their latitudinal dependence', *Journal of Geophysical Research: Oceans* **125**(7), e2019JC015754.

Clauser, F. H. (1956), 'The turbulent boundary layer', *Advances in applied mechanics* **4**, 1–51.

Cohen, M. X. (2019), 'A better way to define and describe morlet wavelets for time-frequency analysis', *NeuroImage* **199**, 81–86.

Collaud Coen, M., Praz, C., Haefele, A., Ruffieux, D., Kaufmann, P. and Calpini, B. (2014), 'Determination and climatology of the planetary boundary layer height above the swiss plateau by in situ and remote sensing measurements as well as by the cosmo-2 model', *Atmospheric Chemistry and Physics* **14**(23), 13205–13221.

Comerón, A., Sicard, M. and Rocadenbosch, F. (2013), 'Wavelet correlation transform method and gradient method to determine aerosol layering from lidar returns: some comments', *Journal of Atmospheric and Oceanic Technology* **30**(6), 1189–1193.

Croft, B., Martin, R. V., Moore, R. H., Ziemba, L. D., Crosbie, E. C., Liu, H., Russell, L. M., Saliba, G., Wisthaler, A., Müller, M. et al. (2021), 'Factors controlling marine aerosol size distributions and their climate effects over the northwest atlantic ocean region', *Atmospheric Chemistry and Physics* **21**(3), 1889–1916.

Cuesta, J., Marsham, J. H., Parker, D. J. and Flamant, C. (2009), 'Dynamical mechanisms controlling the vertical redistribution of dust and the thermodynamic structure of the west saharan atmospheric boundary layer during summer', *Atmospheric Science Letters* **10**(1), 34–42.

Dai, G., Althausen, D., Hofer, J., Engelmann, R., Seifert, P., Bühl, J., Mamouri, R.-E., Wu, S. and Ansmann, A. (2018), 'Calibration of raman lidar water vapor profiles by means of aeronet photometer observations and gdas meteorological data', *Atmospheric Measurement Techniques* **11**(5), 2735–2748.

Dandou, A., Tombrou, M., Kalogiros, J., Bossioli, E., Biskos, G., Mihalopoulos, N. and Coe, H. (2017), 'Investigation of turbulence parametrization schemes with reference to the atmospheric boundary layer over the aegean sea during etesian winds', *Boundary-Layer Meteorology* **164**, 303–329.

Dang, R., Yang, Y., Hu, X.-M., Wang, Z. and Zhang, S. (2019), 'A review of techniques for diagnosing the atmospheric boundary layer height (ablh) using aerosol lidar data', *Remote Sensing* **11**(13), 1590.

Davis, K. J., Gamage, N., Hagelberg, C., Kiemle, C., Lenschow, D. and Sullivan, P. (2000), 'An objective method for deriving atmospheric structure from airborne lidar observations', *Journal of Atmospheric and Oceanic Technology* **17**(11), 1455–1468.

de Arruda Moreira, G., Sánchez-Hernández, G., Guerrero-Rascado, J. L., Cazorla, A. and Alados-Arboledas, L. (2022), 'Estimating the urban atmospheric boundary layer height from remote sensing applying machine learning techniques', *Atmospheric Research* **266**, 105962.

Díaz, J. P., Expósito, F. J., Pérez, J. C., González, A., Wang, Y., Haimberger, L. and Wang, J. (2019), 'Long-term trends in marine boundary layer properties over the atlantic ocean', *Journal of Climate* **32**(10), 2991–3004.

Diner, D. J., Ackerman, T. P., Anderson, T. L., Bösenberg, J., Braverman, A. J., Charlson, R. J., Collins, W. D., Davies, R., Holben, B. N., Hostetler, C. A. et al. (2004), 'Paragon: An integrated approach for characterizing aerosol climate impacts and environmental interactions', *Bulletin of the American Meteorological Society* **85**(10), 1491–1502.

Dourado, M. and Oliveira, A. P. d. (2001), 'Observational description of the atmospheric and oceanic boundary layers over the atlantic ocean', *Revista Brasileira de Oceanografia* **49**, 49–59.

Duncan Jr, J. B., Bianco, L., Adler, B., Bell, T., Djalalova, I. V., Riihimaki, L., Sedlar, J., Smith, E. N., Turner, D. D., Wagner, T. J. et al. (2022), 'Evaluating convective planetary boundary layer height estimations resolved by both active and passive remote sensing instruments during the cheesehead19 field campaign', *Atmospheric Measurement Techniques* **15**(8), 2479–2502.

Dunion, J. P. and Velden, C. S. (2004), 'The impact of the saharan air layer on atlantic tropical cyclone activity', *Bulletin of the American Meteorological Society* **85**(3), 353–366.

Durre, I., Vose, R. S. and Wuertz, D. B. (2006), 'Overview of the integrated global radiosonde archive', *Journal of Climate* **19**(1), 53–68.

ECMWF (2017), *IFS Documentation CY43R3 - Part IV: Physical processes*, number 4, ECMWF.
URL: *https://www.ecmwf.int/node/17736*

Edson, J., Crawford, T., Crescenti, J., Farrar, T., Frew, N., Gerbi, G., Helmis, C., Hristov, T., Khelif, D., Jessup, A. et al. (2007), 'The coupled boundary layers and air–sea transfer experiment in low winds', *Bulletin of the American Meteorological Society* **88**(3), 341–356.

Edson, J., Paluszkiewicz, T., Sandgathe, S., Vincent, L., Goodman, L., Curtin, T., Hollister, J., Colton, M., Anderson, S., Andreas, E. et al. (1999), 'Coupled marine boundary layers and air-sea interaction initiative: combining process studies, simulations, and numerical models', *Office of Naval Reasearch* .

Eleftheriadis, K., Colbeck, I., Housiadas, C., Lazaridis, M., Mihalopoulos, N., Mitsakou, C., Smolik, J. and Ždímal, V. (2006), 'Size distribution, composition and origin of the submicron aerosol in the marine boundary layer during the eastern mediterranean "sub-aero" experiment', *Atmospheric Environment* **40**(32), 6245–6260.

Emeis, S. (2010), *Surface-based remote sensing of the atmospheric boundary layer*, Vol. 40, Springer Science & Business Media.

Engelmann, R., Kanitz, T., Baars, H., Heese, B., Althausen, D., Skupin, A., Wandinger, U., Komppula, M., Stachlewska, I. S., Amiridis, V. et al. (2016), 'The automated multiwavelength raman polarization and water-vapor lidar polly xt: The next generation', *Atmospheric Measurement Techniques* **9**(4), 1767–1784.

Evan, A. T., Vimont, D. J., Heidinger, A. K., Kossin, J. P. and Bennartz, R. (2009), 'The role of aerosols in the evolution of tropical north atlantic ocean temperature anomalies', *Science* **324**(5928), 778–781.

Fairall, C., Bariteau, L., Grachev, A., Hill, R., Wolfe, D., Brewer, W., Tucker, S., Hare, J. and Angevine, W. (2006), 'Turbulent bulk transfer coefficients and ozone deposition velocity in the international consortium for atmospheric research into transport and transformation', *Journal of Geophysical Research: Atmospheres* **111**(D23).

Fairall, C. and Davidson, K. (1986), Dynamics and modeling of aerosols in the marine atmospheric boundary layer, *in* 'Oceanic Whitecaps: And Their Role in Air-Sea Exchange Processes', Springer, pp. 195–208.

Faloona, I. (2009), 'Sulfur processing in the marine atmospheric boundary layer: A review and critical assessment of modeling uncertainties', *Atmospheric Environment* **43**(18), 2841–2854.

Fan, S., Wang, B., Tesche, M., Engelmann, R., Althausen, A., Liu, J., Zhu, W., Fan, Q., Li, M., Ta, N. et al. (2008), 'Meteorological conditions and structures of atmospheric boundary layer in october 2004 over pearl river delta area', *Atmospheric Environment* **42**(25), 6174–6186.

Farmer, D. K., Cappa, C. D. and Kreidenweis, S. M. (2015), 'Atmospheric processes and their controlling influence on cloud condensation nuclei activity', *Chemical Reviews* **115**(10), 4199–4217.

Fedorovich, E., Conzemius, R. and Mironov, D. (2004), 'Convective entrainment into a shear-free, linearly stratified atmosphere: Bulk models reevaluated through large eddy simulations', *Journal of the atmospheric sciences* **61**(3), 281–295.

Field, C. B. and Barros, V. R. (2014), *Climate change 2014–Impacts, adaptation and vulnerability: Regional aspects*, Cambridge University Press.

Foltz, G. R. and McPhaden, M. J. (2008), 'Impact of saharan dust on tropical north atlantic sst', *Journal of Climate* **21**(19), 5048–5060.

Foth, A., Baars, H., Di Girolamo, P. and Pospichal, B. (2015), 'Water vapour profiles from raman lidar automatically calibrated by microwave radiometer data during hope', *Atmospheric Chemistry and Physics* **15**(14), 7753–7763.

Fuchs, J., Cermak, J., Andersen, H., Hollmann, R. and Schwarz, K. (2017), 'On the influence of air mass origin on low-cloud properties in the southeast atlantic', *Journal of Geophysical Research: Atmospheres* **122**(20), 11–076.

Garcia-Carreras, L., Parker, D., Marsham, J., Rosenberg, P., Brooks, I., Lock, A., Marenco, F., McQuaid, J. and Hobby, M. (2015), 'The turbulent structure and diurnal growth of the saharan atmospheric boundary layer', *Journal of the Atmospheric Sciences* **72**(2), 693–713.

Garratt, J. and Ryan, B. (1989), 'The structure of the stably stratified internal boundary layer in offshore flow over the sea', *Boundary-layer meteorology* **47**, 17–40.

Generoso, S., Bey, I., Labonne, M. and Bréon, F.-M. (2008), 'Aerosol vertical distribution in dust outflow over the atlantic: Comparisons between geos-chem and cloud-aerosol lidar and infrared pathfinder satellite observation (calipso)', *Journal of Geophysical Research: Atmospheres* **113**(D24).

Gerasopoulos, E., Amiridis, V., Kazadzis, S., Kokkalis, P., Eleftheratos, K., Andreae, M., Andreae, T., El-Askary, H. and Zerefos, C. (2010), 'Three-year ground based measurements of aerosol optical depth over the eastern mediterranean: the urban environment of athens', *Atmospheric Chemistry & Physics Discussions* **10**(11), 28273–28309.

Giménez, J., Pastor, C., Castañer, R., Nicolás, J., Crespo, J. and Carratalá, A. (2010), 'Influence of saharan dust outbreaks and atmospheric stability upon vertical profiles of size-segregated aerosols and water vapor', *Atmospheric Environment* **44**(3), 338–346.

Gkikas, A., Proestakis, E., Amiridis, V., Kazadzis, S., Di Tomaso, E., Marinou, E., Hatzianastassiou, N., Kok, J. F. and García-Pando, C. P. (2022), 'Quantification of the dust optical depth across spatiotemporal scales with the midas global dataset (2003–2017)', *Atmospheric Chemistry and Physics* **22**(5), 3553–3578.

Granados-Muñoz, M., Navas-Guzmán, F., Bravo-Aranda, J., Guerrero-Rascado, J., Lyamani, H., Fernández-Gálvez, J. and Alados-Arboledas, L. (2012), 'Automatic determination of the planetary boundary layer height using lidar: One-year analysis over southeastern spain', *Journal of Geophysical Research: Atmospheres* **117**(D18).

Graps, A. (1995), 'An introduction to wavelets', *IEEE computational science and engineering* **2**(2), 50–61.

Grimsdell, A. W. and Angevine, W. M. (2002), 'Observations of the afternoon transition of the convective boundary layer', *Journal of Applied Meteorology and Climatology* **41**(1), 3–11.

Groß, S., Gasteiger, J., Freudenthaler, V., Müller, T., Sauer, D., Toledano, C. and Ansmann, A. (2016), 'Saharan dust contribution to the caribbean summertime boundary layer–a lidar study during saltrace', *Atmospheric Chemistry and Physics* **16**(18), 11535–11546.

Gutleben, M., Groß, S., Wirth, M., Emde, C. and Mayer, B. (2019), 'Impacts of water vapor on saharan air layer radiative heating', *Geophysical Research Letters* **46**(24), 14854–14862.

Han, S., Bian, H., Tie, X., Xie, Y., Sun, M. and Liu, A. (2009), 'Impact of nocturnal planetary boundary layer on urban air pollutants: Measurements from a 250-m tower over tianjin, china', *Journal of hazardous materials* **162**(1), 264–269.

Hanson, H. P. (1991), 'Marine stratocumulus climatologies', *International journal of climatology* **11**(2), 147–164.

Heinemann, G. (2008), 'The polar regions: a natural laboratory for boundary layer meteorology-a review', *Meteorologische Zeitschrift* **17**(5), 589.

Heinold, B., Tegen, I., Schepanski, K. and Hellmuth, O. (2008), 'Dust radiative feedback on saharan boundary layer dynamics and dust mobilization', *Geophysical Research Letters* **35**(20).

Hennemuth, B. and Lammert, A. (2006), 'Determination of the atmospheric boundary layer height from radiosonde and lidar backscatter', *Boundary-Layer Meteorology* **120**, 181–200.

Hersbach, H., Bell, B., Berrisford, P., Hirahara, S., Horányi, A., Muñoz-Sabater, J., Nicolas, J., Peubey, C., Radu, R., Schepers, D., Simmons, A., Soci, C., Abdalla, S., Abellan, X., Balsamo, G., Bechtold, P., Biavati, G., Bidlot, J., Bonavita, M., De Chiara, G., Dahlgren, P., Dee, D., Diamantakis, M., Dragani, R., Flemming, J., Forbes, R., Fuentes, M., Geer, A., Haimberger, L., Healy, S., Hogan, R. J., Hólm, E., Janisková, M., Keeley, S., Laloyaux, P., Lopez, P., Lupu, C., Radnoti, G., de Rosnay, P., Rozum, I., Vamborg, F., Villaume, S. and Thépaut, J.-N. (2020), 'The era5 global reanalysis', *Quarterly Journal of the Royal Meteorological Society* **146**(730), 1999–2049.
URL: *https://rmets.onlinelibrary.wiley.com/doi/abs/10.1002/qj.3803*

Hoerling, M., Eischeid, J., Perlwitz, J., Quan, X., Zhang, T. and Pegion, P. (2012), 'On the increased frequency of mediterranean drought', *Journal of climate* **25**(6), 2146–2161.

Holzworth, G. C. (1964), 'Estimates of mean maximum mixing depths in the contiguous united states', *Monthly Weather Review* **92**(5), 235–242.

Hong, S.-Y. (2010), 'A new stable boundary-layer mixing scheme and its impact on the simulated east asian summer monsoon', *Quarterly Journal of the Royal Meteorological Society* **136**(651), 1481–1496.

Huang, J., Fu, Q., Su, J., Tang, Q., Minnis, P., Hu, Y., Yi, Y. and Zhao, Q. (2009), 'Taklimakan dust aerosol radiative heating derived from calipso observations using the fu-liou radiation model with ceres constraints', *Atmospheric Chemistry and Physics* **9**(12), 4011–4021.

Hudson, J. G. (1993), 'Cloud condensation nuclei', *Journal of Applied Meteorology and Climatology* **32**(4), 596–607.

Hunt, W. H., Winker, D. M., Vaughan, M. A., Powell, K. A., Lucker, P. L. and Weimer, C. (2009), 'Calipso lidar description and performance assessment', *Journal of Atmospheric and Oceanic Technology* **26**(7), 1214–1228.

Illingworth, A. J., Cimini, D., Haefele, A., Haeffelin, M., Hervo, M., Kotthaus, S., Löhnert, U., Martinet, P., Mattis, I., O'connor, E. et al. (2019), 'How can existing ground-based profiling instruments improve european weather forecasts?', *Bulletin of the American Meteorological Society* **100**(4), 605–619.

Jacobeit, J. (1987), 'Variations of trough positions and precipitation patterns in the mediterranean area', *Journal of Climatology* **7**(5), 453–476.
URL: *https://rmets.onlinelibrary.wiley.com/doi/abs/10.1002/joc.3370070503*

Jiang, Q. and Wang, Q. (2021), 'Characteristics and scaling of the stable marine internal boundary layer', *Journal of Geophysical Research: Atmospheres* **126**(21), e2021JD035510.

Joshi, M. M., Gregory, J. M., Webb, M. J., Sexton, D. M. and Johns, T. C. (2008), 'Mechanisms for the land/sea warming contrast exhibited by simulations of climate change', *Climate dynamics* **30**, 455–465.

Kalivitis, N., Kerminen, V.-M., Kouvarakis, G., Stavroulas, I., Bougiatioti, A., Nenes, A., Manninen, H., Petäjä, T., Kulmala, M. and Mihalopoulos, N. (2015), 'Atmospheric new particle formation as a source of ccn in the eastern mediterranean marine boundary layer', *Atmospheric Chemistry and Physics* **15**(16), 9203–9215.

Kalivitis, N., Stavroulas, I., Bougiatioti, A., Kouvarakis, G., Gagné, S., Manninen, H., Kulmala, M. and Mihalopoulos, N. (2012), 'Night-time enhanced atmospheric ion concentrations in the marine boundary layer', *Atmospheric Chemistry and Physics* **12**(8), 3627–3638.

Kallos, G., Astitha, M., Katsafados, P. and Spyrou, C. (2007), 'Long-range transport of anthropogenically and naturally produced particulate matter in the mediterranean and north atlantic: Current state of knowledge', *Journal of Applied Meteorology and Climatology* **46**(8), 1230–1251.

Kang, S.-L., Davis, K. J. and LeMone, M. (2007), 'Observations of the abl structures over a heterogeneous land surface during ihop_2002', *Journal of Hydrometeorology* **8**(2), 221–244.

Kanitz, T., Engelmann, R., Heinold, B., Baars, H., Skupin, A. and Ansmann, A. (2014), 'Tracking the saharan air layer with shipborne lidar across the tropical atlantic', *Geophysical Research Letters* **41**(3), 1044–1050.

Kante, I. K., Badiane, D., Sall, S. M., Deme, A. and Diedhiou, A. (2012), 'Comparative study of the west african continental, coastal, and marine atmospheric profiles during the summer of 2006', *International Journal of Geophysics* **2012**(1), 603949.

Katoshevski, D., Nenes, A. and Seinfeld, J. H. (1999), 'A study of processes that govern the maintenance of aerosols in the marine boundary layer', *Journal of Aerosol Science* **30**(4), 503–532.

Katrib, Y., Martin, S., Rudich, Y., Davidovits, P., Jayne, J. and Worsnop, D. (2005), 'Density changes of aerosol particles as a result of chemical reaction', *Atmospheric Chemistry and Physics* **5**(1), 275–291.

Khanna, S. and Brasseur, J. G. (1997), 'Analysis of monin–obukhov similarity from large-eddy simulation', *Journal of Fluid Mechanics* **345**, 251–286.

Kim, M.-H., Yeo, H., Park, S., Park, D.-H., Omar, A., Nishizawa, T., Shimizu, A. and Kim, S.-W. (2021), 'Assessing caliop-derived planetary boundary layer height using ground-based lidar', *Remote Sensing* **13**(8), 1496.

Klose, M., Shao, Y., Karremann, M. K. and Fink, A. H. (2010), 'Sahel dust zone and synoptic background', *Geophysical Research Letters* **37**(9).

Knippertz, P. and Stuut, J.-B. W. (2014), 'Mineral dust', *Mineral dust—A key player in the Earth system* pp. 121–147.

Knippertz, P. and Todd, M. C. (2012), 'Mineral dust aerosols over the sahara: Meteorological controls on emission and transport and implications for modeling', *Reviews of Geophysics* **50**(1).

Kocha, C., Tulet, P., Lafore, J.-P. and Flamant, C. (2013), ‘The importance of the diurnal cycle of aerosol optical depth in west africa’, *Geophysical Research Letters* **40**(4), 785–790.

Kokkalis, P., Alexiou, D., Papayannis, A., Rocadenbosch, F., Soupiona, O., Raptis, P.-I., Mylonaki, M., Tzanis, C. G. and Christodoulakis, J. (2020), ‘Application and testing of the extended-kalman-filtering technique for determining the planetary boundary-layer height over athens, greece’, *Boundary-Layer Meteorology* **176**, 125–147.

Kolb, C. E. and Worsnop, D. R. (2012), ‘Chemistry and composition of atmospheric aerosol particles’, *Annual review of physical chemistry* **63**(1), 471–491.

Kotthaus, S., Bravo-Aranda, J. A., Collaud Coen, M., Guerrero-Rascado, J. L., Costa, M. J., Cimini, D., O’Connor, E. J., Hervo, M., Alados-Arboledas, L., Jiménez-Portaz, M. et al. (2023), ‘Atmospheric boundary layer height from ground-based remote sensing: a review of capabilities and limitations’, *Atmospheric Measurement Techniques* **16**(2), 433–479.

Kristensen, T. B., Müller, T., Kandler, K., Benker, N., Hartmann, M., Prospero, J. M., Wiedensohler, A. and Stratmann, F. (2016), ‘Properties of cloud condensation nuclei (ccn) in the trade wind marine boundary layer of the western north atlantic’, *Atmospheric Chemistry and Physics* **16**(4), 2675–2688.

Kudryavtsev, V. N. and Makin, V. K. (2011), ‘Impact of ocean spray on the dynamics of the marine atmospheric boundary layer’, *Boundary-layer meteorology* **140**(3), 383–410.

Lammert, A. and Bösenberg, J. (2006), ‘Determination of the convective boundary-layer height with laser remote sensing’, *Boundary-Layer Meteorology* **119**, 159–170.

Lauvaux, T., Miles, N. L., Deng, A., Richardson, S. J., Cambaliza, M. O., Davis, K. J., Gaudet, B., Gurney, K. R., Huang, J., O’Keefe, D. et al. (2016), ‘High-resolution atmospheric inversion of urban co2 emissions during the dormant season of the indianapolis flux experiment (influx)’, *Journal of Geophysical Research: Atmospheres* **121**(10), 5213–5236.

Legrand, M., Plana-Fattori, A. and N’doumé, C. (2001), ‘Satellite detection of dust using the ir imagery of meteosat: 1. infrared difference dust index’, *Journal of Geophysical Research: Atmospheres* **106**(D16), 18251–18274.

Lenoble, J., Remer, L. and Tanre, D. (2013), *Aerosol remote sensing*, Springer Science & Business Media.

Li, H., Chang, J., Liu, Z., Zhang, L., Dai, T. and Chen, S. (2020), ‘An improved method for automatic determination of the planetary boundary layer height based on lidar data’, *Journal of Quantitative Spectroscopy and Radiative Transfer* **257**, 107382.

Li, H., Liu, B., Ma, X., Jin, S., Ma, Y., Zhao, Y. and Gong, W. (2021), ‘Evaluation of retrieval methods for planetary boundary layer height based on radiosonde data’, *Atmospheric Measurement Techniques* **14**(9), 5977–5986.

Li, H., Liu, B., Ma, X., Jin, S., Wang, W., Fan, R., Ma, Y., Wei, R. and Gong, W. (2023), 'Estimation of planetary boundary layer height from lidar by combining gradient method and machine learning algorithms', *IEEE Transactions on Geoscience and Remote Sensing* .

Lionello, P. and Galati, M. (2008), 'Links of the significant wave height distribution in the mediterranean sea with the northern hemisphere teleconnection patterns', *Advances in Geosciences* **17**, 13–18.

Liu, H., Chan, J. C. and Cheng, A. Y. (2001), 'Internal boundary layer structure under sea-breeze conditions in hong kong', *Atmospheric Environment* **35**(4), 683–692.

Liu, Z., Omar, A., Vaughan, M., Hair, J., Kittaka, C., Hu, Y., Powell, K., Trepte, C., Winker, D., Hostetler, C. et al. (2008), 'Calipso lidar observations of the optical properties of saharan dust: A case study of long-range transport', *Journal of Geophysical Research: Atmospheres* **113**(D7).

Liu, Z., Vaughan, M., Winker, D., Kittaka, C., Getzewich, B., Kuehn, R., Omar, A., Powell, K., Trepte, C. and Hostetler, C. (2009), 'The calipso lidar cloud and aerosol discrimination: Version 2 algorithm and initial assessment of performance', *Journal of Atmospheric and Oceanic Technology* **26**(7), 1198–1213.

Lock, A. (2009), 'Factors influencing cloud area at the capping inversion for shallow cumulus clouds', *Quarterly Journal of the Royal Meteorological Society: A journal of the atmospheric sciences, applied meteorology and physical oceanography* **135**(641), 941–952.

Luo, B., Minnett, P. J., Zuidema, P., Nalli, N. R. and Akella, S. (2021), 'Saharan dust effects on north atlantic sea-surface skin temperatures', *Journal of Geophysical Research: Oceans* **126**(4), e2021JC017282.

Luo, T., Wang, Z., Zhang, D. and Chen, B. (2016), 'Marine boundary layer structure as observed by a-train satellites', *Atmospheric Chemistry and Physics* **16**(9), 5891–5903.

Luo, T., Yuan, R. and Wang, Z. (2014), 'Lidar-based remote sensing of atmospheric boundary layer height over land and ocean', *Atmospheric Measurement Techniques* **7**(1), 173–182.

Mahrt, L. (1999), 'Stratified atmospheric boundary layers', *Boundary-Layer Meteorology* **90**, 375–396.

Manninen, A. J., O'Connor, E. J., Vakkari, V. and Petäjä, T. (2016), 'A generalised background correction algorithm for a halo doppler lidar and its application to data from finland', *Atmospheric Measurement Techniques* **9**(2), 817–827.

Manninen, A., Marke, T., Tuononen, M. and O'Connor, E. (2018), 'Atmospheric boundary layer classification with doppler lidar', *Journal of Geophysical Research: Atmospheres* **123**(15), 8172–8189.

Marinou, E., Amiridis, V., Binietoglou, I., Tsikerdekis, A., Solomos, S., Proestakis, E., Konsta, D., Papagiannopoulos, N., Tsekeri, A., Vlastou, G. et al. (2017), 'Three-dimensional evolution of saharan dust transport towards europe based on a 9-year earlinet-optimized calipso dataset', *Atmospheric Chemistry and Physics* **17**(9), 5893–5919.

Marinou, E., Paschou, P., Tsikoudi, I., Tsekeri, A., Daskalopoulou, V., Kouklaki, D., Siomos, N., Spanakis-Misirlis, V., Voudouri, K. A., Georgiou, T. et al. (2023), 'An overview of the askos campaign in cabo verde', *Environmental Sciences Proceedings* **26**(1), 200.

Marinou, E., Voudouri, K. A., Tsikoudi, I., Drakaki, E., Tsekeri, A., Rosoldi, M., Ene, D., Baars, H., O'Connor, E., Amiridis, V. et al. (2021), 'Geometrical and microphysical properties of clouds formed in the presence of dust above the eastern mediterranean', *Remote Sensing* **13**(24), 5001.

Marsham, J. H., Parker, D. J., Grams, C. M., Johnson, B. T., Grey, W. M. and Ross, A. N. (2008), 'Observations of mesoscale and boundary-layer scale circulations affecting dust transport and uplift over the sahara', *Atmospheric Chemistry and Physics* **8**(23), 6979–6993.

McBean, G. (1986), The atmospheric boundary layer, *in* 'The Geophysics of Sea Ice', Springer, pp. 283–337.

McMurry, P. H. (2000), 'A review of atmospheric aerosol measurements', *Atmospheric Environment* **34**(12-14), 1959–1999.

McNider, R. T. and Pielke, R. A. (1981), 'Diurnal boundary-layer development over sloping terrain', *Journal of Atmospheric Sciences* **38**(10), 2198–2212.

Menut, L., Masson, O. and Bessagnet, B. (2009), 'Contribution of saharan dust on radionuclide aerosol activity levels in europe? the 21–22 february 2004 case study', *Journal of Geophysical Research: Atmospheres* **114**(D16).

Miglietta, M. M., Moscatello, A., Conte, D., Mannarini, G., Lacorata, G. and Rotunno, R. (2011), 'Numerical analysis of a mediterranean 'hurricane'over south-eastern italy: Sensitivity experiments to sea surface temperature', *Atmospheric research* **101**(1-2), 412–426.

Miller, S., Keim, B., Talbot, R. and Mao, H. (2003), 'Sea breeze: Structure, forecasting, and impacts', *Reviews of geophysics* **41**(3).

Mona, L., Amodeo, A., Pandolfi, M. and Pappalardo, G. (2006), 'Saharan dust intrusions in the mediterranean area: Three years of raman lidar measurements', *Journal of Geophysical Research: Atmospheres* **111**(D16).

Monin, A. S. and Obukhov, A. M. (1954), 'Basic laws of turbulent mixing in the surface layer of the atmosphere', *Contrib. Geophys. Inst. Acad. Sci. USSR* **151**(163), e187.

Morcrette, J.-J., Beljaars, A., Benedetti, A., Jones, L. and Boucher, O. (2008), 'Sea-salt and dust aerosols in the ecmwf ifs model', *Geophysical Research Letters* **35**(24).

Morille, Y., Haeffelin, M., Drobinski, P. and Pelon, J. (2007), 'Strat: An automated algorithm to retrieve the vertical structure of the atmosphere from single-channel lidar data', *Journal of Atmospheric and Oceanic Technology* **24**(5), 761–775.

Muhs, D. R., Prospero, J. M., Baddock, M. C. and Gill, T. E. (2014), *Identifying Sources of Aeolian Mineral Dust: Present and Past*, Springer Netherlands, Dordrecht, pp. 51–74.

Nakoudi, K., Giannakaki, E., Dandou, A., Tombrou, M. and Komppula, M. (2019), 'Planetary boundary layer height by means of lidar and numerical simulations over new delhi, india', *Atmospheric Measurement Techniques* **12**(5), 2595–2610.

Newsom, R. and Krishnamurthy, R. (2022), Doppler lidar (dl) instrument handbook, Technical report, DOE Office of Science Atmospheric Radiation Measurement (ARM) User Facility.

Nieuwstadt, F. T. (1984), 'The turbulent structure of the stable, nocturnal boundary layer', *Journal of the atmospheric sciences* **41**(14), 2202–2216.

Omar, A. H., Winker, D. M., Vaughan, M. A., Hu, Y., Trepte, C. R., Ferrare, R. A., Lee, K.-P., Hostetler, C. A., Kittaka, C., Rogers, R. R. et al. (2009), 'The calipso automated aerosol classification and lidar ratio selection algorithm', *Journal of Atmospheric and Oceanic Technology* **26**(10), 1994–2014.

O'Connor, E. J., Illingworth, A. J., Brooks, I. M., Westbrook, C. D., Hogan, R. J., Davies, F. and Brooks, B. J. (2010), 'A method for estimating the turbulent kinetic energy dissipation rate from a vertically pointing doppler lidar, and independent evaluation from balloon-borne in situ measurements', *Journal of atmospheric and oceanic technology* **27**(10), 1652–1664.

Pal, S. and Lee, T. R. (2019), 'Contrasting air mass advection explains significant differences in boundary layer depth seasonal cycles under onshore versus offshore flows', *Geophysical Research Letters* **46**(5), 2846–2853.

Palm, S. P., Hagan, D., Schwemmer, G. and Melfi, S. (1998), 'Inference of marine atmospheric boundary layer moisture and temperature structure using airborne lidar and infrared radiometer data', *Journal of Applied Meteorology and Climatology* **37**(3), 308–324.

Palm, S. P., Schwemmer, G. K., Vandemark, D., Evans, K. D. and Miller, D. O. (1999), Estimation of surface latent heat flux over the ocean and its relationship to marine atmospheric boundary layer (mabl) structure, *in* 'Application of Lidar to Current Atmospheric Topics III', Vol. 3757, SPIE, pp. 178–189.

Pappalardo, G., Amodeo, A., Apituley, A., Comeron, A., Freudenthaler, V., Linné, H., Ansmann, A., Bösenberg, J., D'Amico, G., Mattis, I. et al. (2014), 'Earlinet: towards an advanced sustainable european aerosol lidar network', *Atmospheric Measurement Techniques* **7**(8), 2389–2409.

Pastor, F., Estrela, M. J., Peñarrocha, D. and Millán, M. M. (2001), 'Torrential rains on the spanish mediterranean coast: Modeling the effects of the sea surface temperature', *Journal of Applied Meteorology and Climatology* **40**(7), 1180–1195.

Pearson, G., Davies, F. and Collier, C. (2009), 'An analysis of the performance of the ufam pulsed doppler lidar for observing the boundary layer', *Journal of Atmospheric and Oceanic Technology* **26**(2), 240–250.

Peña, A., Gryning, S.-E. and Hasager, C. B. (2008), 'Measurements and modelling of the wind speed profile in the marine atmospheric boundary layer', *Boundary-layer meteorology* **129**, 479–495.

Peña, M., Biscarri, F., Guerrero, J. I., Monedero, I. and León, C. (2016), 'Rule-based system to detect energy efficiency anomalies in smart buildings, a data mining approach', *Expert Systems with Applications* **56**, 242–255.

Pérez, C., Nickovic, S., Baldasano, J., Sicard, M., Rocadenbosch, F. and Cachorro, V. (2006), 'A long saharan dust event over the western mediterranean: Lidar, sun photometer observations, and regional dust modeling', *Journal of Geophysical Research: Atmospheres* **111**(D15).

Pezzi, L. P., Souza, R. B. d., Dourado, M. S., Garcia, C. A. E., Mata, M. and Silva-Dias, M. A. F. d. (2005), 'Ocean-atmosphere in situ observations at the brazil-malvinas confluence region', *Geophysical Research Letters* **32**(22).

Pisso, I., Sollum, E., Grythe, H., Kristiansen, N. I., Cassiani, M., Eckhardt, S., Arnold, D., Morton, D., Thompson, R. L., Groot Zwaaftink, C. D. et al. (2019), 'Flexpart 10.4', *Zenodo* .

Portalakis, P., Tombrou, M., Kalogiros, J., Dandou, A. and Wang, Q. (2021), 'Investigation of air-sea turbulent momentum flux over the aegean sea with a wind-wave coupling model', *Atmosphere* **12**(9), 1208.

Proestakis, E., Gkikas, A., Georgiou, T., Kampouri, A., Drakaki, E., Ryder, C. L., Marenco, F., Marinou, E. and Amiridis, V. (2024), 'A near-global multiyear climate data record of the fine-mode and coarse-mode components of atmospheric pure dust', *Atmospheric Measurement Techniques* **17**(12), 3625–3667.

Prospero, J. M. and Carlson, T. N. (1972), 'Vertical and areal distribution of saharan dust over the western equatorial north atlantic ocean', *Journal of Geophysical Research* **77**(27), 5255–5265.

Prospero, J. M., Ginoux, P., Torres, O., Nicholson, S. E. and Gill, T. E. (2002), 'Environmental characterization of global sources of atmospheric soil dust identified with the nimbus 7 total ozone mapping spectrometer (toms) absorbing aerosol product', *Reviews of geophysics* **40**(1), 2–1.

Prospero, J. M. and Mayol-Bracero, O. L. (2013), 'Understanding the transport and impact of african dust on the caribbean basin', *Bulletin of the American Meteorological Society* **94**(9), 1329–1337.

Rampanelli, G. and Zardi, D. (2004), 'A method to determine the capping inversion of the convective boundary layer', *Journal of Applied Meteorology and Climatology* **43**(6), 925–933.

Rao, D. B. and Prasad, D. H. (2007), 'Sensitivity of tropical cyclone intensification to boundary layer and convective processes', *Natural Hazards* **41**, 429–445.

Reddy, T. R., Mehta, S. K., Ananthavel, A., Ali, S., Annamalai, V. and Rao, D. N. (2021), 'Seasonal characteristics of sea breeze and thermal internal boundary layer over indian east coast region', *Meteorology and Atmospheric Physics* **133**, 217–232.

Rémy, S., Kipling, Z., Flemming, J., Boucher, O., Nabat, P., Michou, M., Bozzo, A., Ades, M., Huijnen, V., Benedetti, A. et al. (2019), 'Description and evaluation of the tropospheric aerosol scheme in the european centre for medium-range weather forecasts (ecmwf) integrated forecasting system (ifs-aer, cycle 45r1)', *Geoscientific Model Development* **12**(11), 4627–4659.

Rémy, S., Kipling, Z., Huijnen, V., Flemming, J., Nabat, P., Michou, M., Ades, M., Engelen, R. and Peuch, V.-H. (2021), 'Description and evaluation of the tropospheric aerosol scheme in the integrated forecasting system (ifs-aer, cycle 47r1) of ecmwf', *Geoscientific Model Development Discussions* **2021**, 1–44.

Rémy, S., Metzger, S., Huijnen, V., Williams, J. E. and Flemming, J. (2024), 'An improved representation of aerosol in the ecmwf ifs-compo 49r1 through the integration of eqsam4climv12–a first attempt at simulating aerosol acidity', *Geoscientific Model Development* **17**(21), 7539–7567.

Ren, Y., Zhang, J. A., Guimond, S. R. and Wang, X. (2019), 'Hurricane boundary layer height relative to storm motion from gps dropsonde composites', *Atmosphere* **10**(6), 339.

Richardson, L. F. (1921), 'I. some measurements of atmospheric turbulence', *Philosophical Transactions of the Royal Society of London. Series A, Containing Papers of a Mathematical or Physical Character* **221**(582-593), 1–28.

Rolph, G., Stein, A. and Stunder, B. (2017), 'Real-time environmental applications and display system: Ready', *Environmental Modelling & Software* **95**, 210–228.

Russell, L. M., Pandis, S. N. and Seinfeld, J. H. (1994), 'Aerosol production and growth in the marine boundary layer', *Journal of Geophysical Research: Atmospheres* **99**(D10), 20989–21003.

Sandu, I., Stevens, B. and Pincus, R. (2010), 'On the transitions in marine boundary layer cloudiness', *Atmospheric Chemistry and Physics* **10**(5), 2377–2391.

Schafer, R., May, P. T., Keenan, T. D., McGuffie, K., Ecklund, W. L., Johnston, P. E. and Gage, K. S. (2001), 'Boundary layer development over a tropical island during the maritime continent thunderstorm experiment', *Journal of the atmospheric sciences* **58**(15), 2163–2179.

Schepanski, K. (2018), 'Transport of mineral dust and its impact on climate', *Geosciences* **8**(5), 151.

Schepanski, K., Tegen, I., Laurent, B., Heinold, B. and Macke, A. (2007), 'A new saharan dust source activation frequency map derived from msg-seviri ir-channels', *Geophysical Research Letters* **34**(18), L18803.

Schnitker, D. (1982), 'Climatic variability and deep ocean circulation: evidence from the north atlantic', *Palaeogeography, Palaeoclimatology, Palaeoecology* **40**(1-3), 213–234.

Schween, J., Hirsikko, A., Löhnert, U. and Crewell, S. (2014), 'Mixing-layer height retrieval with ceilometer and doppler lidar: from case studies to long-term assessment', *Atmospheric Measurement Techniques* **7**(11), 3685–3704.

Schwiesow, R. (1986), 'A comparative overview of active remote-sensing techniques', *Probing the Atmospheric Boundary Layer* pp. 129–138.

Seibert, P., Kromp-Kolb, H., Kasper, A., Kalina, M., Puxbaum, H., Jost, D. T., Schwikowski, M. and Baltensperger, U. (1998), 'Transport of polluted boundary layer air from the po valley to high-alpine sites', *Atmospheric Environment* **32**(23), 3953–3965.

Seidel, D. J., Sun, B., Pettey, M. and Reale, A. (2011), 'Global radiosonde balloon drift statistics', *Journal of Geophysical Research: Atmospheres* **116**(D7).

Seidel, D. J., Zhang, Y., Beljaars, A., Golaz, J.-C., Jacobson, A. R. and Medeiros, B. (2012), 'Climatology of the planetary boundary layer over the continental united states and europe', *Journal of Geophysical Research: Atmospheres* **117**(D17).

Seinfeld, J. H. and Pandis, S. N. (2016), *Atmospheric chemistry and physics: from air pollution to climate change*, John Wiley & Sons.

Senghor, H., Machu, É., Hourdin, F. and Gaye, A. T. (2017), 'Seasonal cycle of desert aerosols in western africa: analysis of the coastal transition with passive and active sensors', *Atmospheric Chemistry and Physics* **17**(13), 8395–8410.

Shen, C., Zhao, C., Ma, N., Tao, J., Zhao, G., Yu, Y. and Kuang, Y. (2018), 'Method to estimate water vapor supersaturation in the ambient activation process using aerosol and droplet measurement data', *Journal of Geophysical Research: Atmospheres* **123**(18), 10–606.

Shin, H. H. and Hong, S.-Y. (2011), 'Intercomparison of planetary boundary-layer parametrizations in the wrf model for a single day from cases-99', *Boundary-Layer Meteorology* **139**, 261–281.

Skamarock, W. C., Klemp, J. B., Dudhia, J., Gill, D. O., Barker, D. M., Duda, M. G., Huang, X.-Y., Wang, W., Powers, J. G. et al. (2008), 'A description of the advanced research wrf version 3', *NCAR technical note* **475**(125), 10–5065.

Solomos, S., Ansmann, A., Mamouri, R.-E., Binietoglou, I., Patlakas, P., Marinou, E. and Amiridis, V. (2017), 'Remote sensing and modelling analysis of the extreme dust storm hitting the middle east and eastern mediterranean in september 2015', *Atmospheric Chemistry and Physics* **17**(6), 4063–4079.

Stanković, R. S. and Falkowski, B. J. (2003), 'The haar wavelet transform: its status and achievements', *Computers & Electrical Engineering* **29**(1), 25–44.

Stirnberg, R., Cermak, J., Kotthaus, S., Haeffelin, M., Andersen, H., Fuchs, J., Kim, M., Petit, J.-E. and Favez, O. (2021), 'Meteorology-driven variability of air pollution (pm 1) revealed with explainable machine learning', *Atmospheric Chemistry and Physics* **21**(5), 3919–3948.

Stohl, A., Forster, C., Frank, A., Seibert, P. and Wotawa, G. (2005), 'The lagrangian particle dispersion model flexpart version 6.2', *Atmospheric Chemistry and Physics* **5**(9), 2461–2474.

Stull, R. B. (1988), Mean boundary layer characteristics, *in* 'An introduction to boundary layer meteorology', Springer, pp. 1–27.

Stull, R. B. (2012), *An introduction to boundary layer meteorology*, Vol. 13, Springer Science & Business Media.

Subbey, S., Michalsen, K. and Nilsen, G. K. (2008), 'A tool for analyzing information from data storage tags: the continuous wavelet transform (cwt)', *Reviews in Fish Biology and Fisheries* **18**, 301–312.

Suck, S. and Brock, J. (1979), 'Evolution of atmospheric aerosol particle size distributions via brownian coagulation numerical simulation', *Journal of Aerosol Science* **10**(6), 581–590.

Sujatha, P., Mahalakshmi, D., Ramiz, A., Rao, P. and Naidu, C. (2016), 'Ventilation coefficient and boundary layer height impact on urban air quality', *Cogent Environmental Science* **2**(1), 1125284.

Sun, Y. and Zhao, C. (2020), 'Influence of saharan dust on the large-scale meteorological environment for development of tropical cyclone over north atlantic ocean basin', *Journal of Geophysical Research: Atmospheres* **125**(23), e2020JD033454.

Tackett, J. L., Winker, D. M., Getzewich, B. J., Vaughan, M. A., Young, S. A. and Kar, J. (2018), 'Calipso lidar level 3 aerosol profile product: Version 3 algorithm design', *Atmospheric Measurement Techniques* **11**(7), 4129–4152.

Thieuleux, F., Moulin, C., Breon, F.-M., Maignan, F., Poitou, J. and Tanré, D. (2005), Remote sensing of aerosols over the oceans using msg/seviri imagery, *in* 'Annales Geophysicae', Vol. 23, Copernicus Publications Göttingen, Germany, pp. 3561–3568.

Thorpe, A., Hoskins, B. and Innocentini, V. (1989), 'The parcel method in a baroclinic atmosphere', *Journal of Atmospheric Sciences* **46**(9), 1274–1284.

Tombrou, M., Bossioli, E., Kalogiros, J., Allan, J., Bacak, A., Biskos, G., Coe, H., Dandou, A., Kouvarakis, G., Mihalopoulos, N. et al. (2015), 'Physical and chemical processes of air masses in the aegean sea during etesians: Aegean-game airborne campaign', *Science of the Total Environment* **506**, 201–216.

Tombrou, M., Dandou, A., Helmis, C., Akylas, E., Angelopoulos, G., Flocas, H., Assimakopoulos, V. and Soulakellis, N. (2007), 'Model evaluation of the atmospheric boundary layer and mixed-layer evolution', *Boundary-layer meteorology* **124**, 61–79.

Tsaknakis, G., Papayannis, A., Kokkalis, P., Amiridis, V., Kambezidis, H., Mamouri, R., Georgoussis, G. and Avdikos, G. (2011), 'Inter-comparison of lidar and ceilometer retrievals for aerosol and planetary boundary layer profiling over athens, greece', *Atmospheric Measurement Techniques* **4**(6), 1261–1273.

Tsikoudi, I., Marinou, E., Vakkari, V., Gialitaki, A., Tsichla, M., Amiridis, V., Komppula, M., Raptis, I. P., Kampouri, A., Daskalopoulou, V. et al. (2022), 'Pbl height retrievals at a coastal site using multi-instrument profiling methods', *Remote Sensing* **14**(16), 4057.

Tsikoudi, I., Marinou, E., Voudouri, K., Koutsoupi, I., Drakaki, E., Kampouri, A., Vakkari, V., Baars, H., Giannakaki, E., Tombrou, M. et al. (2023), 'Pbl height retrievals during askos campaign', *Environmental Sciences Proceedings* **26**(1), 23.

Uno, I., Yumimoto, K., Shimizu, A., Hara, Y., Sugimoto, N., Wang, Z., Liu, Z. and Winker, D. M. (2008), '3d structure of asian dust transport revealed by calipso lidar and a 4dvar dust model', *Geophysical Research Letters* **35**(6).
URL: *https://agupubs.onlinelibrary.wiley.com/doi/abs/10.1029/2007GL032329*

Vajda, A., Tuomenvirta, H., Jokinen, P., Luomaranta, A., Makkonen, L., Tikanmäki, M., Groenemeijer, P., Saarikivi, P., Michaelides, S., Papadakis, M. et al. (2011), *Probabilities of adverse weather affecting transport in Europe: climatology and scenarios up to the 2050s*, Ilmatieteen Laitos Helsinki, Finland.

Vakkari, V., Manninen, A. J., O'Connor, E. J., Schween, J. H., Van Zyl, P. G. and Marinou, E. (2019), 'A novel post-processing algorithm for halo doppler lidars', *Atmospheric Measurement Techniques* **12**(2), 839–852.

Vakkari, V., O'connor, E., Nisantzi, A., Mamouri, R. and Hadjimitsis, D. (2015), 'Low-level mixing height detection in coastal locations with a scanning doppler lidar', *Atmospheric Measurement Techniques* **8**(4), 1875–1885.

Vaughan, M. A., Powell, K. A., Winker, D. M., Hostetler, C. A., Kuehn, R. E., Hunt, W. H., Getzewich, B. J., Young, S. A., Liu, Z. and McGill, M. J. (2009), 'Fully automated detection of cloud and aerosol layers in the calipso lidar measurements', *Journal of Atmospheric and Oceanic Technology* **26**(10), 2034–2050.

Vignati, E., De Leeuw, G. and Berkowicz, R. (2001), 'Modeling coastal aerosol transport and effects of surf-produced aerosols on processes in the marine atmospheric boundary layer', *Journal of Geophysical Research: Atmospheres* **106**(D17), 20225–20238.

Vogelezang, D. and Holtslag, A. (1996), 'Evaluation and model impacts of alternative boundary-layer height formulations', *Boundary-Layer Meteorology* **81**(3), 245–269.

von Engeln, A. and Teixeira, J. (2013), 'A planetary boundary layer height climatology derived from ecmwf reanalysis data', *Journal of Climate* **26**(17), 6575–6590.

Washington, R., Todd, M., Middleton, N. J. and Goudie, A. S. (2003), 'Dust-storm source areas determined by the total ozone monitoring spectrometer and surface observations', *Annals of the Association of American Geographers* **93**(2), 297–313.

Weitkamp, C. et al. (2005), 'Range-resolved optical remote sensing of the atmosphere', *Springer-Verlag New York* **102**, 241–303.

Whitcher, B., Guttorp, P. and Percival, D. B. (2000), 'Wavelet analysis of covariance with application to atmospheric time series', *Journal of Geophysical Research: Atmospheres* **105**(D11), 14941–14962.

Whiteman, C., Zhong, S., Bian, X., Fast, J. and Doran, J. (2000), 'Boundary layer evolution and regional-scale diurnal circulations over the and mexican plateau', *Journal of Geophysical Research: Atmospheres* **105**(D8), 10081–10102.

Whiteman, D., Melfi, S. and Ferrare, R. (1992), 'Raman lidar system for the measurement of water vapor and aerosols in the earth's atmosphere', *Applied optics* **31**(16), 3068–3082.

Wiegner, M., Emeis, S., Freudenthaler, V., Heese, B., Junkermann, W., Münkel, C., Schäfer, K., Seefeldner, M. and Vogt, S. (2006), 'Mixing layer height over munich, germany: Variability and comparisons of different methodologies', *Journal of Geophysical Research: Atmospheres* **111**(D13).

Winker, D. M., Hostetler, C. A. and Hunt, W. H. (2003), Cloud-aerosol lidar with orthogonal polarization (caliope), *in* 'IGARSS 2003. 2003 IEEE International Geoscience and Remote Sensing Symposium. Proceedings (IEEE Cat. No. 03CH37477)', Vol. 3, IEEE, pp. 1514–1516.

Winker, D. M., Vaughan, M. A., Omar, A., Hu, Y., Powell, K. A., Liu, Z., Hunt, W. H. and Young, S. A. (2009), 'Overview of the calipso mission and caliop data processing algorithms', *Journal of Atmospheric and Oceanic Technology* **26**(11), 2310–2323.

Winker, D., Tackett, J., Getzewich, B., Liu, Z., Vaughan, M. and Rogers, R. (2013), 'The global 3-d distribution of tropospheric aerosols as characterized by caliop', *Atmospheric Chemistry and Physics* **13**(6), 3345–3361.

Yamada, T. (1977), 'A numerical experiment on pollutant dispersion in a horizontally-homogeneous atmospheric boundary layer', *Atmospheric Environment (1967)* **11**(11), 1015–1024.

Young, G. S., Sikora, T. D. and Winstead, N. S. (2000), 'Inferring marine atmospheric boundary layer properties from spectral characteristics of satellite-borne sar imagery', *Monthly weather review* **128**(5), 1506–1520.

Yu, L. (2019), 'Global air–sea fluxes of heat, fresh water, and momentum: Energy budget closure and unanswered questions', *Annual Review of Marine Science* **11**(1), 227–248.

Zemba, J. and Friehe, C. A. (1987), 'The marine atmospheric boundary layer jet in the coastal ocean dynamics experiment', *Journal of Geophysical Research: Oceans* **92**(C2), 1489–1496.

Zeng, S., Vaughan, M., Liu, Z., Trepte, C., Kar, J., Omar, A., Winker, D., Lucker, P., Hu, Y., Getzewich, B. et al. (2019), 'Application of high-dimensional fuzzy k-means cluster analysis to caliop/calipso version 4.1 cloud–aerosol discrimination', *Atmospheric Measurement Techniques* **12**(4), 2261–2285.

Zhong, T., Wang, N., Shen, X., Xiao, D., Xiang, Z. and Liu, D. (2020), 'Determination of planetary boundary layer height with lidar signals using maximum limited height initialization and range restriction (mlhi-rr)', *Remote Sensing* **12**(14), 2272.

Zhou, W., Leung, L. R., Lu, J., Yang, D. and Song, F. (2020), 'Contrasting recent and future itcz changes from distinct tropical warming patterns', *Geophysical Research Letters* **47**(22), e2020GL089846.